System Design and Scaling Trends in Airborne Wind Energy

Joshi, R.

DOI
10.4233/uuid:4332d7c1-16da-40cf-8bbe-201bab967581

Publication date
2025

Document Version
Final published version

Citation (APA)
Joshi, R. (2025). *System Design and Scaling Trends in Airborne Wind Energy*. [Dissertation (TU Delft), Delft University of Technology]. https://doi.org/10.4233/uuid:4332d7c1-16da-40cf-8bbe-201bab967581

System Design and Scaling Trends In Airborne Wind Energy

Rishikesh Joshi

System Design and Scaling Trends in Airborne Wind Energy

System Design and Scaling Trends in Airborne Wind Energy

Dissertation

for the purpose of obtaining the degree of doctor
at Delft University of Technology
by the authority of the Rector Magnificus, prof. dr. ir. T.H.J.J. van der Hagen,
chair of the Board for Doctorates
to be defended publicly on
Monday 16 June 2025 at 10:00 o'clock

by

Rishikesh JOSHI

Master of Science in Sustainable Energy Technology
Delft University of Technology, The Netherlands
born in Pune, India

This dissertation has been approved by the promotors.

Composition of the doctoral committee:

Rector Magnificus,	chairperson
Prof.dr. D. A. von Terzi,	Delft University of Technology, promotor
Dr.-Ing. R. Schmehl,	Delft University of Technology, promotor

Independent members:

Prof.dr. S. J. Watson,	Delft University of Technology
Prof.dr. C. L. Bottasso,	Technical University of Munich, Germany
Prof.dr. A. Croce,	Politecnico di Milano, Italy
Dr. M. K. McWilliam,	Technical University of Denmark, Denmark
Dr. C. Vergara,	Kitepower B.V., The Netherlands
Prof.dr.ir. A. C. Viré,	Delft University of Technology, reserve member

This research was part of the NEON research program and was funded by the Nederlandse Organisatie voor Wetenschappelijk Onderzoek (NWO) under grant no. 17628.

Keywords: airborne wind energy, performance modelling, system design, levelised cost of energy, techno-economic analysis, scaling

Printed by: Proefschriftspecialist

Cover by: Aditya Wankhade – Portfolio

(Front: An airborne wind energy kite soars through the sky, symbolising innovation and sustainability. Back: The colours within the bulb signify the ignition of new possibilities and advancing knowledge, set against the backdrop of Saraswati.)

ISBN 978-94-6518-073-1

An electronic copy of this dissertation is available at
https://repository.tudelft.nl/.

To Aai & Baba

Renewable energy is vital in addressing the climate crisis, but true impact lies in consuming less and living more consciously

CONTENTS

SUMMARY

Airborne wind energy (AWE) is an emerging technology that differs in operating principles from horizontal axis wind turbines (HAWTs). It uses tethered flying devices to harness higher-altitude wind resources. The primary motivation for AWE development lies in its potential to deliver similar energy output at lower costs and reduced carbon emissions compared to wind turbines of equivalent power ratings. AWE is in its early development stage, with commercial prototypes reaching power outputs of up to several hundred kilowatts. At this early stage of technology development, the AWE industry can significantly benefit from a systems-level understanding of the technology. To this end, the work reported here developed a multi-disciplinary design, analysis and optimisation (MDAO) tool for the conceptual system design of an AWE device and applied it to identify key design drivers, trade-offs and the scaling potential of a chosen AWE concept.

The MDAO tool is a framework that integrates models, including wind resources, power production, energy production and costs. As part of this research, new models were developed to enable the framework's functionality. This study focused on the fixed-wing ground-generation (GG) concept of AWE. Still, the proposed methodology can be applied to any AWE concept depending on the availability of individual models tailored to the particular concept. In most markets, performance is measured using a metric known as the levelised cost of energy (LCoE). This metric relates the system's total costs to the energy it can produce over its lifetime. This metric is used here as the objective for system design, evaluating trade-offs and scaling analysis.

For the performance calculation, a quasi-steady model was developed to estimate the electrical cycle average power of fixed-wing GG AWE systems. In this approach, the kite is represented as a point mass and operated in circular flight manoeuvres while reeling out the tether. The model accounts for various factors such as flight elevation, gravity, vertical wind shear, hardware limitations, and drivetrain losses. A unique characteristic of GG AWE systems is their cyclical power output, arising from alternating reel-out and reel-in phases. An intermediate storage buffer is required to deliver smooth power to the grid. Three drivetrain configurations—based on electrical, hydraulic, and mechanical storage technologies—were investigated, with the electrical drivetrain identified as the most suitable choice for early commercialisation. To estimate the LCoE, a reference economic model was developed as part of an IEA Wind Task 48 activity, which included data contributions from 10 industry and academic participants. The model provides capital and operational cost estimates for AWE components and defines economic metrics for use in system design and optimisation.

The MDAO framework was applied to optimise system design parameters, minimising LCoE for rated power capacities of 100, 500, 1000, and 2000 kW. Results indicated that the minimum LCoE was achieved at 500 kW, with diminishing returns in power output per unit wing area as the wing size increased. This finding suggests that scaling up

fixed-wing GG AWE systems to multi-megawatt capacities may not yield significant economic benefits due to the increasing impact of kite mass on both energy production and costs. Power smoothing was identified as a key challenge, as it significantly influences drivetrain sizing and associated costs, which account for approximately 50% of the total LCoE. The primary cost drivers for fixed-wing GG AWE systems were found to be kite mass, storage requirements, and tether replacement costs. Therefore, future development efforts should focus on reducing kite mass through advanced materials and manufacturing techniques, enhancing tether fatigue life, and optimising operations to minimise replacements. A noteworthy distinction from HAWTs is that for AWE systems, lifetime operational costs are equal to or greater than initial capital expenditures. This cost structure makes AWE systems more financially accessible in markets with limited availability of upfront capital.

Although the framework in this research was developed for fixed-wing GG systems, it can be adapted to other AWE concepts with tailored models, enabling broader insights into scaling and design. This adaptability positions the framework as a valuable tool for guiding the evolution of AWE technology.

SAMENVATTING

Airborne windenergie (AWE) is een innovatieve technologie die qua werking fundamenteel verschilt van conventionele windturbines met een horizontale as (HAWTs). In plaats van vaste torens en rotorbladen maakt AWE gebruik van vliegende systemen die via touwen met de grond zijn verbonden, waardoor zij de sterkere en constantere wind op grotere hoogte kunnen benutten. De voornaamste drijfveer achter de ontwikkeling van AWE is het potentieel om een vergelijkbare hoeveelheid energie op te wekken als traditionele windturbines, maar dan tegen lagere kosten en met een kleinere CO_2-voetafdruk. Momenteel bevindt AWE zich nog in een vroeg stadium van technologische ontwikkeling, met commerciële prototypes die vermogens van enkele honderden kilowatt bereiken. In deze ontwikkelingsfase kan de sector sterk profiteren van een geïntegreerde, systeembrede benadering van ontwerp en prestatieanalyse. Dit proefschrift beschrijft de ontwikkeling van een multidisciplinaire tool voor ontwerp, analyse en optimalisatie (MDAO), bedoeld voor het conceptuele ontwerp van AWE-systemen. Met deze tool zijn belangrijke ontwerpkeuzes, afwegingen en schaalvoordelen van een specifiek AWE-concept in kaart gebracht.

De MDAO-tool vormt een raamwerk waarin diverse modellen worden geïntegreerd, waaronder modellen voor windbronnen, energieopbrengst, vermogensproductie en kosten. Voor dit onderzoek zijn nieuwe modellen ontwikkeld om de werking van het raamwerk mogelijk te maken. De focus ligt op het AWE-concept met een vaste vleugel en grondgebonden energieopwekking (ground-generation, GG). De voorgestelde methodiek is echter ook toepasbaar op andere AWE-concepten, mits er geschikte modellen beschikbaar zijn voor het betreffende concept. In de meeste energiemarkten wordt de prestatie van energiesystemen beoordeeld aan de hand van de genivelleerde kosten van energie (Levelized Cost of Energy, LCoE), een maatstaf die de totale kosten van het systeem relateert aan de hoeveelheid energie die het gedurende de levensduur kan opwekken. In dit onderzoek wordt de LCoE gehanteerd als doelmaat voor het systeemontwerp, afwegingsanalyses en schaalanalyses.

Voor het berekenen van de prestaties is een quasi-statisch model ontwikkeld om het gemiddelde elektrische vermogen per cyclus van vaste-vleugel GG-AWE-systemen te schatten. In dit model wordt de vlieger benaderd als een puntmassa die cirkelvormige vliegbewegingen uitvoert tijdens het uitrollen van het touw. Het model houdt rekening met verschillende factoren, zoals vlieghoogte, zwaartekracht, de verticale windgradiënt, hardwarebeperkingen en het rendement van de aandrijflijn. Een onderscheidend kenmerk van GG-AWE-systemen is de cyclische vermogensproductie, waarbij het touw afwisselend wordt uit- en ingehaald. Om een stabiele vermogenslevering aan het elektriciteitsnet te waarborgen, is een tussentijdse opslagbuffer noodzakelijk. Drie configuraties van de aandrijflijn – gebaseerd op elektrische, hydraulische en mechanische opslag – zijn onderzocht, waarbij de elektrische aandrijflijn als het meest geschikt werd beoordeeld voor

vroege commercialisatie. Voor het inschatten van de LCoE is een referentie-economisch model ontwikkeld binnen het kader van IEA Wind Task 48, met bijdragen van tien industriële en academische partners. Dit model biedt schattingen van kapitaal- en operationele kosten voor AWE-componenten en definieert de economische parameters voor toepassing in ontwerp en optimalisatie.

Het MDAO-raamwerk is ingezet om systeemparameters te optimaliseren met als doel de LCoE te minimaliseren voor vermogensklassen van 100, 500, 1000 en 2000 kW. Uit de resultaten blijkt dat de laagste LCoE wordt bereikt bij 500 kW, terwijl de opbrengsten per vierkante meter vleugeloppervlak afnemen bij verdere opschaling van het systeem. Dit suggereert dat het vergroten van vaste-vleugel GG-AWE-systemen tot multi-megawattvermogens mogelijk geen significante economische voordelen oplevert, met name vanwege de toenemende invloed van de massa van de vlieger op zowel de energieproductie als de kosten. Vermogensafvlakking is geïdentificeerd als een belangrijke uitdaging, aangezien dit aspect een grote impact heeft op de dimensionering en kosten van de aandrijflijn, die circa 50% van de totale LCoE bepalen. De belangrijkste kostenfactoren voor GG-AWE-systemen zijn de massa van de vlieger, de opslagvereisten en de vervangingskosten van het touw. Daarom zou toekomstige ontwikkeling zich moeten richten op het verlagen van de vliegermassa door middel van geavanceerde materialen en productieprocessen, het verbeteren van de vermoeiingslevensduur van het touw, en het optimaliseren van de bedrijfsvoering om het aantal vervangingen te minimaliseren. Een opvallend verschil met conventionele windturbines is dat bij AWE-systemen de operationele kosten gedurende de levensduur gelijk aan of zelfs hoger kunnen zijn dan de initiële investeringskosten. Dit kostenprofiel maakt AWE-systemen met name financieel aantrekkelijk in markten waar het beschikbare startkapitaal beperkt is.

Hoewel het ontwikkelde raamwerk specifiek is toegepast op vaste-vleugel GG-systemen, kan het met aangepaste modellen worden uitgebreid naar andere AWE-concepten. Dit maakt het raamwerk tot een waardevol instrument voor het verkrijgen van bredere inzichten in schaalbaarheid en ontwerpkeuzes, en het kan zo een belangrijke bijdrage leveren aan de verdere ontwikkeling van AWE-technologie.

NOMENCLATURE

Greek symbols

α	Wind shear coefficient
β	Elevation angle
χ	Course angle
η	Efficiency
γ	Cone opening angle
λ	Tangential velocity factor
ϕ	Azimuth angle
Ψ	Roll angle
ρ	Material density
σ	Material strength
τ	Tangential
θ	Polar angle
ζ	Power harvesting factor

Latin symbols

$Æ$	Aspect ratio
A	Area
a	Acceleration
C	Capital cost
C_D	Drag coefficient
C_L	Lift coefficient
D	Drag
d	Diameter

E	Energy
e	Wing planform efficiency factor
F	Force
f	Factor
h	Height
L	Lift
l	Length
m	Mass
N	Number
O	Operation and maintenance cost per year
P	Power
p	Price per unit
R	Radius
r	Discount rate
S	Wing area
t	Time
v	Velocity
X	X-axis co-ordinate
Y	Y-axis co-ordinate
Z	Z-axis co-ordinate

Subscripts

a	Aerodynamic
avg	Average
batt	Batteries
BoP	Balance of plant
BoS	Balance of systems
decomm	Decommissioning
DT	Drivetrain

e	Electrical
eff	Effective
found	Foundation
g	Gravity
gb	Gearbox
gen	Generator
i	Reel-in
insyall	Installation and commissioning
k	Kite
l	Loading
m	Mechanical
mat	Material
max	Maximum
min	Minimum
o	Reel-out
p	Pattern
pc	Power converters
r	Radial
ref	Reference
sto	Storage
str	Structure
t	Tether
w	Wind
y	Year

List of Figures

List of Tables

1

INTRODUCTION

1.1. WHY AIRBORNE WIND ENERGY?

The EU Directive [1] on the European Green Deal [2] set out in 2019 states that the EU should achieve climate neutrality in the member countries by 2050 and an intermediate reduction of net greenhouse gas emissions by at least 55% by 2030, compared to the 1990 levels. In response, the EU Commission proposed the REPowerEU plan [3] to double the share of renewables in the energy mix by 2030, compared to 2020, to reach at least 40%. Large-scale deployment of renewables will be crucial in achieving these targets. Wind energy is set to become the primary source of electricity in Europe shortly after 2025, and by 2030, it will provide almost 25% of the EU's electricity needs [4]. Europe currently has around 300 GW of installed wind energy capacity and has targets to have around 500 GW in 2030 [5] and around 1200 GW in 2050 [6]. Most countries have set similar ambitious targets for wind energy [7]. These trends indicate that wind energy will play a central role in the energy transition and the future global energy mix.

Significant progress has been made in the development and scaling of horizontal axis wind turbines (HAWTs) over the past half-century. The increase in power ratings and diameters has been associated with reductions in the cost of energy for wind projects [8]. This has led to wind being one of the cheapest energy sources. However, with the increasing sizes, these machines are now encountering challenges in further upscaling due to structural, logistical, and economic constraints [9, 10]. Airborne wind energy (AWE) is an emerging technology that uses tethered airborne devices to harness the higher altitude wind resource inaccessible to HAWTs [11] with potentially lower material usage [12, 13]. It differs in operating principles from HAWTs and has the potential to become a complementary wind energy technology to accelerate the energy transition. The primary motivation behind developing AWE technology is the hypothesis that for a given location, a similar amount of energy can be produced at a lower cost and carbon footprint than a wind turbine of a similar power rating.

Multiple AWE concepts exist and can be classified in various ways. A review of all existing technologies can be found in [14, 15]. One classification criterion is the type of flight operation, which can be crosswind or tether-aligned. Another criterion is the power generation method, which can be fly-generation (FG) or ground-generation

(GG). In the FG concept, power is produced onboard using small ram-air turbines and transmitted to the ground via conducting tethers. In the GG concept, the kite pulls the tether, which unwinds a drum-generator module on the ground, generating power. Another GG concept, the rotary system, involves transmitting the torque generated by a network of wings to a ground-based generator via a network of tethers. Additionally, AWE systems can also be classified based on the type of flying device, which includes multiple concepts such as soft-wing, fixed-wing, and hybrid-wing configurations. Figure 1.1 shows the implemented concepts by different companies till now and Table 1.1 gives their respective details.

Table 1.1: Tested commercial airborne wind energy prototypes.

Developer	**Prototype**	**Concept**	**Kite type**	**Rated Power (kW)**	**Source**
Mozaero[a]	AP3	GG	Fixed-wing	150	[18]
Kitemill	KM1	GG	Fixed-wing	20	[19, 20]
TwingTec	Twing (T29)	GG	Fixed-wing	10	[21]
Windlift	C1	FG	Fixed-wing	2	[22–24]
EnerKíte	EK30/Enerwing	GG	Hybrid-wing	30	[25]
Toyota	Mothership v11	GG	Soft-wing	1	[26–28]
Kitekraft	SN9	FG	Box-wing	12	[29]
Makani[b]	M600	FG	Fixed-wing	600	[30]
CPECC	Airpower	GG	Parachute	2400[c]	[31, 32]
Skysails Power	SKN PN-14	GG	Soft-wing	120	[33]
Kitepower	Falcon	GG	Soft-wing	100	[34]
Kitenergy	KE60 Mark II	GG	Soft-wing	60	[35]
Windswept	Kite Turbine	GG	Rotary	1	[36]
Wind Fisher	MAG1	GG	Magnus rotor	-	[37]
someAWE	MAR3	GG	Rotary	0.5	[38, 39]

[a] Formerly known as Ampyx Power

[b] Operations discontinued

[c] Maximum reel-out power

This thesis focuses on the fixed-wing GG concept as illustrated in fig. 1.2. A fixed-wing kite analogous to a glider aircraft is connected by a tether to a drum-generator module on the ground. The kite flies in repetitive crosswind patterns, pulling the tether with high force from the drum and driving the generator, as shown in fig. 1.2(a). During this reel-out phase, electricity is generated. Once the tether has reached a certain length, the kite is retracted towards the generator with minimum aerodynamic drag and substantially lower force as shown in fig. 1.2(b). A small fraction of the generated electricity is consumed during this reel-in phase. An intermediate buffer storage is typically used for this purpose. The reel-out and reel-in phases are repeated cyclically to generate a net power output.

Figure 1.1: Implemented and tested commercial prototypes, ordered from left to right and top to bottom according to Table 1.1. The thumbnails are adapted from [16, 17].

1

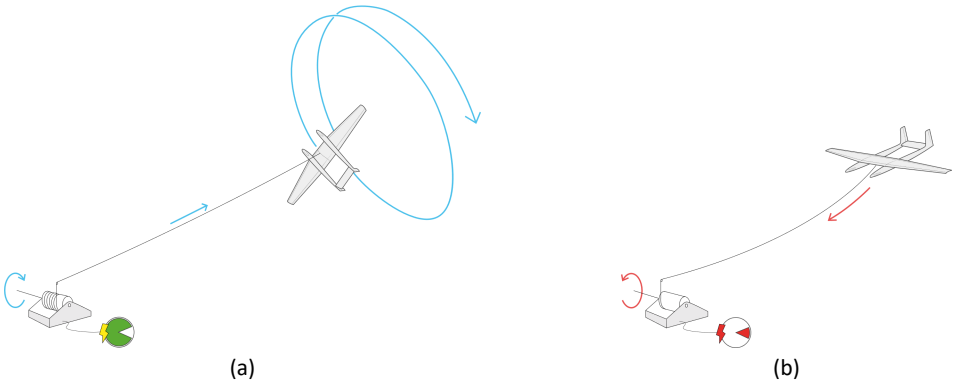

Figure 1.2: Operation schematic of the fixed-wing ground-generation airborne wind energy concept [40]: (a) Reel-out phase, (b) Reel-in phase (image courtesy of Mozaero [41]).

Figure 1.3 shows the analogy between the components of a HAWT and a GG AWE system. The rotor nacelle assembly of wind turbines is structurally held at the designed hub height with the help of a tower. In contrast, the kite maintains the required height by spending part of its aerodynamic force to compensate for the gravitational force. A hub is responsible for the torque transfer from the wind turbine blades to the generator. While, the GG AWE systems extract power from the pulling force generated by the kite, which is then transferred with the help of a tether to a drum on the ground. The drum is then responsible for converting this linear pulling force into torque, which drives the generator. These differences in components and operational principles suggest that the scaling trends of AWE systems might be different from those of HAWTS.

1.2. RESEARCH GAP AND QUESTIONS

Compared to wind turbines, AWE is still in its early development phase, with the first commercial prototypes in the range of up to several hundred kilowatts [43]. At this early stage of technology development, the AWE industry can profit significantly from a systems-level understanding of the technology. This can guide the development by identifying the right sizing and the key design drivers. Design drivers are the aspects or parameters that greatly affect the performance of systems. Understanding these can lead to a better understanding of the potential of the technology and its value proposition.

Fast and scalable models that capture all relevant physics are essential for system design studies, but the field lacks highly matured and sophisticated models [44, 45]. Studies presented in [40, 46, 47] performed system design and scaling analysis focusing on the performance of systems in terms of power or energy production, but in most markets, performance is measured using a metric known as the levelised

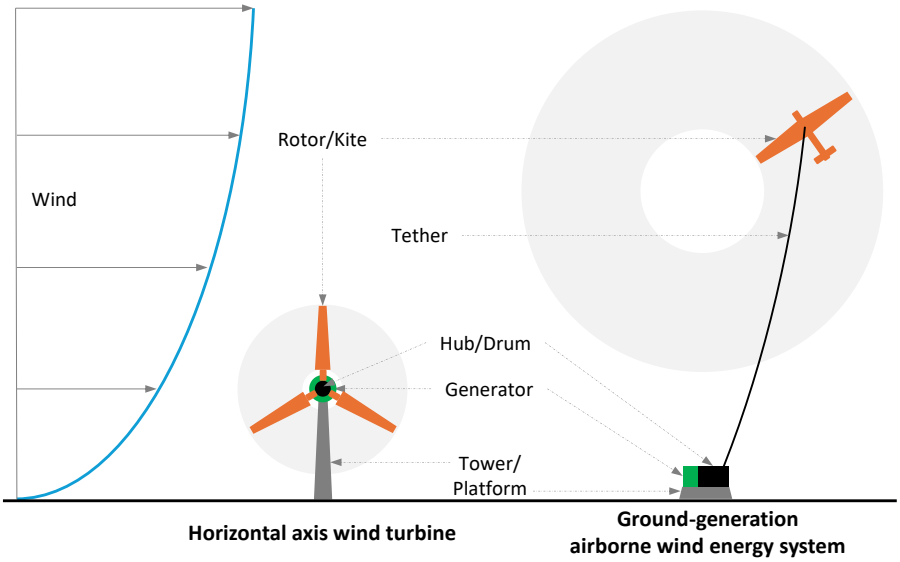

Figure 1.3: Analogy between the components of a horizontal-axis wind turbine and a ground-generation airborne wind energy system [42].

cost of energy (LCoE). This metric relates the system's total costs to the energy it can produce over its lifetime. A cost model, along with power and energy production models, is needed to evaluate this metric. Grete [48] and Faggiani and Schmehl [49] performed LCoE-driven design studies using a quasi-steady model for soft-wing GG system developed presented in [50, 51] and building upon the cost model proposed in [52]. In these studies, the kite mass was only considered dependent on wing area, but it will also depend on the aspect ratio and the wing loading. The generator-rated power was considered a constant parameter in the optimisation but should instead be considered a design parameter since it has a significant cost share. Tether lifetime and intermediate storage costs for power smoothing were not modelled. Table 1.2 lists the LCoE values reported in articles and technical reports available in the public domain. The range of values is indicative of the uncertainty and diversity in modelling assumptions of different studies. A comprehensive system design analysis by coupling power, energy production and cost models is still missing in the literature.

The present work, therefore, aims to develop an understanding of the key design drivers, trade-offs, and scaling potential of AWE systems while considering all relevant aspects together. This leads to the formulation of the following overarching research question and subquestions.

- ***What is the system design that minimises the cost of airborne wind energy?***

RQ1. How do we model the electrical power production profile and capital and operational expenditures of a given kite–tether–ground station configuration?

Table 1.2: Overview of LCoE values reported in the public domain.

AWE concept	Power (kW)	LCoE (€/MWh)	Source
Soft-wing GG	[600, 900, 1400]*	[50, 45, 48]	[52]
Soft-wing GG	[600, 900, 1400]*	[43, 50, 60]	[48]
Soft-wing GG	[20, 200, 2000]	[19-32, 18-22, 25-43]	[53]
Agnostic	Agnostic	46-150	[54]
Soft-wing GG	[20, 200, 2000]	[51-57, 45-50, 46-51]	[55]
Soft-wing GG	100	120	[49]
Agnostic	4100	72	[56]
Agnostic	Agnostic	40-80	[57]

* maximum reel-out power

RQ2. What methodology can be employed to find an optimal system design that minimises the levelised cost of energy?

RQ3. What are the factors that drive the scaling of airborne wind energy systems?

These research questions can be answered by developing a holistic and integrated framework that can evaluate the impact of a change in a design parameter on the system's performance with respect to a chosen objective. We have developed a multi-disciplinary design, analysis and optimisation (MDAO) framework that integrates models including wind resources, power production, energy production and costs. Since there are limitations in the fidelity of simulation models for AWE, the goal was not to produce absolute values describing an optimal system design with the least possible LCoE but to identify the trends within the design space. This work is focused on the fixed-wing ground-generation concept, but the proposed methodology can be applied to any AWE concept depending on the availability of individual models tailored to the particular concept.

1.3. THESIS OUTLINE

The chapter outline of the thesis is as follows:

- **Chapter 2:** Power Curve Modelling
  This chapter describes the developed model for estimating the power curve of a fixed-wing GG AWE system.

- **Chapter 3:** Drivetrain Concepts for Power Smoothing
  This chapter presents a comparative analysis of three different drivetrain concepts for power smoothing of GG AWE systems.

- **Chapter 4:** Cost Modelling and Economic Metrics
  This chapter presents the developed cost model for estimating capital and operational costs of AWE systems and defines the economic metrics that can be used as design objectives.

- **Chapter 5:** System Design and Scaling Trends
  This chapter presents the developed system design framework, which integrates the models described in the previous chapters.

- **Chapter 6:** Conclusions
  This chapter summarises the conclusions from all the chapters and presents the key findings, limitations and implications of this dissertation.

This outline is visualised in fig. 1.4. Chapters 2 to 4 form the building blocks of the integrated framework and, hence, are standalone chapters which could be read out of order. The blue arrows indicate the complete storyline in order.

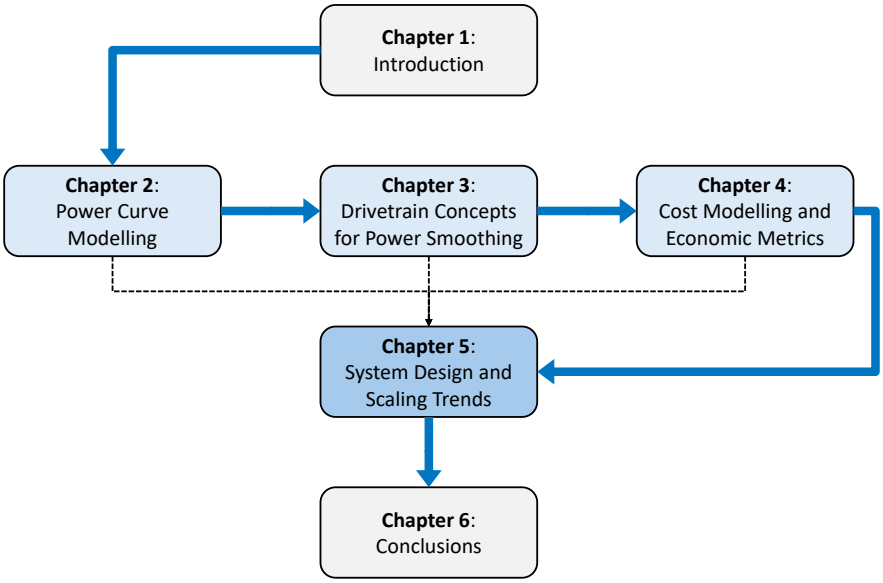

Figure 1.4: Visual thesis outline. The blue arrows show the reading order, and the dashed line shows that the models and the methods described in Chapters 2 to 4 are integrated into a framework presented in Chapter 5.

2

POWER CURVE MODELLING

This chapter addresses the first identified research question related to the power curve modelling of airborne wind energy (AWE) systems. We present a fast model for estimating the net power output of fixed-wing ground-generation AWE systems in the conceptual design phase. In this quasi-steady approach, the kite is represented as a point mass and operated in circular flight manoeuvres while reeling out the tether. This phase is subdivided into several segments. Each segment is assigned a single flight state resulting from an equilibrium of the forces acting on the kite. The model accounts for the effects of flight pattern elevation, gravity, vertical wind shear, hardware limitations, and drivetrain losses. The simulated system is defined by the kite, tether and drivetrain properties, such as the kite wing area, aspect ratio, aerodynamic properties, tether dimensions and material properties, generator rating, maximum allowable drum speed, etc.

The outline of this chapter is as follows. Section 2.2 describes the theoretical framework, which begins with simplifying assumptions and then builds up by relaxing them step by step, Section 2.3 presents the model capabilities through a numerical example, effects of gravity, scaling on performance and Section 2.4 presents the conclusions.

This chapter has been adapted from the following peer-reviewed article:

[40] R. Joshi, R. Schmehl, and M. Kruijff. "Power curve modelling and scaling of fixed-wing ground-generation airborne wind energy systems". In: Wind Energy Science 9.11 (2024), pp. 2195–2215. DOI: 10.5194/wes-9-2195-2024.

2.1. STATE-OF-ART

Compared to flexible membrane kites, fixed-wing kites are characterised by better aerodynamic performance, a higher lift-to-drag ratio, and a substantially larger mass-to-wing surface ratio. While the first ratio stays roughly the same when increasing the size of the kite, the latter ratio progressively increases. This increase affects fixed-wing kites much more than it does soft-wing kites, rendering mass a crucial parameter for designing large-scale fixed-wing AWES. The present work focuses on the gravitational effect of mass and its interplay with the resultant aerodynamic force and the tether force during quasi-steady flight operation. To understand this effect, it is important to note that the gravitational force is a constant contribution to the force equilibrium at the kite. In contrast, the aerodynamic force depends on the instantaneous flight speed and can thus vary greatly in the different operational phases of the system. The tether force, on the other hand, is a reaction force to the vectorial sum of the two external forces.

Because of the fast crosswind manoeuvres in the reel-out phase, the apparent wind speed is high, and the quasi-steady force equilibrium is dominated by the aerodynamic loading and the tether force - except for low wind speeds at cut-in where the gravitational force contributes substantially. In the reel-in phase, the gravitational effect is exploited to retract the kite with a minimum tether force and thus reel-in power. The force equilibrium is dominated by the aerodynamic and gravitational forces, while the tether force plays only a minor role. Several different strategies exist for launching and landing. For AWE systems pursuing a vertical takeoff and landing (VTOL) strategy, the aerodynamic force generated by the VTOL subsystem is used entirely to overcome gravity because the wing is either perpendicular to the wind and thus ineffective for lift (e.g. Makani or Kitekraft) or aligned with the wind but providing an insufficient lift force (e.g. Kitemill or TwingTec). For AWE systems pursuing a horizontal takeoff and landing (HTOL) strategy, the kite needs to be accelerated by an external mechanism to a certain minimum flight speed at which the aerodynamic force can overcome gravity. This can be done with a catapult and optional onboard propellers (e.g. Ampyx Power) or a swivelling mast (Enerkíte). Irrespective of how the fixed-wing kite is launched or landed, it has to maintain a certain minimum flight speed during crosswind operation to create an aerodynamic load level sufficient to compensate for gravity's effect and stay airborne. This interplay between aerodynamic, gravitational, and tether forces during the different operational phases requires careful tradeoff analysis when designing a fixed-wing AWE system.

Several physical models with a broad spectrum of fidelity and scope have been developed to understand and mathematically describe the operation of AWE systems. Higher-fidelity approaches based on dynamic models and system control, such as in [58–60] are computationally expensive and require the initialisation and tuning of many parameters. [46] investigated the scaling effects of fixed-wing ground-generation AWE systems using AWEbox [61], which is an optimal control framework. Their simulation results do not reveal consistent trends, which could indicate non-converged results. The results of such models are highly dependent on the implemented controller's performance. Hence, they are not the best option for

understanding the fundamental principles of systems, the achievable energy output, and the interdependencies between environmental, system design, and operational parameters. Lower-fidelity approaches based on steady or quasi-steady models can be used for this purpose, and techno-economic analysis, such as in [49, 52, 62].

There have been several attempts to model the power generation characteristics of AWE systems with lower fidelity, but none of the theories account for all the relevant physical effects. The first mathematical foundation for estimating power extraction using tethered kites in a crosswind motion was laid by [63]. This analytical theory assumes idealised flight states to estimate the mechanical power output of a pumping AWE system, but it does not account for losses due to elevation, retraction phase, gravity, vertical wind shear, and hardware limitations.

[64] extended this crosswind theory to spherical coordinates to compute the mean mechanical reel-out power of ground generation systems. The theory accounts for the averaged effects of elevation and gravity on the kite but does not account for the losses due to the retraction phase. [65] extended Loyd's ideal power extraction theory for fixed-wing ground generation systems to account for the retraction phase, average pattern elevation and hardware limitations such as the maximum tether force and generator power rating. But, their study did not account for the effect of gravity. [66] presented a model for soft-wing ground generation systems that accounts for losses due to elevation, the transition phase, and the retraction phase but did not account for the effect of gravity. They also accounted for various efficiencies of the ground station in computing net electrical power output. The model results were compared against measurements of a 4 kW prototype demonstrator.

[67] presented a model to compute the net power output that accounts for the traction and retraction phases, including gravity and component efficiencies. However, the paper does not provide explicit problem formulation using gravity nor highlight the relevance of different force terms. The model results were compared against measurements of a 5 kW prototype, which showed deviations within their expected range. It was also compared to a full six-degree-of-freedom (6-DoF) simulation of a 30 kW system which showed good agreement between their models. [68] presented an analytical modelling framework to compute net power output, accounting for the losses due to elevation, gravity, and the retraction phase. Following this work, [69] proposed refining the power estimation by including the effect of far wake on the induced drag. These losses were modelled as loss factors to calculate the net power output. The model results were not compared against higher fidelity simulations or measurements.

A quasi-steady model (QSM) for soft-wing ground generation systems was developed by [50, 51] and validated by [70] using measurements from a 20 kW prototype. This model accounts for the losses due to elevation, retraction phase, transition phase and gravity. We have extended this formulation to fixed-wing systems by incorporating changes in the retraction phase, angle of attack controllability impacting the operational lift coefficient, consideration of induced drag, effects of vertical wind shear, hardware limitations, and drivetrain losses. The model is then used to formulate an optimisation problem to find the operational set points for maximising the system's electrical cycle power. The study offers several insights into

the impact of gravity and system scaling across low and high wind speeds. The findings highlight how kite and tether mass scaling influences performance, revealing trade-offs between larger and smaller kite-tether configurations.

The chapter is structured as follows. Section 2.2 describes the theoretical framework, which begins with simplifying assumptions and then builds up by relaxing them step by step; Section 2.3 presents the model capabilities through a numerical example, effects of gravity, scaling on performance and Section 2.4 presents the conclusions.

2.2. MODEL DESCRIPTION

Consider a fixed-wing kite, analogous to a glider aeroplane, with wing planform area S, aspect ratio AR, lift and drag coefficients C_L and C_D, respectively, with a tether of maximum allowable force $F_\mathrm{t,max}$, flying on a circular flight trajectory, with a turning radius of R_p, cone opening angle γ_p, and turning axis elevation angle β_p, which is also referred to as the pattern elevation angle in the following sections. The pattern elevation angle is kept constant for one reel-out and reel-in phase. This is the first step of a system-level performance analysis, so unsteady effects such as turbulence or wind gusts are not considered. The kite kinematics and the forces acting on the kite are formulated in a spherical reference frame (r,θ,ϕ), defined with respect to the Cartesian wind reference frame $(\mathrm{X_w},\mathrm{Y_w},\mathrm{Z_w})$. The horizontal axis is aligned with the wind velocity $\mathbf{v}_\mathrm{w}$ and its Z-axis pointing vertically upwards, as shown in fig. 2.1. The unit vectors $\mathbf{e}_\mathrm{r},\mathbf{e}_\theta$, and $\mathbf{e}_\phi$ define a right-handed local vector base. The kite's position is represented by point **K**, and the ground station is located at the origin **O**. The radial coordinate r specifies the geometrical distance between the kite and the ground station, θ is the polar angle which is complementary to the tether elevation angle β measured from the ground (i.e. $\theta+\beta=90°$), and ϕ is the azimuth angle.

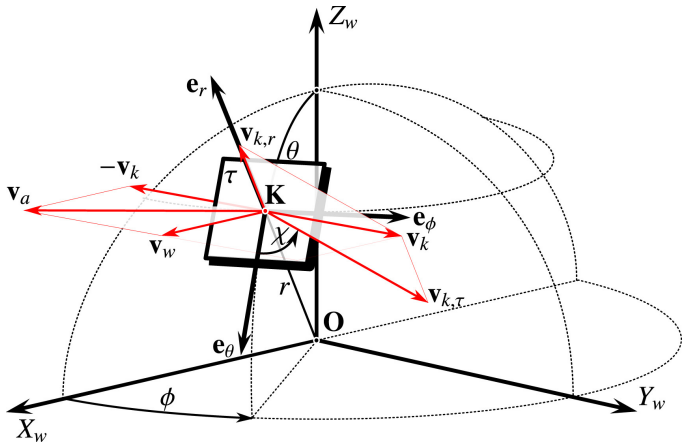

Figure 2.1: Decomposition of kite kinematics in a spherical reference frame [50].

The kite velocity $\mathbf{v}_\mathrm{k}$ can be decomposed into radial and tangential components $v_\mathrm{k,r}$

and $v_{k,\tau}$, respectively. The direction of $v_{k,\tau}$ is given by the course angle χ measured in the local tangential plane τ from the unit vector $\mathbf{e}_\theta$. The apparent wind velocity can be expressed in spherical coordinates (r,θ,ϕ) as

$$\mathbf{v}_a = \begin{bmatrix} v_{a,r} \\ v_{a,\theta} \\ v_{a,\phi} \end{bmatrix} = \begin{bmatrix} \sin\theta\cos\phi \\ \cos\theta\cos\phi \\ -\sin\phi \end{bmatrix} v_w - \begin{bmatrix} 1 \\ 0 \\ 0 \end{bmatrix} v_{k,r} - \begin{bmatrix} 0 \\ \cos\chi \\ \sin\chi \end{bmatrix} v_{k,\tau}. \tag{2.1}$$

The final model simulating the reel-out and reel-in phases of a system is formulated as an optimisation problem where the net electrical cycle power is maximised for given wind conditions. The fixed model inputs are the system design parameters, such as the kite wing area, aspect ratio, wing aerodynamic properties, tether properties, speed limits of the drum-generator module, etc. The optimisation variables are the operational parameters such as the stroke length (reeling distance over a cycle), pattern elevation angle, cone opening angle, turning radius at the start of the cycle, kite reeling speed and operating lift coefficient. The optimisation problem is constrained by physical limits such as the maximum tether force, tether length limit, minimum ground clearance, maximum operation height, etc.

Section 2.2.1 describes power extraction using the assumption of a massless kite on a straight tether at an elevation. Section 2.2.2 introduces a kite mass estimation function based on prototype data and scaling laws. Section 2.2.3 incorporates the effect of gravity on the power output. Section 2.2.4 describes the impact of the retraction phase on the net power output of the system. Section 2.2.5 introduces vertical wind shear, and finally, Section 2.2.6 describes the electrical cycle power of a system considering all the effects together.

2.2.1. MASSLESS KITE AT AN ELEVATION

Figure 2.2(a) illustrates the physical problem of a massless kite with a straight inelastic tether flying a circular pattern symmetric around the $\mathbf{X}_w$ axis. In the depicted instance along the flight path, the kite just passes through the $\mathbf{X}_w\mathbf{Z}_w$-plane and the wind vector $\mathbf{v}_w$ is orthogonal to the kite's tangential motion component. At this analysis stage, we assume a uniform and constant wind field, i.e. the wind speed and the direction do not change in time and space. The rotation of the wind reference frame is assumed to be so slow that the accelerations induced by this rotation are negligible. For any arbitrary point on the circular flight manoeuvre, fig. 2.2(b) shows the decomposition of velocity and force vectors in the $\mathbf{e}_r\mathbf{v}_a$-plane.

The assumption of a massless kite allows us to ignore the effects of gravity and inertia on the kite's motion. Since the tether cannot support a bending moment, the radial force balance is

$$F_t = F_a, \quad \text{where} \tag{2.2}$$

$$F_a = \frac{1}{2}\rho S\sqrt{C_L^2 + C_D^2}\, v_a^2. \tag{2.3}$$

Because of the assumed straight tether, the kite's radial speed $v_{k,r}$ is identical to the reel-out speed v_o. For any point on the flight trajectory, the apparent wind speed

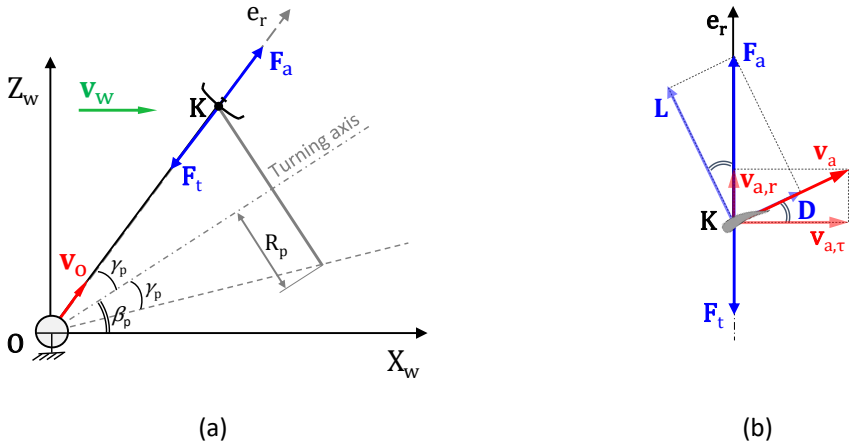

Figure 2.2: Velocities and forces for the massless kite at an elevation. (a) Side view illustrating the circular flight manoeuvre with average pattern elevation angle β_p, opening cone angle γ_p, reel-out speed v_o, and force equilibrium $\mathbf{F}_t + \mathbf{F}_a = 0$ at the kite. (b) Decomposition of velocity and force vectors in the $\mathbf{e}_r\mathbf{v}_a$-plane of the spherical reference frame for any arbitrary point on the trajectory.

can be expressed by its radial and tangential components as

$$v_a = v_{a,r}\sqrt{\left(\frac{v_{a,\tau}}{v_{a,r}}\right)^2 + 1}. \tag{2.4}$$

The radial component is defined by eq. (2.1) as

$$v_{a,r} = v_w \sin\theta\cos\phi - v_o. \tag{2.5}$$

The ratio of tangential and radial components of the apparent wind velocity is also known as the kinematic ratio as described in [50]. Because of the geometric similarity of velocity and force triangles illustrated in fig. 2.2(b), the kinematic ratio can be related to the lift-to-drag ratio,

$$\kappa = \frac{v_{a,\tau}}{v_{a,r}} = \frac{C_L}{C_D}. \tag{2.6}$$

From eqs. (2.2) to (2.6), the extractable mechanical power at the ground station can be computed as

$$P_{m,o} = F_t v_o \tag{2.7}$$

$$= \frac{1}{2}\rho S\sqrt{C_L^2 + C_D^2}(v_w \sin\theta\cos\phi - v_o)^2\left[\left(\frac{C_L}{C_D}\right)^2 + 1\right]v_o. \tag{2.8}$$

From this equation, one can conclude that increasing values of the elevation angle and azimuth angles decrease the magnitude of the apparent wind velocity vector. We simplify our formulation and represent one circular flight manoeuvre by a single flight state. During one full circular flight manoeuvre, the elevation angle β will vary from $\beta_p - \gamma_p$ to $\beta_p + \gamma_p$, where γ_p is the cone opening angle. The geometric average β_p over one full manoeuvre can be considered a representative elevation angle over the pattern. The effect of the azimuth angle differs from that of the elevation angle. Using the geometric average of the variation of the azimuth angle as a representative angle will result in $\phi_p = 0$ due to the negative and positive signs of the azimuth angle on either side of the symmetry plane $X_w Z_w$. But in reality, the kite flying on a circular manoeuvre is, on average, at a non-zero azimuth angle [51]. Therefore, we consider the geometric centre of the semicircle as a representative azimuth angle. The centroid y_c of a semicircle with radius R in the Cartesian reference frame is given by

$$y_c = \frac{4R}{3\pi}. \tag{2.9}$$

This translates to a specific azimuth angle in the spherical reference frame. For a given cone angle γ_p, the azimuth angle representing the centroid of a semicircle is

$$\phi_p = \sin^{-1}\left(\frac{4\sin\gamma_p}{3\pi}\right) \tag{2.10}$$

Therefore, it can be approximated that a representative point for the entire pattern, incorporating the average effect of elevation and azimuth is with $\theta = \pi/2 - \beta_p$ and $\phi_p = \sin^{-1}(4\sin\gamma_p/3\pi)$. The mean pattern reel-out power can now be estimated using eq. (2.7). The reel-out speed is an independent variable in our model, which is controlled by the ground station, and the tangential velocity is a result of the local force balance at the kite. The other dependent properties of the system are the tether dimensions, the kite's operational envelope, and the effective drag coefficient. They are computed as follows.

TETHER DIMENSIONS

For a given turning radius R_p and opening cone angle γ_p during operation, the required tether length is computed as

$$l_t = \frac{R_p}{\sin\gamma_p}. \tag{2.11}$$

For a given tether tensile strength σ_t and maximum allowable tether force $F_{t,max}$, the required tether diameter can be calculated as

$$d_t = \sqrt{\frac{4F_{t,max}}{\pi\sigma_t}}. \tag{2.12}$$

For ground-gen systems, the tether lifetime is driven primarily by fatigue due to bending and creep [71]. Hence, the tether will not be sized based on the material's ultimate breaking strength but on the optimal operating stress levels for an extended fatigue life.

KITE'S OPERATIONAL ENVELOPE

From eq. (2.7), one can see that the closer the tether is aligned with the wind velocity, the higher the power generated in crosswind operation. However, in a practical operation scenario, the kite must maintain a certain ground clearance h_{min}, and in most cases, respect a maximum operating height h_{max} for safety reasons and regulations. These limits must be considered when estimating the tether length and the operational height during the cycle. Figure 2.3 shows this geometrical relationship where $z_{\text{k,min}}$ and $z_{\text{k,max}}$ are the bottom-most and the top-most operating points during the cycle, $l_{\text{t,min}}$ and $R_{\text{p,min}}$ are the tether length and the turning radius at the start of the cycle, respectively. The operational height range of the kite is the unhashed vertical region between h_{min} and h_{max}. The region between the red dotted lines represents the actual operational envelope of the kite. This envelope changes since the optimal operating parameters change with respect to different wind conditions.

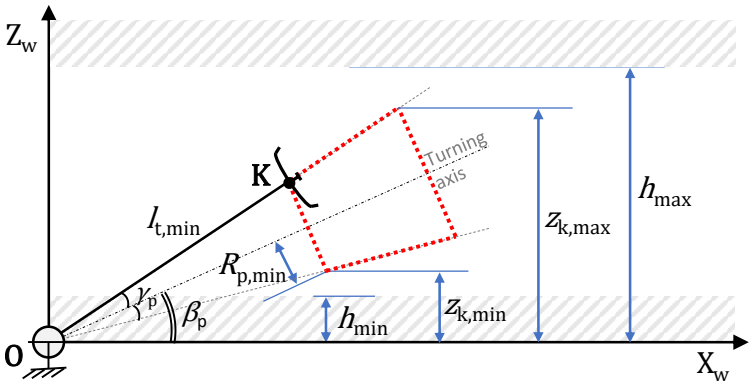

Figure 2.3: Side view illustrating the kite's operational envelope (region shown by the red dotted lines), and the operational height range (unhashed region between h_{min} and h_{max}).

Determining the minimum tether length $l_{\text{t,min}}$ using eq. (2.11), the minimum ground clearance h_{min} can be enforced by computing the kite's height at the bottom-most point of its circular flight manoeuvre

$$z_{\text{k,min}} = \frac{R_{\text{p,min}}}{\sin\gamma_{\text{p}}} \sin(\beta_{\text{p}} - \gamma_{\text{p}}), \tag{2.13}$$

such that $z_{\text{k,min}} \geq h_{\text{min}}$. The maximum operational height limit h_{max} can be enforced similarly by computing

$$z_{\text{k,max}} = \frac{R_{\text{p,max}}}{\sin\gamma_{\text{p}}} \sin(\beta_{\text{p}} + \gamma_{\text{p}}). \tag{2.14}$$

WING LIFT COEFFICIENT

We assume complete control over the kite by modulating the angle of attack to maintain the necessary wing lift coefficient C_L for optimal flight. Therefore, C_L is a variable in our model whose value is based on the lift polar. The maximum lift coefficient will set the upper limit considering some stall margins. This can be obtained from experimental measurements or computational analysis such as in [72].

EFFECTIVE DRAG COEFFICIENT

In addition to the wing drag, the tether is responsible for drag losses during operation. The tether drag contribution is assumed to be lumped to the kite, resulting in an effective drag of the combined kite and tether system [73]. To estimate this effective drag, it is assumed that the generated moment at the ground station equals the sum of the moments generated by the kite and the tether drag individually. The generated drag force is approximately perpendicular to the tether for high lift-to-drag ratios. We assume that the apparent velocity of the topmost segment of the tether is the same as that of the kite, and it uniformly drops to zero at the ground station. For a given tether length l_t, this moment equality can be mathematically expressed as

$$l_t D_{eff} = l_t D_k + \int_0^{l_t} l \frac{1}{2} \rho v_{a,l}^2 C_{d,t} d_t \mathrm{d}l \tag{2.15}$$

$$= l_t \frac{1}{2} \rho v_a^2 C_{D,k} S + \frac{1}{2} \rho \frac{v_a^2}{l_t^2} C_{d,t} d_t \int_0^{l_t} l^3 \mathrm{d}l, \tag{2.16}$$

where $C_{D,k}$ is the kite drag coefficient, $v_{a,l}$ is the apparent velocity of the tether element $\mathrm{d}l$ at a distance l from the ground station, d_t is the cross-sectional diameter, and $C_{d,t}$ is the cross-sectional drag coefficient of the tether.

This equation can be solved to estimate the effective drag coefficient

$$C_{D,eff} = C_{D,k} + C_{D,t}, \tag{2.17}$$

where,

$$C_{D,t} = \frac{1}{4} C_{d,t} d_t l_t \frac{1}{S}. \tag{2.18}$$

It is the effective drag coefficient of the tether lumped at the kite. The total drag of a wing is the sum of parasitic drag and lift-induced drag. Parasitic drag is comprised of a pressure drag contribution due to flow separation and a skin friction drag contribution. The induced drag is coupled to the generated lift [74]. For a given wing with aspect ratio $\mathcal{R}$ and wing planform efficiency (Oswald) factor e, the total kite drag coefficient can be expressed as

$$C_{D,k} = C_{d,min} + \frac{(C_L - C_{l,Cd,min})^2}{\pi \mathcal{R} e}, \tag{2.19}$$

where $C_{d,min}$ is the parasitic drag, C_L is the wing lift coefficient, and $C_{l,Cd,min}$ is the lift coefficient at $C_{d,min}$. As stated earlier, the drag polar can be obtained from experimental measurements or computational analysis such as in [72].

2.2.2. EFFECTIVE MASS ESTIMATE

Equation (2.2) does not consider the effect of gravity in the force equilibrium. This effect can be generally neglected during the reel-out phase for smaller systems, especially for low-mass soft-wing systems. This is because the gravitational force is much lower than the traction force. The main impact of weight for soft-wing systems is during the reel-in phase since they typically fly to higher heights because the lift-to-drag ratio is limited to a lower value. Gravity helps to reduce this height and shorten the reel-in phase [51]. This effect differs for larger and fixed-wing systems with higher mass [60]. Gravity reduces the attainable tether force and should be accounted for in the power extraction.

[75, 76] developed a model for mass scaling at the part level based on the 150 kW prototype AP3 and the MW level concept study AP4 developed by Ampyx Power B.V. The model uses the prototype as a reference system and applies known scaling laws for each structural part within the kite. The reference prototype was designed to meet aviation standards with relatively conservative safety factors. The prototype's architecture is scalable using a conventional design with ribs, spar caps, webs, etc. It is, therefore, assumed to be a good representation even for much larger fixed-wing kites. In the resulting mass model, the kite mass m_k is a non-linear function of the kite planform wing area S, aspect ratio AR, and maximum tether force $F_{t,max}$, given as

$$m_k = \left[\left(0.024\frac{F_{t,max}}{S} + 0.1\right)S^2 + \left(1.7\frac{F_{t,max}}{S} + 32.5\right)S - 50\right] \left[0.46\left(\frac{\mathit{AR}}{\mathit{AR}_{ref}}\right)^2 - 0.66\left(\frac{\mathit{AR}}{\mathit{AR}_{ref}}\right) + 1.2\right], \quad (2.20)$$

where $\mathit{AR}_{ref} = 12$, $F_{t,max}$ is in kN, S is in m^2, and m_k is in kgm. The physical meaning of the term $F_{t,max}/S$ corresponds to the wing loading for an aircraft. It states the maximum force it can handle per unit wing area and varies around 1-10 kNm^{-2} based on the purpose and size of the aircraft. Figure 2.4 is a plot of kite mass against wing area using the above equation and fixing $\mathit{AR} = 12$ and $F_{t,max}/S = 3.5\,kNm^{-2}$. These fixed values represent the AP3 150 kW prototype values. The result is compared against various data points compiled in [62]. As seen from the aircraft scaling curve [77], a conventional aircraft wing does not increase in mass as drastically as an AWE system kite. Based on available information, the MegAWES kite has $\mathit{AR} = 12$, and $F_{t,max}/S = 11\,kNm^{-2}$ [60]; AP2 has $\mathit{AR} = 10$; AP4 has $\mathit{AR} = 12$ and $F_{t,max}/S = 3\,kNm^{-2}$ [75, 78]; AP5 has $\mathit{AR} = 9.6$ and $F_{t,max}/S = 3.9\,kNm^{-2}$ [12]; M600 has $\mathit{AR} = 20$ and $F_{t,max}/S = 7.3\,kNm^{-2}$; MX2 has $\mathit{AR} = 12.5$ and $F_{t,max}/S = 4.6\,kNm^{-2}$ [79]; [80] has $\mathit{AR} = 26$ and $F_{t,max}/S = 12.4\,kNm^{-2}$.

Figure 2.5 shows a 3D scatter plot by varying all three parameters in eq. (2.20). As expected, the kite mass increases with increasing values of wing area, maximum allowable tether force and aspect ratio.

This mass model is based on the horizontal take-off and landing (HTOL) concept for the kite. A vertical take-off and landing (VTOL) concept will have different scaling due to the additional motors. Moreover, the fly-generation (FG) AWE system kites will also have a different scaling behaviour from that of GG systems. A more refined

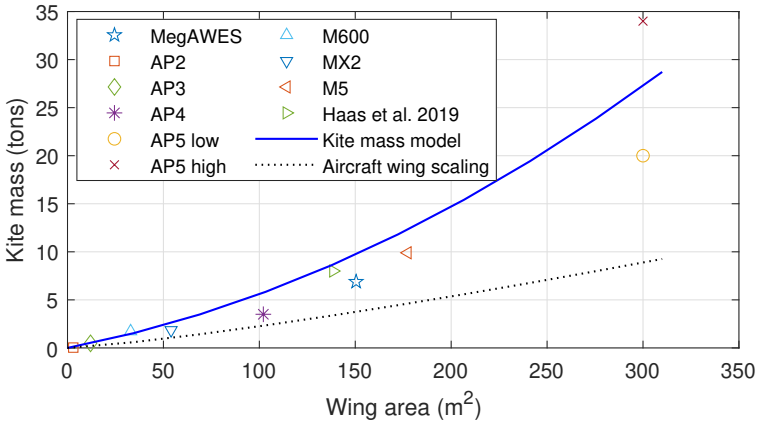

Figure 2.4: Kite mass as a function of wing area. Discrete data points from [62]. MegAWES: [60], Ampyx Power AP2, AP3, and AP4: [75, 78], AP5 low and AP5 high: [12], Makani Power M600, MX2 and M5: [79, 81], Haas et al. 2019: [80], Aircraft wing scaling: [77].

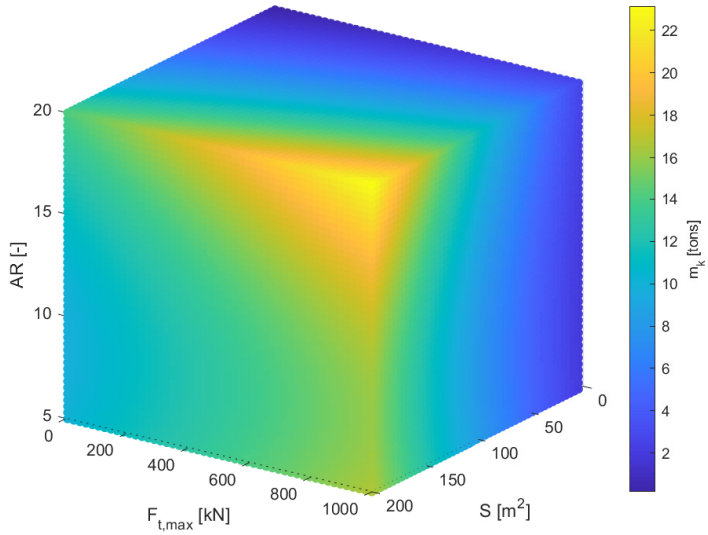

Figure 2.5: 3D scatter plot illustrating the relationship between wing area S, maximum tether force $F_{\mathrm{t,max}}$, and aspect ratio AR, with the kite mass m_{k}.

estimate of the kite mass is a complex interdisciplinary process which requires coupled aero-structural models such as in [82]. These models require knowledge of

many design and manufacturing details that are not known at the conceptual level and are highly specific to the design. They are also computationally demanding. We consider a simple mass model for the present work since we are not focused on absolute values but on the design trends within a large design space. The kite mass model in the present framework could be replaced by a coupled aero-structure model, which can give better mass estimates.

The minimum wind speed required by a static kite to compensate for the gravitational force and stay airborne, also known as the static take-off limit (STOL), will help us further understand the effect of mass. The STOL can be calculated as

$$v_{\mathrm{w,STOL}} = \sqrt{\frac{2m_{\mathrm{k}}g}{\rho S C_{\mathrm{L,max}}}}, \tag{2.21}$$

where $C_{\mathrm{L,max}}$ is the maximum operable wing lift coefficient. Table 2.1 shows the STOL for some of the prototypes. When the wind speeds are below the STOL for the particular kite, for example, during take-off, they need to be accelerated to achieve a higher apparent wind speed that allows compensation for the gravitational force. This implies that less heavy soft-wing kites, such as the TU Delft V3, could be launched at lower wind speeds without additional accelerating mechanisms for take-off. On the other hand, the heavier fixed-wing kites will always need to be accelerated to increase their apparent speeds.

Table 2.1: Static take-off limits for different prototypes. AP2: [75, 83], AP3: [72, 75], MegAWES: [60], MX2: [81], TU Delft V3: [84].

Kite	**Wing area** (m^2)	**Kite mass** (kg)	$\mathbf{C_{L,max}}(-)$	**STOL** (ms^{-1})
AP2	3	35	1.5	11.3
AP3	12	475	2.1	17.5
MegAWES	150.45	6885	1.9	19.8
MX2	54	1850	2	16.7
TU Delft V3	19.75	22.8	1	4.3

In addition to the kite mass, tether mass also affects power extraction and is assumed to be lumped together with the kite mass. To determine the equivalent lumped mass, we require that the moment generated at the drum equal the sum of the moments generated by the kite and the continuous tether individually [73]. For a specific tether length l_{t} and elevation angle β

$$l_{\mathrm{t}} m_{\mathrm{eff}} g \cos\beta = l_{\mathrm{t}} m_{\mathrm{k}} g \cos\beta + \int_0^{l_{\mathrm{t}}} l g \cos\beta \frac{\pi}{4} d_{\mathrm{t}}^2 \rho_{\mathrm{t}} \mathrm{d}l, \tag{2.22}$$

where g is the gravitational acceleration, d_{t} is the tether diameter, ρ_{t} is the tether material density, and $\mathrm{d}l$ is the length of the tether element at a distance l from the drum. This equation can be solved as

$$l_{\mathrm{t}} m_{\mathrm{eff}} = l_{\mathrm{t}} m_{\mathrm{k}} + \frac{\pi}{4} d_{\mathrm{t}}^2 \rho_{\mathrm{t}} \int_0^{l_{\mathrm{t}}} l \mathrm{d}l, \tag{2.23}$$

$$m_{\text{eff}} = m_{\text{k}} + \frac{1}{2} m_{\text{t}}, \tag{2.24}$$

where the tether mass varies with the deployed length of the tether during the cycle as

$$m_{\text{t}} = \frac{\pi}{4} d_{\text{t}}^2 \rho_{\text{t}} l_{\text{t}}. \tag{2.25}$$

2.2.3. EFFECT OF GRAVITY

If we consider the top point of the pattern during operation, shown in fig. 2.6, the aerodynamic force vector $\mathbf{F}_{\text{a}}$ has to tilt upwards to compensate for the kite's weight $\mathbf{F}_{\text{g}}$. This tilt is achieved by rolling the kite by an angle Ψ from the radial direction. In this model, the roll and the pitch are defined as orientation properties of the aerodynamic force vector relative to the radial direction. Along the manoeuvre, the aerodynamic force vector will continuously roll and pitch to counteract gravity. This effectively reduces the contribution of $\mathbf{F}_{\text{a}}$ to $\mathbf{F}_{\text{t}}$. Since $\mathbf{F}_{\text{g}}$ always points downwards, it does not have a component in the $\mathbf{e}_{\phi}$ direction. For the top point of the pattern, the quasi-steady force balance of $\mathbf{F}_{\text{t}}$, $\mathbf{F}_{\text{g}}$ and $\mathbf{F}_{\text{a}}$ in spherical coordinates is

$$\begin{bmatrix} -F_{\text{t}} \\ 0 \\ 0 \end{bmatrix} + \begin{bmatrix} -F_{\text{g}} \cos\theta \\ F_{\text{g}} \sin\theta \\ 0 \end{bmatrix} + \begin{bmatrix} F_{\text{a,r}} \\ F_{\text{a},\theta} \\ 0 \end{bmatrix} = 0. \tag{2.26}$$

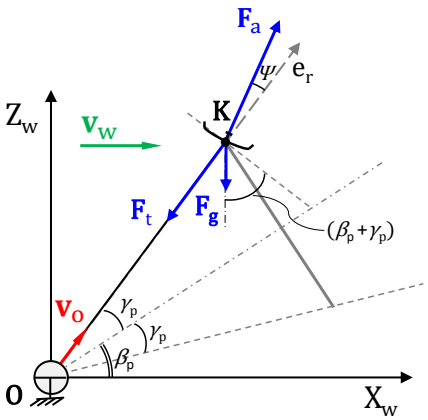

Figure 2.6: Side view illustrating the forces and velocities, including weight, during the reel-out phase of the kite at the top point of its circular manoeuvre.

Due to the tilting of $\mathbf{F}_{\text{a}}$ relative to the radial direction, the geometric similarity between the velocity and force triangles, as used to formulate eq. (2.6), is lost. Hence, the kinematic ratio κ cannot be substituted with the glide ratio. The mechanical reel-out power, in this case, becomes

$$P_{\mathrm{m,o}} = F_{\mathrm{t}} v_{\mathrm{o}} \tag{2.27}$$

$$= \left(\sqrt{\left(\frac{1}{2}\rho S\right)^2 (C_{\mathrm{L}}^2 + C_{\mathrm{D}}^2)(v_{\mathrm{w}} \sin\theta\cos\phi - v_{\mathrm{o}})^4 \left(\kappa^2+1\right)^2 - (F_{\mathrm{g}}\sin\theta)^2} - F_{\mathrm{g}}\cos\theta \right) v_{\mathrm{o}}. \tag{2.28}$$

As explained in [50] and [51], while maintaining the force balance given in eq. (2.26), there should be a solution for the kinematic ratio κ for which the decomposition of $\mathbf{F}_{\mathrm{a}}$ in $\mathbf{L}$ and $\mathbf{D}$ components corresponds to the glide ratio. By the definition of drag force, $D = (\mathbf{F}_{\mathrm{a}} \cdot \mathbf{v}_{\mathrm{a}})/v_{\mathrm{a}}$, and using $F_a = \sqrt{L^2 + D^2}$, we get the equation

$$\frac{L}{D} = \sqrt{\left(\frac{F_a v_a}{\mathbf{F}_{\mathrm{a}} \cdot \mathbf{v}_{\mathrm{a}}}\right)^2 - 1}. \tag{2.29}$$

This equation is a consistency constraint that must be respected for the solution of the kite speed within the force balance. The value for κ is solved numerically.

During the cyclic motion of the kite through the pattern, the apparent wind speed varies due to the aerodynamic work and the potential and kinetic energy exchange. The apparent wind velocity will be highest at the bottom and lowest on the topmost part of the pattern [60]. This variation in velocity leads to oscillations of the mechanical power. Although it should ideally not affect the pattern average power during the cycle, it will demand oversizing of the drivetrain to be able to handle the oscillation peaks. This will lead to increased costs and reduced overall efficiency since the drivetrain will not operate near its rated conditions most of the time. This undesired effect is more extreme for larger kite masses. The oscillating mechanical power must be capped if it exceeds the generator limit. This can be done in multiple ways, for example, by modulating the reeling speed or changing the angle of attack, which can both be done relatively quickly or by increasing the pattern elevation angle, which takes more time. The work of gravity during the upward and downward parts of the pattern is conserved, but at the same time, there are non-conservative forces, such as the drag force, which lead to energy dissipation. We choose the same representative point to evaluate the mean pattern reel-out power as discussed in Section 2.2.1. The power is estimated using eq. (2.27) with $\theta = \pi/2 - \beta_{\mathrm{p}}$ and $\phi_{\mathrm{p}} = \sin^{-1}(4\sin\gamma_{\mathrm{p}}/3\pi)$.

2.2.4. RETRACTION PHASE

At the end of the reel-out phase, when the kite is at the topmost point along its trajectory, it is assumed to be pulled back in a straight line starting from the top of the pattern, covering the reeled-out distance. This is as shown in fig. 2.6, but with the difference that the kite does not have a tangential velocity, i.e., the kite's tangential velocity component $v_{\mathrm{k},\tau} = 0$, with $\theta = \pi/2 - (\beta_{\mathrm{p}} + \gamma_{\mathrm{p}})$ and $\phi_{\mathrm{p}} = 0$. It only has a velocity in the negative radial direction. This is the reel-in velocity v_{i}, an independent variable in the model controlled by the ground station.

A force balance similar to the one described in Section 2.2.3 is solved to estimate the required mechanical reel-in power

$$P_{\mathrm{m,i}} = F_{\mathrm{t}} v_{\mathrm{i}} \tag{2.30}$$

$$= \left(\sqrt{\left(\frac{1}{2}\rho S\right)^2 \left(C_{\mathrm{L}}^2 + C_{\mathrm{D}}^2\right) \left[\left(v_{\mathrm{w}} \sin\theta \cos\phi + v_{\mathrm{i}}\right)^2 + \left(v_{\mathrm{w}} \cos\theta \cos\phi\right)^2 \right]^2 - \left(F_{\mathrm{g}} \sin\theta\right)^2} - F_{\mathrm{g}} \cos\theta \right) v_{\mathrm{i}}. \tag{2.31}$$

In contrast to the reel-out phase, gravity assists the kite in the retraction phase by reducing the required tether force for reeling in. When the reel-in speed is increased, the time required for reel-in can be decreased, but this increases the apparent speed, consequently increasing the tether force. To achieve this descent, the kite needs to modulate C_{L} to a lower value by pitching the kite. By doing so, the kite could be reeled in faster without necessarily increasing the tether force, hence minimising the required reel-in power. This trade-off should be captured when optimising the system's performance.

2.2.5. EFFECT OF VERTICAL WIND SHEAR

Since the kite gradually climbs from lower to higher heights during the reel-out phase, it is exposed to vertical wind shear. The wind resource varies with the height from location to location based on the ground surface roughness and other local meteorological parameters [11]. These vertical wind distributions can be modelled using meteorological data and exhibit significant diurnal and annual variations. [85] proposed a method to identify characteristic shapes of the wind profile using reanalysis data. Such characteristic wind profile shapes can be used with this model to evaluate the energy production of systems. Since an in-depth wind resource characterisation is not the focus of this work, the commonly used characterisation of a vertical wind profile in neutral atmospheric conditions using the power law given by

$$v_{\mathrm{w}}(z_2) = v_{\mathrm{w}}(z_1) \left(\frac{z_2}{z_1}\right)^{\alpha}, \tag{2.32}$$

is used to describe the relationship between wind speed v_{w} and height z based on the ground surface roughness parameter α [86].

To account for the changing inflow during the system's operation, the reel-out phase is discretised in several segments as shown in fig. 2.7. The tractive power is evaluated for each segment using the corresponding wind speed and resulting force balance. The orange points represent the numerical evaluation points during the reel-out and reel-in phases.

2.2.6. ELECTRICAL CYCLE POWER OPTIMISATION

The power represented by eq. (2.27) is the average mechanical reel-out power over one pattern for a given wind speed. This does not yet account for the losses due

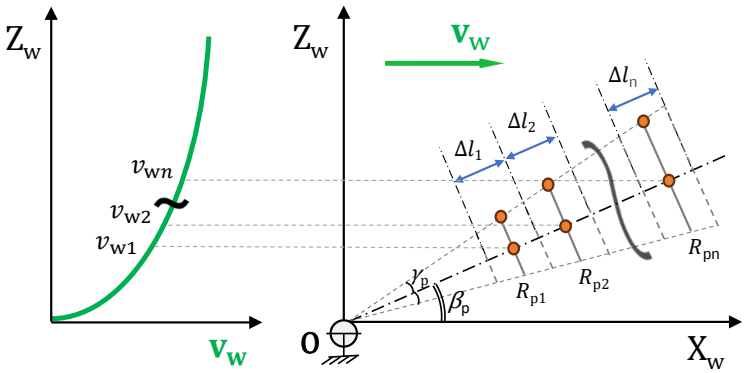

Figure 2.7: The discretised reel-out phase experiences different wind speeds as an effect of the vertical wind shear.

to the power consumed in the reel-in phase and the losses in the drivetrain. The drivetrain is the chain of components between the drum of an AWE system and the point of connection to the electricity grid. Since the power output of a ground-gen AWE system is cyclic, a storage component needs to be used to charge and discharge during the cycle to maintain smooth power fed into the grid [87]. The electrical cycle average power is computed as

$$P_{\mathrm{e,avg}} = \frac{P_{\mathrm{e,o}}\, t_{\mathrm{o}} - P_{\mathrm{e,i}}\, t_{\mathrm{i}}}{t_{\mathrm{o}} + t_{\mathrm{i}}}, \quad \text{where} \tag{2.33}$$

$$P_{\mathrm{e,o}} = P_{\mathrm{m,o}} \eta_{\mathrm{DT}}, \quad \text{and} \tag{2.34}$$

$$P_{\mathrm{e,i}} = \frac{P_{\mathrm{m,i}}}{\eta_{\mathrm{DT}}}. \tag{2.35}$$

Here, t_{o} is the time duration of the reel-out phase, $P_{\mathrm{e,i}}$ is the power required during reel-in, t_{i} is the time duration of the reel-in phase, η_{DT} is the drivetrain efficiency.

DRIVETRAIN EFFICIENCY

In a typical electrical drivetrain, the generator is connected to the drum using a gearbox. The generator is then connected to an electrical storage module via a power converter and to the grid via a power converter in parallel configuration [66, 87]. Therefore, η_{DT} is a combination of the individual component efficiencies given as

$$\eta_{\mathrm{DT}} = \eta_{\mathrm{gb}} \eta_{\mathrm{gen}} \eta_{\mathrm{pc}} \eta_{\mathrm{sto}} \eta_{\mathrm{pc}}, \tag{2.36}$$

where η_{gb} is the gearbox, η_{gen} is the generator, η_{sto} is the electrical storage, and η_{pc} is the power converter efficiencies, respectively. We assume a value of 95% for all the three components except the generator. The generator efficiency at its rated speed could be as high as 95% and drops steeply below about 40% of its rated speed. This non-linear relationship is based on the supplier data received from Ampyx Power

B.V. and is modelled as

$$\eta_{\text{gen}} = 0.671\left(\frac{v}{v_{\text{rated}}}\right)^3 - 1.4141\left(\frac{v}{v_{\text{rated}}}\right)^2 + 0.9747\left(\frac{v}{v_{\text{rated}}}\right) + 0.7233, \tag{2.37}$$

where v is the operating speed of the generator. Figure 2.8 shows this generator efficiency plot.

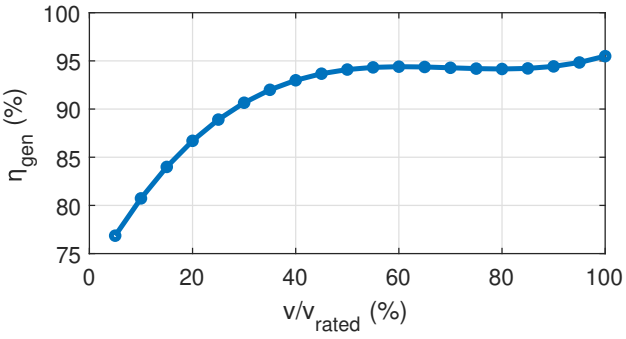

Figure 2.8: Generator efficiency as a function of the ratio of its operating speed with respect to its rated speed.

REEL-OUT AND REEL-IN TIME

The reel-out and reel-in times heavily influence the average electrical cycle power of the system. They are dependent on the reel-out speed v_{o}, reel-in speed v_{i}, stroke length Δl, and the given maximum drum acceleration $a_{\text{d,max}}$. Figure 2.9 shows a velocity-time graph for a representative cycle. The reel-out phase starts with a reeling speed of zero. The kite achieves its set reel-out speed by accelerating with $a_{\text{d,max}}$ and remains constant until the kite covers the stroke length. The kite then decelerates back to zero to begin the reel-in phase. Similar to the start of the reel-out phase, the reeling speed reaches its set value by accelerating with $a_{\text{d,max}}$ and then remains constant till the end of the reel-in phase, after which it again decelerates to zero to begin a new cycle.

If t_1 is the time taken by the kite to reach the maximum reel-out speed, $t_{\text{o,eff}}$ is the effective time during which the kite is in traction, and is producing power, t_2 is the time taken by the kite to reach its maximum reel-in speed, and $t_{\text{i,eff}}$ is the effective time during which the system is out of traction, then the cycle time is expressed as

$$t_{\text{cycle}} = t_{\text{o}} + t_{\text{i}} = t_{\text{o,eff}} + t_1 + t_{\text{i,eff}} + t_2, \quad \text{i.e.} \tag{2.38}$$

$$t_{\text{cycle}} = \frac{\Delta l}{v_{\text{o}}} + \frac{v_{\text{o}}}{a_{\text{d,max}}} + \frac{\Delta l}{v_{\text{i}}} + \frac{v_{\text{i}}}{a_{\text{d,max}}}. \tag{2.39}$$

OPTIMISATION PROBLEM SETUP

The optimisation objective is maximising the electrical cycle average power $P_{\text{e,avg}}$, given by eq. (2.33), for given wind conditions. Table 2.2 shows the list of the

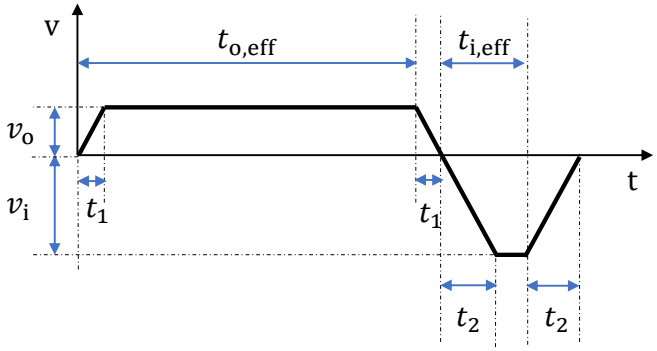

Figure 2.9: Velocity-time graph for a representative cycle.

operational design parameters, which are the variables of the optimisation problem. In general, the upper and lower bounds on the variables should be set such that the optimum is not restricted by the bounds. This will change if component limitations are considered. For example, the limits on the kite speed v will depend on the drivetrain's maximum allowable speed, and the operational wing lift coefficient C_L will depend on the wing aerodynamic properties. Since this is a steady-state model without a controller, the lower limit on the pattern radius R_p could be set based on studies considering a controller such as [82, 88]. To account for the feasibility of trajectories in this model, we propose a lower limit on the turning radius of $5b$, where b is the wing span.

Table 2.2: Operational parameters which are optimised for given wind conditions.

Design variable	Unit	Description
Δl	m	Stroke length
β_p	deg.	Pattern elevation angle
γ_p	deg.	Pattern cone opening angle
$R_{p,min}$	m	Initial turning radius
v_o	m/s	Reel-out speed
$C_{L,o}$	-	Reel-out wing lift coefficient
v_i	m/s	Reel-in speed
$C_{L,i}$	-	Reel-in wing lift coefficient

Table 2.3 presents the list of the constraints of the optimisation problem. Constraints are enforced on the minimum ground clearance, required electrical rated power, peak mechanical power (limiting the size of the generator), maximum tether length, maximum allowable tether force, and minimum number of patterns per cycle. At least one full pattern during a cycle is imposed to account for the fact that inertial effects are excluded, and it can be unrealistic to have fast transitions between reel-out and reel-in without completing at least one circular trajectory.

Another important constraint that must be respected during reel-out and reel-in is given by eq. (2.29). Since the design space is continuous and has non-linear constraints, sequential quadratic programming (SQP), a gradient-based optimisation algorithm, is implemented in MATLAB to solve the problem. The results give the optimal operation set-points for the defined system with respect to the given wind conditions.

Table 2.3: Optimisation problem constraints.

Constraint	Unit	Description
$h_{\text{min}} \leq z_{\text{k}} \leq h_{\text{max}}$	m	Operation height limits
$P_{\text{e,avg}} \leq P_{\text{rated}}$	W	Electrical rated power
$P_{\text{m,o}} \leq P_{\text{gen,rated}}$	W	Peak mechanical power
$l_{\text{t}} \leq l_{\text{t,max}}$	m	Maximum tether length
$F_{\text{t}} \leq F_{\text{t,max}}$	N	Maximum tether force
$N_{\text{p}} \leq N_{\text{p,min}}$	-	Minimum number of patterns per cycle

The optimiser attempts to find a solution for the quasi-steady force balance for every wind speed in the given range. The cut-in wind speed $v_{\text{w,cut-in}}$ is the minimum speed at which the system produces net positive electrical cycle power. That is, for wind speeds below $v_{\text{w,cut-in}}$, power will be consumed to keep the kite in the air ($P_{\text{e,avg}} < 0$). The rated wind speed $v_{\text{w,rated}}$ is the speed at which the system produces its nameplate-rated electrical power. Therefore, the cut-in and the rated wind speeds are part of the solution. On the other hand, the cut-out wind speed $v_{\text{w,cut-out}}$ is a design choice and will most probably be a consequence of the structural lifetime and design limits of the system components. Following conventional wind turbines, the cut-out wind speed is assumed to be $25\,\text{ms}^{-1}$ at the operational height.

This cycle power computation model implemented in MATLAB is available open-source through Zenodo and GitHub [89].

2.3. RESULTS AND DISCUSSION

The attainable power curve for a fixed-wing ground-gen AWE system can be estimated using the presented model. Results from simulating a system with a rated power of 150 kW are presented in Section 2.3.1 and some effects of scaling are discussed in Section 2.3.3, showcasing the capabilities of the model and its application for the conceptual design phase.

2.3.1. SIMULATION RESULTS OF A 150 KW SYSTEM

The system's parameters are based on the prototype AP3 (fig. 2.10), originally developed by Ampyx Power [72, 75], and since 2023 continued by Mozaero [90]. Table 2.4 lists the parameters and the limits used to define the specific system. It is important to note that the system parameters are not optimised, and hence, the power curve does not characterise a commercial 150 kW system. A safety factor

Figure 2.10: First, untethered flight of the AP3 demonstrator aircraft in the Netherlands, in November 2023 [90]. Photo courtesy of Mozaero.

$\eta_{t,gust}$ is applied on $F_{t,max}$, reducing the maximum allowable tether force value below the actual limit of the tether. To account for 3-D wing aerodynamic effects, an aerodynamic efficiency factor is applied on the maximum airfoil lift coefficient, setting an upper limit for the wing lift coefficient C_L. This is given as

$$C_{L,max} = \eta_{C_l} C_{l,max}, \tag{2.40}$$

where η_{C_l} is the efficiency factor and $C_{l,max}$ is the maximum airfoil lift coefficient. For the induced drag calculation using eq. (2.19), a wing planform efficiency factor e (Oswald efficiency factor) is used.

Figure 2.11 shows the chosen vertical wind shear profile representing an onshore scenario and neutral atmospheric conditions using a surface roughness coefficient α of 0.143. The figure also shows wind profiles from Cabauw, an onshore location and Ijmuiden, an offshore location in the Netherlands. These two profiles were generated using the wind profile clustering approach described in [85] and were utilised in [60]. For any given location, several profiles exist based on the probability of occurrence. The profiles with the highest probabilities in the two locations are shown in the figure. The modelled profile with $\alpha = 0.143$ is comparable to the empirical onshore profile and hence is chosen to represent a generic onshore location.

POWER CURVE COMPARISON WITH 6-DOF SIMULATION

The six-degree-of-freedom (6-DoF) simulation results were generated using the simulation framework developed at Ampyx Power B.V., such as described in [58, 78, 83]. This model accounts for three degrees of freedom related to the kite's attitude and three related to its position. Unlike steady-state modelling, it solves the equations of motion, including the acceleration terms. The wing's aerodynamic derivatives are obtained through computational analysis, as described in [72]. The tether is modelled as a flexible component with discretised segments. Flight and

Table 2.4: Model input parameters list.

Parameter	Description	Value
α	Wind shear coefficient	0.143
S	Wing surface area	$12\,\mathrm{m}^2$
AR	Wing aspect ratio	12
$C_{\mathrm{l,max}}$	Max. airfoil lift coefficient	2.5
η_{C_l}	Airfoil efficiency factor	0.80
$C_{\mathrm{l,Cd,min}}$	Lift coefficient at minimum drag coefficient	0.65
$C_{\mathrm{d,min}}$	Minimum drag coefficient	0.056
e	Wing planform efficiency factor	0.60
$F_{\mathrm{t,max}}$	Max. allowable tether force	42 kN
$\eta_{\mathrm{t,gust}}$	Gust margin factor	0.90
σ_t	Tether material strength	$7 \times 10^8\,\mathrm{Nm}^{-2}$
ρ_t	Tether material density	$980\,\mathrm{kgm}^{-3}$
$C_{\mathrm{d,t}}$	Cross-sectional tether drag coefficient	1.2
$l_{\mathrm{t,max}}$	Max. tether length	1000 m
h_{min}	Min. ground clearance	100 m
h_{max}	Max. operating height	1000 m
P_{rated}	Rated electrical power	150 kW
$P_{\mathrm{gen,rated}}$	Generated mechanical power limit	375 kW
$v_{\mathrm{d,max}}$	Max. tangential drum speed	$20\,\mathrm{ms}^{-1}$
$a_{\mathrm{d,max}}$	Max. tangential drum acceleration	$5\,\mathrm{ms}^{-2}$
$N_{\mathrm{p,min}}$	Minimum number of patterns per cycle	1

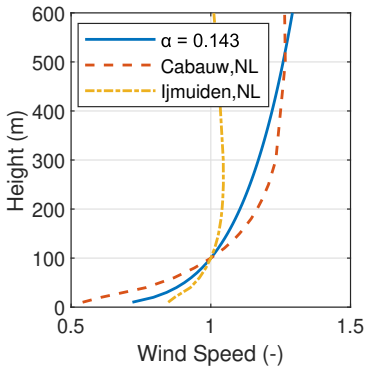

Figure 2.11: The chosen vertical wind shear profile with a surface roughness coefficient of 0.143 compared against profiles from Cabauw, an onshore location, and Ijmuiden, an offshore location in the Netherlands [60].

winch feedback controllers are implemented to simulate the tethered kite system during take-off, reel-out, reel-in, transition and landing phases.

Figure 2.12 shows the computed power curve compared to the ideal crosswind power extraction theory by [63] and the results of the 6-DoF simulation. The

horizontal axis describes the wind speed at 100 m height. Loyd's ideal crosswind power is computed using

$$P_{\text{Loyd}} = \frac{4}{27}\frac{C_{\text{L,max}}^3}{C_{\text{D}}^2}\frac{1}{2}\rho S v_{\text{w}}^3, \tag{2.41}$$

where $C_{\text{L,max}}$ is the upper limit as defined by eq. (2.40), C_{D} is computed as described in eq. (2.19), and v_{w} is the wind speed at 100m height. This ideal crosswind theory overpredicts the power because it neglects the losses due to gravity, elevation and azimuth angles, tether drag, cyclic operation, hardware limits and drivetrain efficiency.

The kite mass m_{k} using eq. (2.20) comes out to be 437 kg, which is close to the indication received from the company about the AP3 prototype, as seen from fig. 2.4. The shape of the estimated power curve using the developed model resembles the curve generated by the 6-DoF simulations, but it is more optimistic. This is mainly because the developed model ignores the losses due to control and inertial effects. It also does not account for realistic take-off or flight sustenance conditions at low wind speeds, which is most likely the reason for the earlier cut-in. The rated power is reached at the wind speed of 15 ms^{-1}. As a design choice, the cut-out wind speed is chosen to be 25 ms^{-1} at the operational height. Due to the vertical wind shear, this translates to a wind speed of 21 ms^{-1} at 100 m.

The mean mechanical and electrical, reel-out and reel-in powers, and the electrical cycle average power, are shown in fig. 2.13 and fig. 2.14. The reel-out power has three regimes, as described in [65, 75]. The cubic regime I is above the cut-in speed (here, 6 ms^{-1}), in which the reel-out power increases cubically until 10 ms^{-1} when the maximum allowable tether force (here, 34 kN, considering the gust margin factor) is reached. The linear regime II starts when reaching the maximum allowable tether force, in which the reel-out power increases linearly till the chosen rated electrical power (here, 150 kW) is reached. The flat regime III starts when reaching the rated power and continues till the cut-out speed. In this regime, the mechanical reel-out power is capped to maintain the rated electrical power. The power is capped by varying the operational parameters. These changes in operational parameters also affect the reel-in power seen in fig. 2.14.

FORCES AND OPERATIONAL PARAMETERS FOR THE ENTIRE WIND SPEED RANGE

Figure 2.15 and fig. 2.16 show the resultant aerodynamic force, the tether force and the gravitational force during the reel-out and reel-in phases, respectively. As specified in Table 2.4, a gust margin factor of 0.9 is applied to the maximum allowable tether force. Once this upper limit is reached, the aerodynamic force has to be capped to avoid tether overload. In our specific example, this limit is reached at 10 ms^{-1}. The aerodynamic force can be capped by reducing the wing's lift coefficient, modulating the reeling speed, or increasing the elevation angle. The choice of a specific capping strategy depends on multiple trade-offs. The optimisation objective is the average electrical cycle power, including the reel-out and reel-in phases. During reel-in, the kite is flown such that the maximum contribution of the generated aerodynamic force is used to counter the kite's weight,

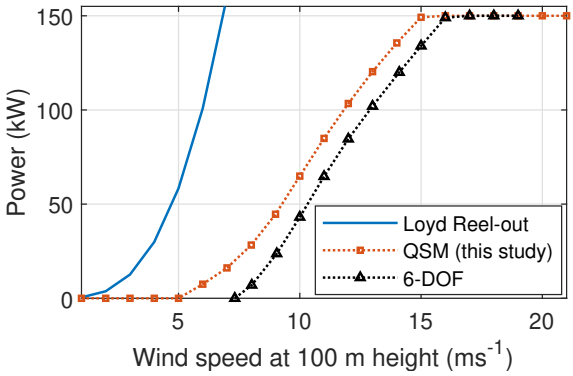

Figure 2.12: Power curve comparison of the quasi-steady-model (QSM) with Loyd and 6-DoF simulation results.

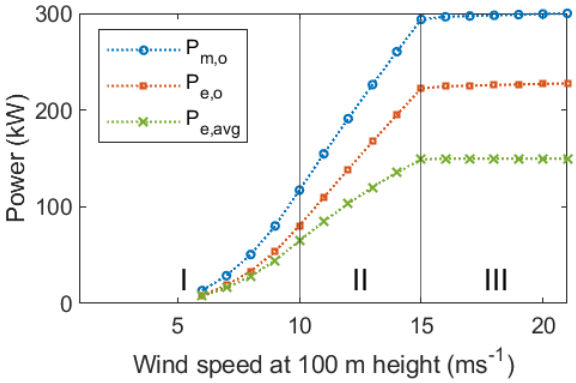

Figure 2.13: Mean mechanical power $P_{\mathrm{m,o}}$, electrical reel-out power $P_{\mathrm{e,o}}$, and electrical cycle average power $P_{\mathrm{e,avg}}$ as functions of the wind speed.

reducing the required pulling force and, consequently, the reel-in power. This is seen in fig. 2.16. Intuitively, if the aerodynamic force completely balanced the weight, it would lead to a $F_{\mathrm{t,i}} = 0$ and hence no requirement of reel-in energy. This would be the case of a freely gliding kite. However, this could also increase the reel-in time, which could lead to lower net cycle power. Hence, the optimiser finds a solution to the reel-in speed such that it creates a non-zero tether force but still ultimately reduces the net cycle loss.

Figure 2.17 and fig. 2.18 shows the lift and drag coefficients during the reel-out and reel-in phases. As stated earlier, C_{L} is a variable in our model and C_{D} is calculated using eq. (2.17). The aerodynamic force during reel-in only has to counter the kite's weight, which is achieved by decreasing the lift coefficient during reel-in. Because of the lift-induced drag contribution, the kite drag coefficient is a function of the

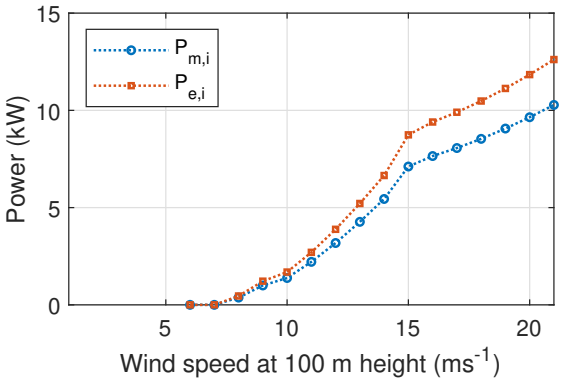

Figure 2.14: Mean mechanical reel-in power $P_{\mathrm{m,i}}$ and electrical power $P_{\mathrm{e,i}}$ as functions of the wind speed.

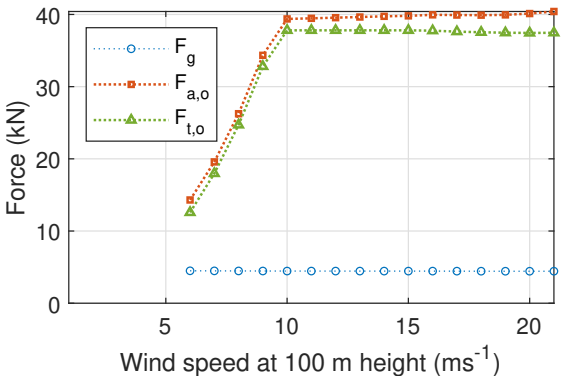

Figure 2.15: Mean resultant aerodynamic force $F_{\mathrm{a,o}}$, tether force $F_{\mathrm{t,o}}$, and weight of the kite and the tether lumped together F_{g} during the reel-out phase, as functions of the wind speed.

lift coefficient and follows its trend. The total drag coefficient is the summation of the kite drag coefficient and the tether drag coefficient as described in eq. (2.17). Figure 2.18 shows that the tether drag coefficient contributes significantly to the system's total drag coefficient. It is almost equal to the kite drag coefficient during the reel-out phase and is higher during the reel-in phase.

The kite's radial and tangential velocity components are commonly non-dimensionalised with the wind speed, leading to the reeling factor $f = v_{\mathrm{k,r}}/v_{\mathrm{w}}$, and the tangential velocity factor $\lambda = v_{\mathrm{k,\tau}}/v_{\mathrm{w}}$ [50]. Figure 2.19 shows the tether reeling factors during reel-out and reel-in and the tangential velocity factor during reel-out. The reel-out speed peaks when the rated power is reached, i.e. at $15\,\mathrm{ms}^{-1}$ of wind speed, and then gradually reduces, assisting in power capping. The reel-in

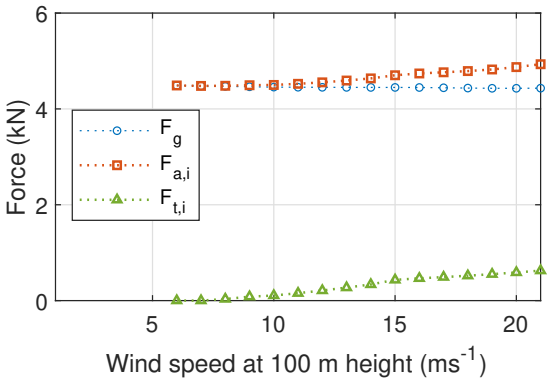

Figure 2.16: Mean resultant aerodynamic force $F_{a,i}$, tether force $F_{t,i}$, and weight of the kite and the tether lumped together F_g during the reel-in phase, as functions of the wind speed.

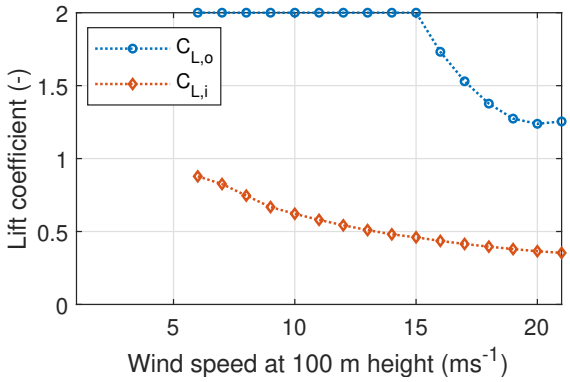

Figure 2.17: Mean kite lift coefficients $C_{L,o}$ and $C_{L,i}$ during the reel-out and reel-in, respectively, as functions of the wind speed.

speed is kept at the drum's tangential speed limit of $20\,\mathrm{ms}^{-1}$. This is seen from the gradual decrease of the reel-in speed factor. After the maximum tether force is reached at $10\,\mathrm{ms}^{-1}$, the kite's tangential velocity is gradually reduced, decreasing the aerodynamic force to maintain the tether force at its maximum value.

Figure 2.20 shows the reel-out time, reel-in time, average time the kite takes to perform one circular pattern during reel-out, and the number of patterns per cycle. The number of patterns is calculated using the reel-out time, pattern radius and tangential kite speed as

$$N_p = \frac{t_o}{2\pi R_p/(v_{k,\tau})}. \tag{2.42}$$

In a more realistic operation, the number of patterns should be a whole number

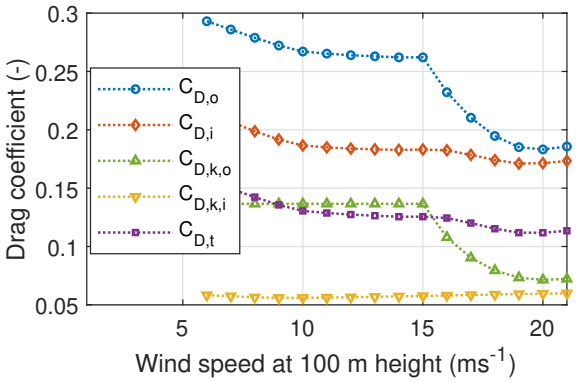

Figure 2.18: Mean effective system drag coefficients $C_{D,o}$ and $C_{D,i}$, mean kite drag coefficients $C_{D,k,o}$ and $C_{D,k,i}$ during the reel-out and reel-in, respectively, and the mean tether drag coefficient $C_{D,t}$, as functions of the wind speed.

such that the reel-in phase always starts from the top point of the pattern. However, since we are not resolving the full trajectory in this model, the number of patterns is allowed to be a fractional result. Moreover, since inertial effects are ignored in this model, the full cycle time durations are optimistic. Realistic cycle times will increase due to the transition phase between reel-out and reel-in, which is unaccounted for in this model.

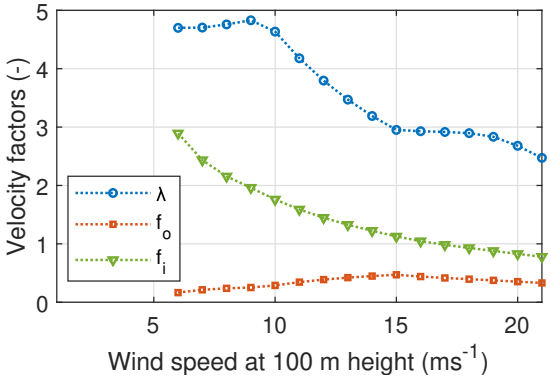

Figure 2.19: Mean kite tangential speed factor λ, reel-out factor f_o, and reel-in factor f_i, as functions of the wind speed.

Figure 2.21 shows the average pattern height, pattern radius, stroke length, maximum tether length, and minimum tether length. The average pattern height is the height of the centre point of the pattern at half of the stroke length.

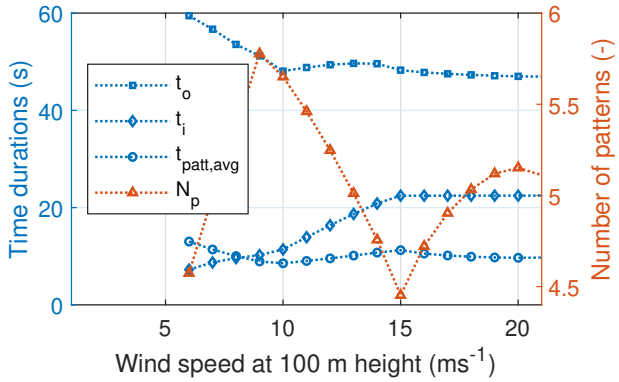

Figure 2.20: Reel-out time t_o, reel-in time t_i, average pattern time $t_{patt,avg}$, and number of patterns per cycle N_p, as functions of the wind speed.

The minimum tether length and, consequently, the pattern radius and height are primarily driven by the ground clearance constraint, pattern elevation angle and the cone opening angle. In reality, they will also be influenced by the effect of the centrifugal force, which is ignored in the quasi-steady approach. As the elevation angle increases, the required minimum tether length is reduced. The maximum tether length is driven by the optimised stroke length.

Figure 2.22 shows the roll, pattern elevation, and opening cone angles. The roll angle is the deviation of the resultant aerodynamic force vector with respect to the radial direction. The pattern elevation angle increases with the wind speed. This quasi-steady flight state results from the trade-off between the increase in incoming wind speed, an increase in cosine losses due to gravity and a decrease in reel-in power with a higher elevation angle. The optimiser trades all these factors to maximise the average cycle power at each wind speed.

FORCES AND OPERATIONAL PARAMETERS OVER ONE CYCLE

The maximum convertable power is limited by the generator-rated power, which in our specific example is 375 kW, as given in Table 2.4. To enforce this hardware limit in the third wind speed regime, the operational parameters have to be modulated. Figure 2.23 shows the mechanical, electrical and electrical cycle power over a single pumping cycle at the rated wind speed of 15 ms^{-1}. The delivered rated power of 150 kW is the electrical cycle average power. The difference in instantaneous mechanical and electrical power is due to the drivetrain efficiency.

The power profile during the cycle has a slight downward trend during the reel-out and an upward trend during the reel-in. This is explained using fig. 2.24. For the quasi-steady state evaluation, the reel-out phase is discretised into five segments arranged in sequence on the horizontal axes of the diagrams. The cycle begins with a tether length of around 400m, and the reel-out phase ends with a tether length of around 700m. The average pattern height and the pattern radius increase during

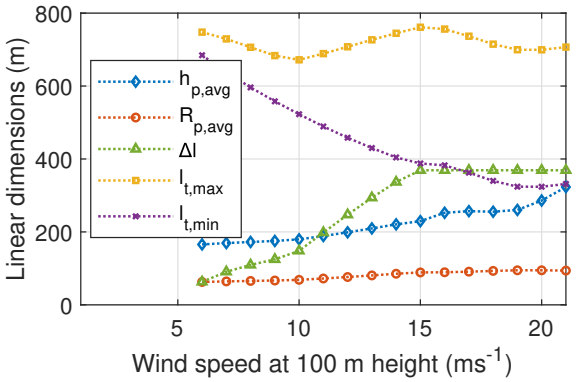

Figure 2.21: Average pattern height $h_{\mathrm{p,avg}}$, average pattern radius $R_{\mathrm{p,avg}}$, stroke length Δl, maximum tether length $l_{\mathrm{t,max}}$, and minimum tether length $l_{\mathrm{t,min}}$, as functions of the wind speed.

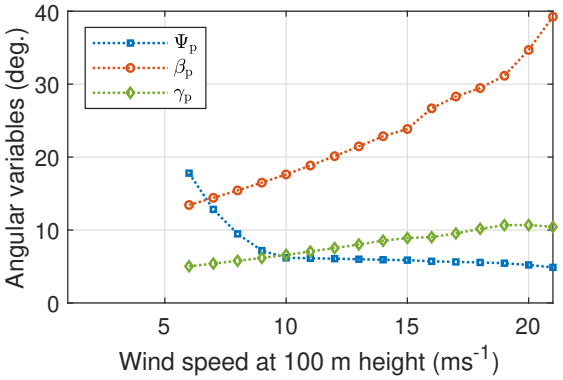

Figure 2.22: Mean roll angle Ψ_{p}, average pattern elevation angle β_{p}, and opening cone angle γ_{p}, as functions of the wind speed.

the reel-out phase. Due to the gain in height, the kite experiences a higher wind speed v_{w} as it climbs up. Due to the increasing tether length, the overall drag of the system increases, and hence, the glide ratio decreases. Hence, to respect the relation given by eq. (2.29), the kite speed has to drop, reflected in the reeling and tangential velocity factors. Since the tether force is already maximised, the overall power decreases due to a lower reel-out speed.

2.3.2. EFFECT OF GRAVITY

Figure 2.25 shows the power curve comparison between two simulations, one with and one without, including the effect of gravity (i.e. weight). Gravity has a negative impact on operation at low wind speeds because this affects the attainable reel-out

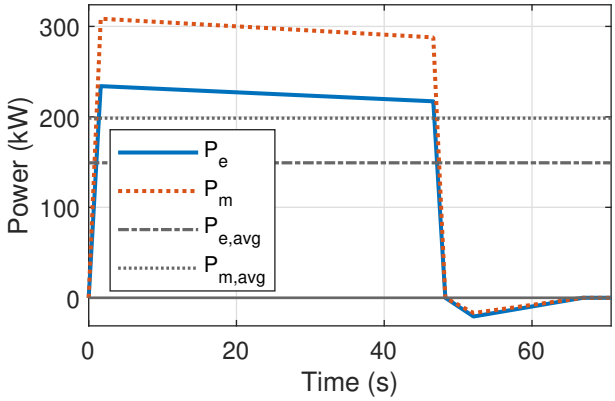

Figure 2.23: Instantaneous powers P_e and P_m together with net powers $P_{e,avg}$ and $P_{m,avg}$ over one pumping cycle at rated wind speed of $15\,ms^{-1}$.

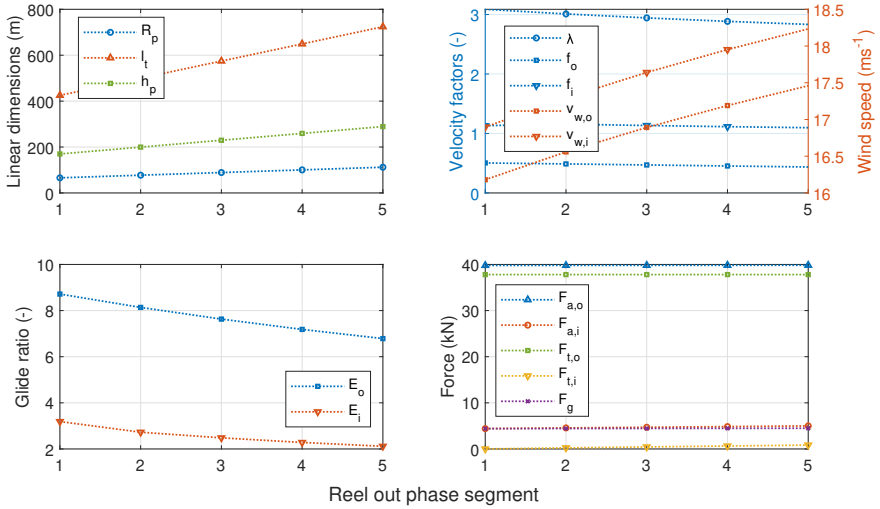

Figure 2.24: Evolution of parameters over the discretised reel-out phase in five segments at rated wind speed of $15\,ms^{-1}$.

power substantially. Hence, the simulation without gravity yields better performance at lower wind speeds than the one including gravity. But for higher wind speeds, this effect is superseded by its impact on the reel-in phase. As explained in Section 2.2.4, the weight assists in the retraction phase, positively impacting the net cycle power output. The kite is pitched in such a way that the resultant aerodynamic force vector balances the gravitational force vector, hence reducing the tether force magnitude in the quasi-steady force balance. The kite can be retracted faster without consuming a

lot of energy.

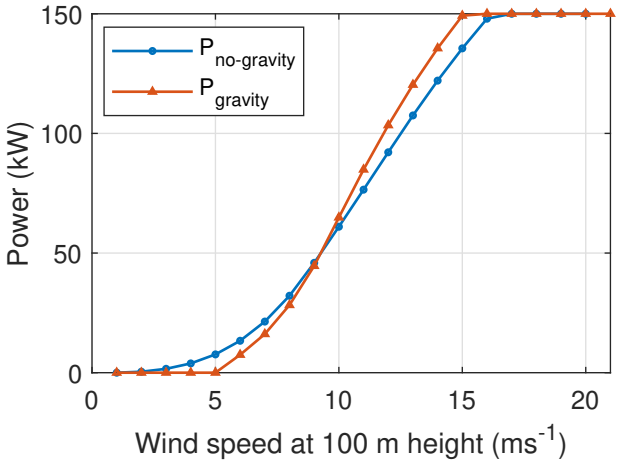

Figure 2.25: Power curve comparison with and without the effect of gravity.

Figure 2.26 and fig. 2.27 detail the effect of gravity over a pumping cycle for a lower wind speed of $6\,\mathrm{ms}^{-1}$ and the rated wind speed $15\,\mathrm{ms}^{-1}$. The reel-out power without the effect of gravity is substantially higher at $6\,\mathrm{ms}^{-1}$ than at $15\,\mathrm{ms}^{-1}$. The net difference between the energy generated during reel-out and consumed during reel-in leads to higher net average power for the case without gravity at $6\,\mathrm{ms}^{-1}$ than at $15\,\mathrm{ms}^{-1}$. This shows that excluding gravity in the analysis does not necessarily lead to optimistic results. In any case, including gravity should always be the more realistic simulation for the pumping cycle.

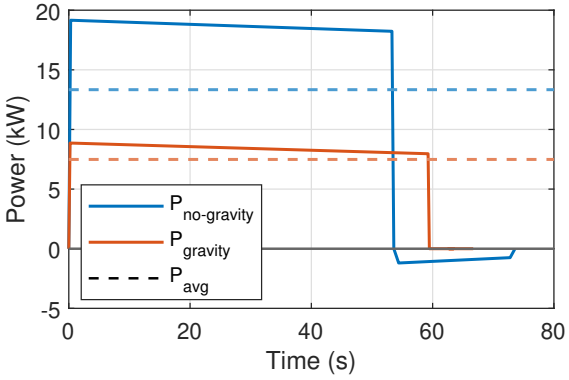

Figure 2.26: Cycle power comparison with and without the effect of gravity for low wind speed of $6\,\mathrm{ms}^{-1}$.

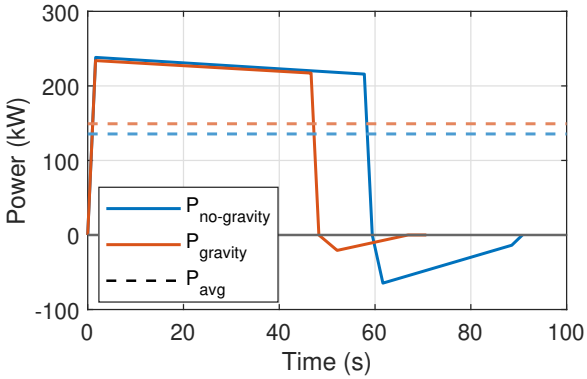

Figure 2.27: Cycle power comparison with and without the effect of gravity for higher wind speed of 15 ms^{-1}.

2.3.3. EFFECT OF SCALING

One of the primary purposes of this model is to capture the effects of scaling on the performance of fixed-wing AWE systems. Due to the interdisciplinary nature of AWE systems, multiple trade-offs must be considered. The kite and the tether are the primary aspects affecting the system's performance. The performance metric used is the power harvesting factor ζ defined as

$$\zeta = \frac{P}{P_w S}, \tag{2.43}$$

where P is the extracted mechanical power and $P_w S$ is the available power in the wind. This metric is based only on the reel-out power and does not consider the reel-in power. The force a tether can withstand for a given material strength is proportional to its diameter as shown in eq. (2.12). The kite should also be able to withstand this tether force; hence, with increasing tether force, the structural mass of the kite increases to support the increasing wing loading. Though increasing the tether force will enable the extraction of more power, the consequent increase in kite mass will decrease the performance. Also, the contribution of tether drag will increase with increasing diameter, consequently penalising the extractable power.

Figure 2.28 shows the effect of tether diameter on the performance of an AWE system. For a kite with the same wing area, the mass increases with increasing tether force as given in eq. (2.20). This increase in kite mass negatively impacts the attainable reel-out power. For this simulation, the performance is maximum when using a tether of diameter of around 3.8 cm. Similarly, fig. 2.29 shows the effect of scaling the wing area on the performance of an AWE system. For the chosen tether, the kite wing area which maximises power is 50 m^2.

Figure 2.30 shows the effect of the tether diameter on the performance of a system with a fixed kite wing area of 100 m^2 for the complete operational wind speed range. As seen from fig. 2.28, the kite mass of a system with smaller tether tension is lower.

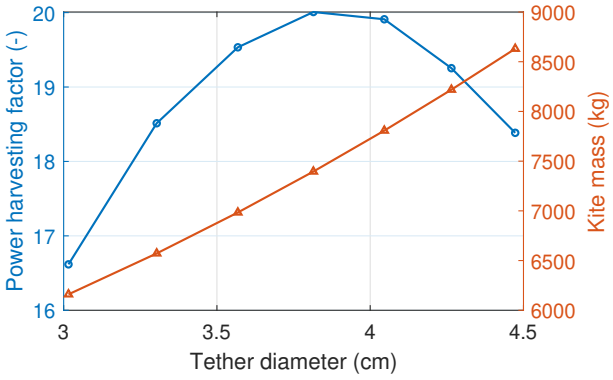

Figure 2.28: Effect of tether diameter on the performance of an AWE system with a fixed kite wing area of 100 m^2 at a constant wind speed of 12 ms^{-1}.

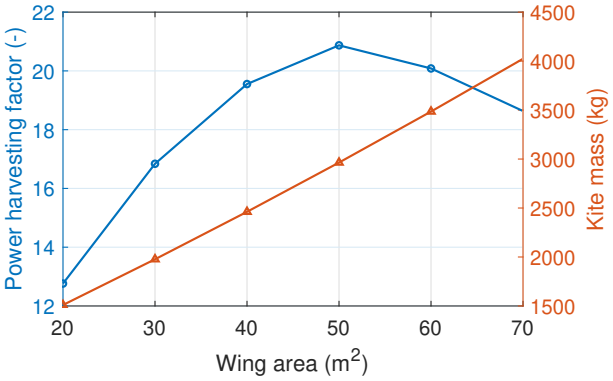

Figure 2.29: Effect of wing area on the performance of a system with fixed tether diameter of 2.7 cm at a wind speed of 12 ms^{-1}.

Lighter kites will experience lower gravitational loss and, hence, will perform better at lower wind speeds. At higher wind speeds, the maximum tether force limits the extractable power. Therefore, for a given wing area, systems with thinner tethers, i.e. lower $F_{t,max}$, perform better at lower wind speeds, and systems with larger tethers, i.e.higher $F_{t,max}$, perform better at higher wind speeds.

Figure 2.31 shows the wing area's effect on a system's performance with a fixed wing-loading for the complete operational wind speed range. Fixed wing loading is used instead of a fixed tether force since simulation results of a high tether force coupled to a small kite and vice-versa do not converge for the entire operational wind speed range. A larger tether force demands a stronger kite, resulting in a heavier one. This configuration cannot produce positive net cycle power at low wind speeds. Therefore, the choice of tether force for a given wing area must fall

in a certain range to have converged results for the entire operational wind speed range. The system performs better with increasing wing area, but these gains are diminishing since the penalising effect of the gravitational force scales faster than the performance gain.

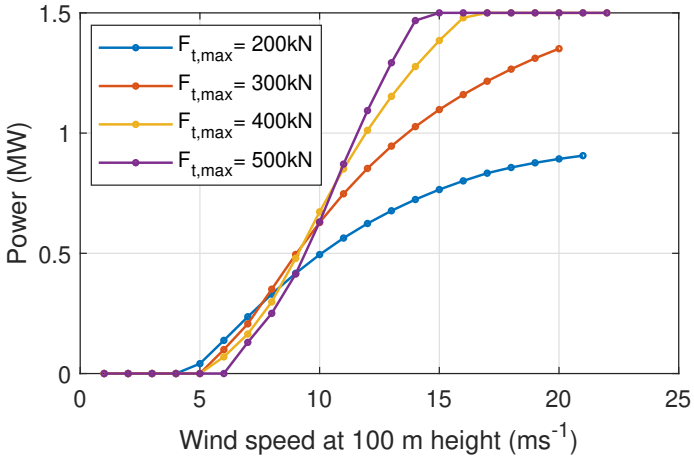

Figure 2.30: Effect of scaling the tether (diameter) on the performance of a system with a fixed kite wing area of 100 m^2 for the complete operational wind speed range.

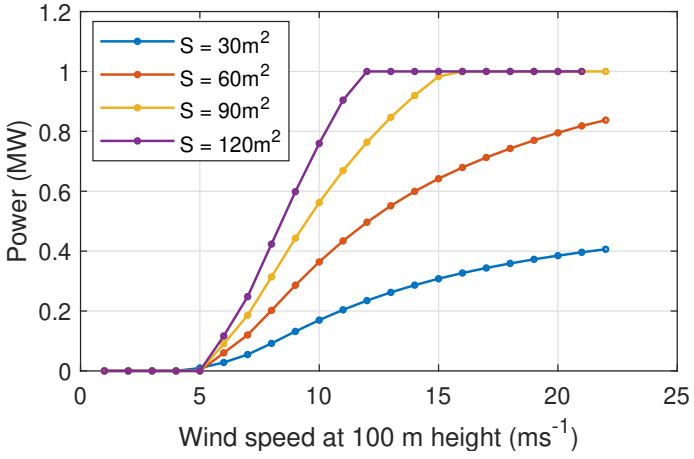

Figure 2.31: Effect of scaling the wing area on the performance of a system with a fixed wing-loading of 3 kNm^{-2} for the complete operational wind speed range.

2.3.4. DISCUSSION

The results show that the proposed model captures all relevant dependencies between the system components, allowing the evaluation of different trade-offs at play. Since the model is based on a quasi-steady flight motion, the results are expected to be optimistic predictions of a real system's performance. Since the model relies on a limited set of input parameters defining an AWE system, it is suitable for coupling with similar-fidelity cost models, as proposed in [91]. The present modelling approach does not account for the various effects of inertia responsible for losses in the different operational phases.

For example, centrifugal acceleration is important during sharp turning manoeuvres, and its effect needs to be balanced by an aerodynamic side force component. A fixed-wing kite generates this side force component by rolling towards the turning axis, reducing the aerodynamic force available for conversion into electricity, thus, representing a loss. On the other hand, the path-aligned acceleration introduces a history term in the kite's equations of motion, affecting the temporal progress along the flight path. For relatively lightweight soft-wing kites, these two inertial effects have only a minor effect on the power output and are thus generally neglected. However, with increasing mass-to-wing surface ratio the contribution of inertia becomes more important. An accompanying study by [92] showed that for heavier kites, the different acceleration terms can lead to quite complex superposition effects. Because it is not possible to account for all acceleration terms in a quasi-steady modelling framework, we decided to neglect all inertial effects and instead use existing 6-DoF dynamic simulation results for validation.

Also, the transition times between the reel-out and reel-in phases are not considered in the present modelling framework. Because of the alternating loading and unloading of the airborne subsystem, the tether alternates between straightening and sagging. Straightening and sagging take time while no work is performed. The kite moves radially away or towards the ground while the winch does not reel. This hysteresis effect represents a loss for the pumping cycle operation. [60] found that the kite needs to be slowed down at the start and the end of the transition phase to avoid tether rupture due to the change in the magnitude of forces. This effect is also known as the "whiplash effect". The present model cannot estimate the reel-out power oscillations due to the acceleration and deceleration of the kite when it follows the prescribed flight path.

The model and simulation results in this paper are not validated against measurement data. Skysails Power Gmbh, a German company, released a certified power curve of their PN-14 system based upon the standard IEC 61400-12-1 used for conventional wind turbines [93]. They reported good agreement of their measurements with their simulation results. Figure 2.32 shows an overlay of their measurements against the 150kW simulation results from Section 2.3.1. This is not a performance comparison since the technologies and their system characteristics differ significantly, but the systems do have similar power ratings. The IEC standard requires multiple changes considering the differences between conventional wind turbines and AWE systems. For instance, the definition of the reference height, wind range, method of averaging over time, incorporating the number of cycles in

averaging, etc. The reference height proposed by Skysails is 200m, which is closer to the average operational height of their system. Alignment on the reference height for wind speed measurements while communicating the power curve is essential for fair comparisons. As the AWE sector advances rapidly, there is a need for dedicated IEC standards to validate the power curve of AWE systems.

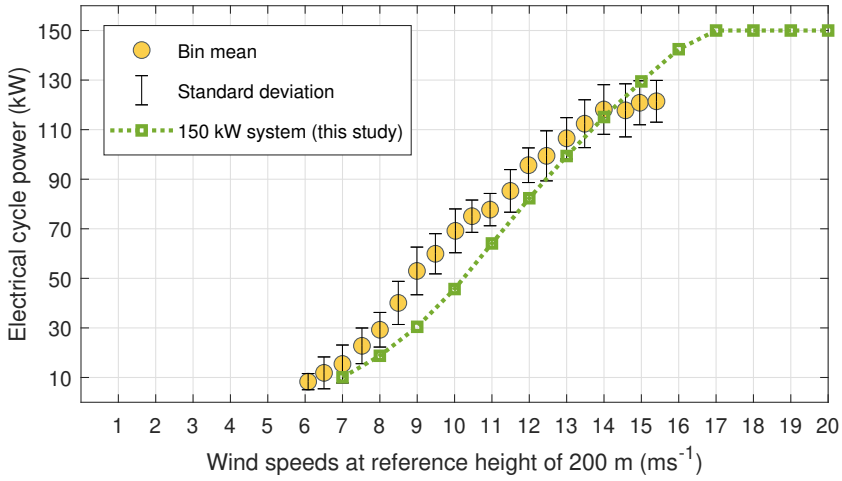

Figure 2.32: Overlay of the power curve of the 150kW system over Skysails' validated power curve of SKS PN-14 [93].

2.4. KEY-TAKEAWAYS

The quasi-steady model presented in this paper enables fast power curve computations based on a limited set of input parameters. It is useful for understanding the fundamental physical behaviour of fixed-wing ground-generation AWE systems and is suitable for sensitivity analysis and estimating AWE systems' theoretical potential. The model can easily be coupled to systems engineering tools, cost models, and larger-scale energy system models. It may thus help to create technology development road-maps, investigate the scaling potential, and define research targets to validate assumptions.

The kite mass is a key parameter influencing the performance of systems, primarily at lower wind speeds. A higher mass leads to a larger component of the generated aerodynamic force needed to compensate for the gravitational force, reducing the usable mechanical power. On the other hand, gravity positively impacts performance at higher wind speeds by reducing the required energy during reel-in. The tether diameter and the kite's structural mass are coupled to design an optimised system. The maximum force-bearing capacity of the tether is directly proportional to the diameter of the tether, and a higher tether force requires a structurally stronger kite. Hence, choosing a tether with a larger force-bearing capacity also increases

the kite mass, negatively impacting the low wind speed performance but enabling higher power extraction at higher wind speeds. This trade-off becomes critical for choosing the optimal tether-kite combination based on site-specific requirements. Upscaling results in a diminishing gain in performance with an increase in kite wing area. Integrating the prescribed model in a system design optimisation framework provides a computational design tool that accounts for the multiple trade-offs for site-specific design. The system design parameters, such as the kite wing area, generator rating, tether diameter, etc., can be optimised to maximise the annual energy production for a specific wind resource. Moreover, annual energy prediction alone will not give the right indication for system design since this metric lacks the influence of costs. To include this important aspect, the presented model can be coupled to a cost model to find the system design that minimises the levelised cost of energy.

Since the presented model is based on the assumption of quasi-steady flight motion, it does not account for inertial effects. These will be significant for larger AWE systems; hence, the model is likely too optimistic in estimating their performance. This approach occupies a middle ground between ideal power extraction and fully resolved dynamic simulations. The outcomes of this analysis define the upper limits that practical systems might approach. Consequently, these models are valuable for determining whether and under what conditions AWE could benefit the entire energy system.

3

DRIVETRAIN CONCEPTS FOR POWER SMOOTHING

Chapter 2 described the developed power curve model for fixed-wing ground-generation airborne wind energy (AWE) systems. The pumping AWE systems have an oscillating power profile that requires smoothing before being supplied to the electricity grid. This chapter proposes three drivetrain concepts as a solution to this power smoothing challenge. The three concepts are based on three different types of storage technologies: electrical, hydraulic and mechanical.

The outline of this chapter is as follows. Section 3.2 presents the three drivetrain concepts. Section 3.3 presents a case study on sizing and costing the three drivetrain concepts for a MW-scale AWE system. Section 3.4 presents the conclusions that provide guidance to AWE developers for choosing a suitable drivetrain concept for their systems.

This chapter has been adapted from the following peer-reviewed article:

[87] R. Joshi, D. von Terzi, M. Kruijff, and R. Schmehl. "Techno-economic analysis of power smoothing solutions for pumping airborne wind energy systems". In: Journal of Physics: Conference Series 2265 (4 May 2022), p. 042069. ISSN: 1742-6588. DOI: 10.1088/1742-6596/2265/4/042069.

3.1. WHAT IS POWER SMOOTHING?

In the reel-out phase, the kite is operated in crosswind repetitive patterns, pulling the tether from a winch that drives a generator and produces electricity on the ground. Once the tether has reached its maximum length, it is reeled back into its starting position. This reel-in phase consumes a small fraction of the produced electricity. Alternating reel-in and reel-out phases in pumping cycles leads to a net production of electricity. Figure 3.1 shows a simulated cycle power output of a pumping AWE system using the performance models introduced in [78, 83]. The integral area in green represents the power production phase, and the one in red represents the consumption phase of the cycle. It should be noted that this power profile does not represent a commercial system operation but is a representation of the pumping cycle.

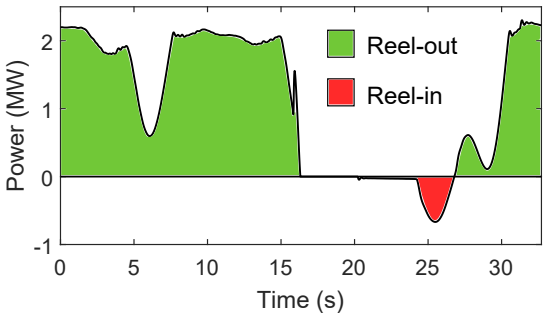

Figure 3.1: Instantaneous power profile during one full cycle of a pumping AWE system at a certain wind speed.

Until recently, the priority of AWE developers has been the kite and its flight operation. However, many companies are now approaching the commercialization phase, which requires a focus on the integration of the generation side with the electricity grid. Compliance with grid codes could be challenging for pumping AWE systems due to their oscillating power profile. In Europe, the European Network of Transmission System Operators for Electricity (ENTSO-E) [94] prescribes the requirements from power generators for integration with the electricity grid. The primary requirement is to maintain the power ramps within prescribed tolerance bands at the point of common coupling. Depending on the country, the power ramps for wind and solar PV in Europe should be within 10-20% of the active power within the timescale of a minute [95–97]. Therefore, power smoothing is an inherent requirement of the pumping AWE systems for connecting to the grid. This can be achieved by utilizing an intermediate storage device between the system and the point of the grid connection.

An important aspect is looking at farm-level power smoothing with synchronized operation of AWE systems. But this may be a future solution. It is relevant to study the system level smoothing for the initial systems since they can then be installed in a wider range of settings with less customization. This increases the addressable

market. The first AWE systems will likely be installed in weak grids, where power smoothing is essential. However, early installations are likely to be individual systems or in small numbers, where farm-level smoothing is not feasible.

The objective of this chapter is to gain insights into the potential power smoothing solutions for AWE systems based on their efficiencies, costs, maturity, integration challenges and other trade-offs. Note that this chapter does not focus on the detailed technical feasibility of the solutions but rather on the first-order techno-economic comparison.

3.2. POWER SMOOTHING SOLUTIONS - DRIVETRAIN CONCEPTS

Power smoothing essentially means providing a constant power output to the grid irrespective of the fluctuations during cycle operation. The power profile of the AWE systems, i.e. the cycle average, the peaks, and the reel-out and reel-in times, are different for different wind speeds. The primary function of the power smoothing solution is to provide constant power to the grid at all times and for every wind speed. This can be done by maintaining the net cycle average to the grid at all times. Figure 3.2 shows the amount of energy to be stored and discharged during the cycle operation to maintain the net cycle average power to the grid during the complete cycle. The green region corresponds to the excess energy being stored during the reel-out phase, and the red region corresponds to the release of this stored energy back to the grid during the reel-in phase. This is assuming that the average mechanical power for every wind speed and the efficiency of the drivetrain is known. A set point for power to the grid at every wind speed should be maintained by the controller based on the wind speed and the system data. A buffer in the storage could be maintained to accommodate the real-time changes in wind speeds and the controller reaction time.

The intermediate energy storage for power smoothing must be capable of delivering a high number of charge-discharge cycles with a fast response. Conventional electrical energy storage batteries are not suitable for such operations. Supercapacitors, hydro-pneumatic accumulators and flywheels are storage technologies used in a wide range of energy recovery applications, including smoothing the delivery of power, dampening vibrations and reducing fluctuations, to name only a few. Based on these three energy storage technologies, three corresponding drivetrain concepts are proposed in this chapter.

3.2.1. ELECTRICAL DRIVETRAIN

Primary components of the electrical drivetrain are shown in fig. 3.3. Supercapacitors are electrochemical energy storage devices that store and release energy at a much faster rate (approx. 300 times) than lithium-ion batteries. Since supercapacitors are electrical storage devices, mechanical energy at the winch needs to be converted to electricity before connecting to the supercapacitor. Electrical generators have an operating speed and torque region for maximizing power conversion efficiency.

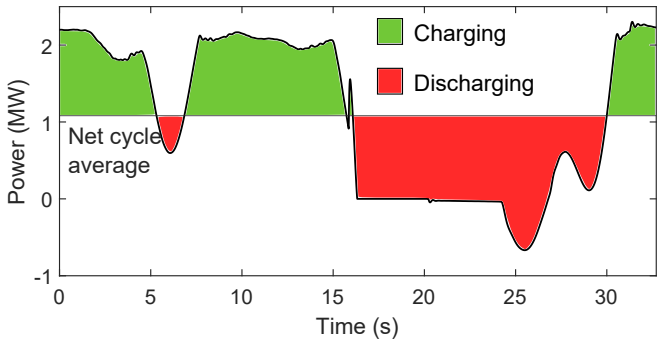

Figure 3.2: Representative charging and discharging integral areas to maintain the net cycle average to the grid at all times for a certain wind speed

Depending on the AWE system, the speed of the winch during the pumping cycle might not be in that operating region. Therefore, a gearbox might be necessary to use as a coupling between the winch and the generator.

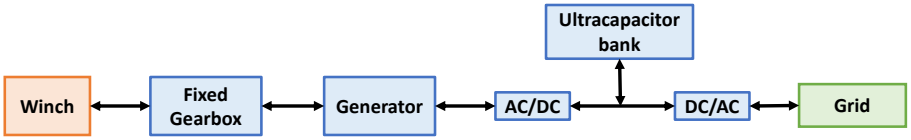

Figure 3.3: Architecture of a fully electric power smoothing solution

The generator is directly coupled to the winch. Hence, it needs to be sized for peak load in the operating wind speed range instead of rated power. This will lead to under-utilization of the generator and is the most important disadvantage of the electrical concept. Due to this, the generator is operated at part load for a significant amount of time. This affects the power conversion efficiency. Supercapacitors are DC devices and have specific operating conditions. Electronic power converters are required at both ends to convert the electric power to the required voltage and frequency levels. The generator-side power converter needs to be sized for peak load like the generator, and the grid-side convertor for rated power. During the reel-out phase, energy equal to the net cycle average is supplied directly to the grid and the excess energy is stored in the supercapacitor. During the reel-in phase, the stored energy is supplied to the grid, and a fraction of it is used to drive the winch for reeling in. Multiple supercapacitor banks are needed for this simultaneous operation.

3.2.2. HYDRAULIC DRIVETRAIN

Primary components of the hydraulic drivetrain are shown in fig. 3.4. This drivetrain was first introduced in [98]. A hydro-pneumatic accumulator is a vessel capable of

storing energy in the form of a compressed gas. The accumulator has two chambers divided by a separator. The difference in the types of these accumulators lies in the kind of separator element used. The three most common types of hydro-pneumatic accumulators are using a bladder, a diaphragm or a piston. The first chamber is a fluid chamber, usually filled with hydraulic oil, and the second is a gas chamber, usually containing nitrogen. The fluid chamber is connected to the hydraulic circuit. During charging, the fluid pressurizes the separator element and compresses the gas. During discharging, the compressed gas is released to exert the pressure back on the fluid.

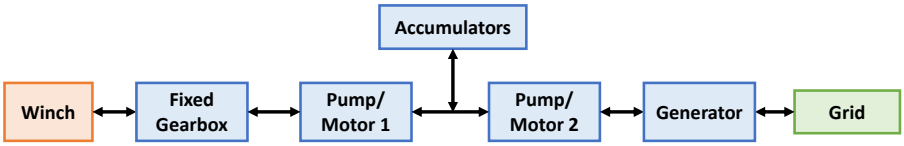

Figure 3.4: Architecture of a hydraulic power smoothing solution

The idea behind this drivetrain is to avoid oversizing the electrical generator. The two hydraulic machines can work either as a pump or a motor. Depending on the hydraulic machine technology, a gearbox might be necessary to couple the first hydraulic machine with the winch. The winch drives the first hydraulic machine in the reel-out phase, which pumps the hydraulic fluid into the accumulator under high pressure. Energy equal to the net cycle average is released with a constant pressure to drive the second hydraulic machine, and excess energy is stored in the accumulator. During the reel-in phase, the stored energy is released to drive the first hydraulic machine as a motor for reeling in and the second hydraulic machine as a motor to drive the electricity generator.

3.2.3. MECHANICAL DRIVETRAIN

This drivetrain concept is conceptualized by Ampyx Power [41] and MAZARO [99]. The primary components are shown in fig. 3.5. The flywheel uses the mechanical power at the winch to store the energy based on the conservation of angular momentum. This drivetrain requires a niche transmission technology called the reversible variable transmission (RVT). The flywheel-side shaft rotates in one direction only, but during reel-in, the winch needs to be rotated in the opposite direction. RVT is necessary for this operation. RVT is a niche component, and hence, a fixed gearbox might be needed to couple the RVT to the winch to align the operation speed and torque regions. The efficiency of the flywheel is maximum when it is operating at its maximum speed. The speed of the generator shaft must also be regulated constantly. Consequently, a variable ratio gearbox is needed to couple the generator shaft and the flywheel to maximize efficiency.

During the reel-out phase, the energy equal to the net cycle average is supplied to the grid and the excess energy is stored in the flywheel. During the reel-in phase, the stored energy is supplied to the grid and the winch. The RVT changes the direction

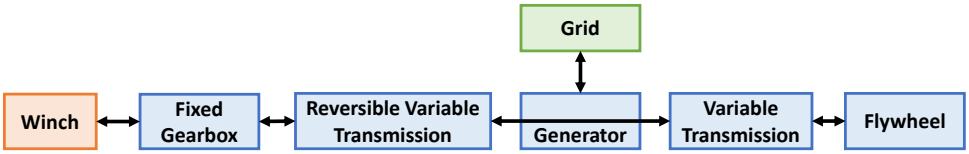

Figure 3.5: Architecture of a mechanical power smoothing solution

of rotation on the winch side for reeling in.

3.3. CASE–STUDY: DRIVETRAIN SIZING AND COSTING FOR A MW–SCALE AWE SYSTEM

The framework used to compare and evaluate differences between the three power smoothing solutions is shown in fig. 3.6. It is based on process workflow modelling to simulate the energy flow between the drivetrain components. The drivetrain models require two inputs: (1) The time series data of the operation of the AWE system (speed, torque) and (2) reference costs and efficiency values associated with the AWE system and the drivetrain components. The developed drivetrain models estimate the sizing and costing of each component based on the logic of power smoothing as described in Section 3.2.

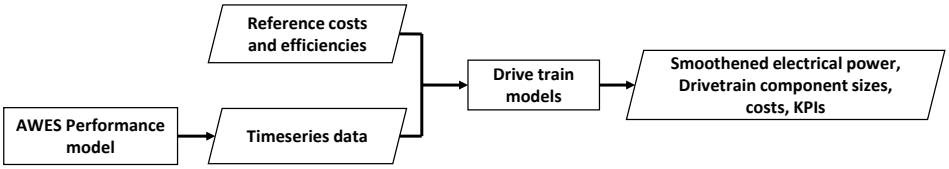

Figure 3.6: Techno-economic framework used to compare the three drivetrain concepts

This analysis is performed considering a single standalone MW-scale pumping AWE system. The time series data are generated using the dynamic six DOF performance model introduced in [78, 83]. The data used is a general representation of the power profiles of the pumping AWE systems and, hence, of the underlying power smoothing requirements.

Techno-economic analysis requires cost and efficiency estimates of the components involved. This information is highly variable, and it is based on different technologies, suppliers, and country-specific regulations. Efforts have been made to use realistic cost and efficiency assumptions based on direct communication with the industry wherever possible. Ampyx Power is currently testing its 150kW system with a fully electrical drivetrain. Inputs regarding the hydraulic concept have been provided by Bosch Rexroth [100]. The mechanical concept is based on products offered by [99, 101, 102]. Cost references for gearboxes, power converters and electrical generators

are obtained from [103]. Additional inputs for cost, efficiency, energy density, power density and other qualitative attributes of storage technologies have been obtained from [104–108].

The average efficiency values of the components in the three drivetrain concepts are given in table 3.1. In the electrical concept, since the generator is operated at part-load for a maximum amount of time, the average efficiency is significantly lower than the generators in the hydraulic and mechanical concepts. Because the concepts are based on niche technologies, which are not yet widely developed, the efficiency values used are on the conservative side of the claims made by the technology developers and that reported in the literature. On the other hand, the efficiencies of matured components, like the gearbox, the power converters and the ultracapacitor, are from the optimistic side of the claims.

Table 3.1: Average efficiencies of the drivetrain components used in the analysis

Electrical	η	**Hydraulic**	η	**Mechanical**	η
Gearbox	0.98	Gearbox	0.98	Gearbox	0.98
Generator	0.80	Generator	0.95	Generator	0.95
AC/DC converter	0.95	Pump/Motor 1	0.92	RVT	0.90
DC/AC converter	0.95	Pump/Motor 2	0.92	VT	0.98
Ultracapacitor	0.97	Accumulator	0.88	Flywheel	0.90

Figure 3.7 shows the difference between the mechanical cycle average power at the winch and the electrical cycle average power at the grid using the three drivetrain concepts. The mechanical power reaches its maximum at $20\,\mathrm{m\,s^{-1}}$. This is the rated wind speed, which stems from a design decision for this particular case study. Figure 3.8 shows the net efficiencies of the three concepts with respect to the wind speed. One of the key performance indicators (KPI) used to compare the net efficiencies of the systems is the capacity factor. A representative wind speed distribution is used for this comparison. The wind speed data is obtained from the ERA5 reanalysis dataset for an offshore location in the German North Sea. The mean wind speed at the location is $11\,\mathrm{m\,s^{-1}}$, the Weibull scale parameter is $12\,\mathrm{m\,s^{-1}}$ and the shape parameter is 2.3. The capacity factor for all three concepts turned out to be 0.47. The electrical power output for all three drivetrains is almost equal to the mean wind speed for the chosen data.

The drivetrain concepts have a high number of components with niche technologies developed by different companies. For this reason, the efficiency values are uncertain. An uncertainty analysis showed that, with a change in the efficiencies of the individual components within a band of 5%, the net efficiencies of the drivetrain concepts vary in the same order. Moreover, the capacity factor for all three concepts remains the same.

In fig. 3.9, the left axis shows the volume of energy stored and discharged in the electrical concept, and the right axis shows the maximum mechanical power peaks during one full cycle in the operational wind speed range. It can be seen that the energy exchanged through the intermediate storage increases with increasing wind

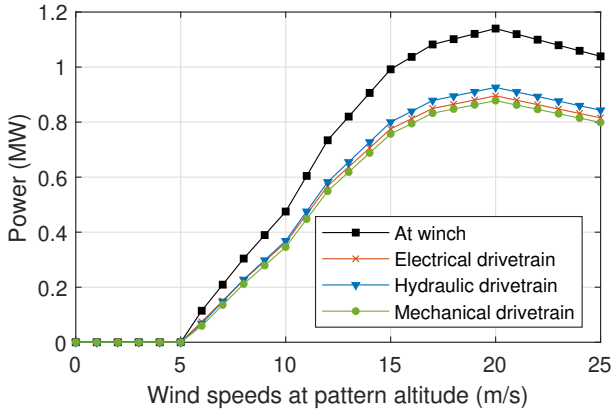

Figure 3.7: Computed power curves using the three drivetrain concepts

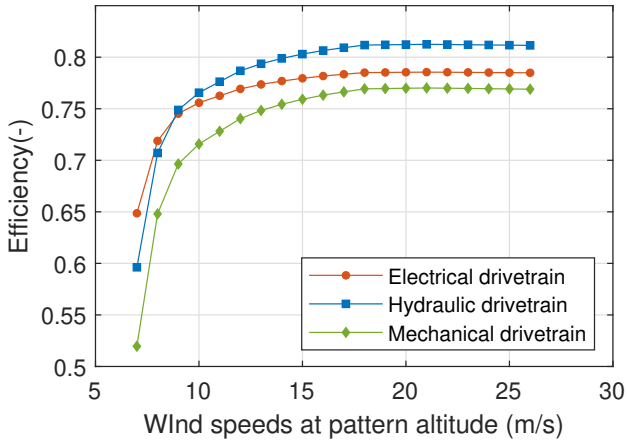

Figure 3.8: Net efficiency of drivetrain concepts with respect to wind speed

speed until its maximum at rated wind speed. As a result, the intermediate storage for power smoothing is utilized more at higher wind speeds. This indicates that the storage would be sized for the rated wind speed. Table 3.2 shows the resulting component sizes for all three drivetrain concepts. The storage components get sized for the rated wind speed, which is $20\,\mathrm{m\,s^{-1}}$. The generator in the electrical concept, the first pump/motor machine in the hydraulic concept and the RVT in the mechanical concept get sized for maximum peak power reached in the cycle operation at the rated wind speed which is 2.46 MW.

This simulated performance data of the AWE system was not based on designing the system for a particular wind class. But when doing so, the rated wind speed is selected with respect to the mean wind speed of the wind class. Designing a

Table 3.2: Component sizes of the three drivetrain concepts

Electrical	Size	Hydraulic	Size	Mechanical	Size	Units
Gearbox	2.46	Gearbox	2.46	Gearbox	2.46	MW
Generator	2.46	Generator	0.95	Generator	0.88	MW
AC/DC	2.46	Pump/Motor 1	2.46	RVT	2.46	MW
DC/AC	0.90	Pump/Motor 2	0.95	VT	1.58	MW
Ultracap.	14.6	Accumulators	15.3	Flywheel	14.75	MWs

system for higher wind speeds will increase the rated power capacity of the system but might also lead to oversizing the drivetrain components. If such a system were to be installed in a location such as the one mentioned earlier, the system would be underutilized for a large amount of time. Figure 3.10 shows KPIs like the levelized cost of energy (LCoE), the capacity factor (cf) and the annual energy production (AEP) for the electrical concept, resulting if the AWE system is capped at lower wind speeds. The LCoE flattens out at $15\,\mathrm{m\,s^{-1}}$. This allows for other trade-offs for the same LCoE. For example, a lower-rated wind speed choice leads to a higher capacity factor, whereas a higher-rated wind speed choice leads to a higher AEP.

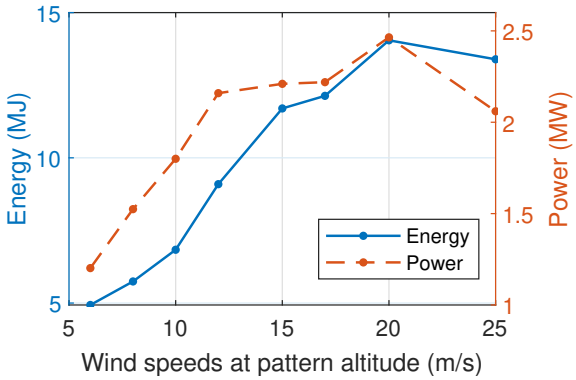

Figure 3.9: Energy exchanged (electrical concept) and the maximum power peaks during one full cycle

Figure 3.11 shows the normalized capital cost breakdown of the complete AWE system using the three drivetrain concepts. Values are normalized because the absolute numbers are not necessary for the relative comparison but also to protect the commercial interests of the companies involved. The cost component 'AWES' includes the cost of the kite, the tether, the winch and the launch and land apparatus. It is the largest cost component, with a share of around 65% for all three concepts. Similar to the efficiency comparison, the capital costs of all three drivetrain concepts are of the same order. The uncertainty for costs is higher than the uncertainty for efficiencies since a lot more factors are involved, like company-specific technologies,

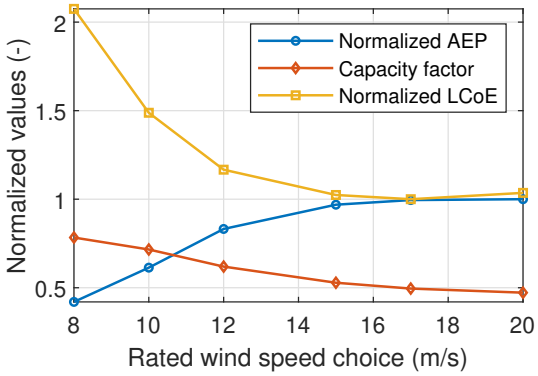

Figure 3.10: AEP, capacity factor (cf), and LCoE using the electrical concept if the system is redesigned for different rated wind speeds

economies of scale and supply chain, to name only a few. It shows that the drivetrain costs are a significant (around 35%) share of the total system costs and, hence, cannot be neglected in the design decisions of the commercial AWE systems. The components sized for the maximum mechanical peak power are the primary cost drivers. They are the generator in the electrical concept, the first pump/motor machine in the hydraulic concept, and the RVT in the mechanical concept. The storage components in all the concepts approximately have the same share.

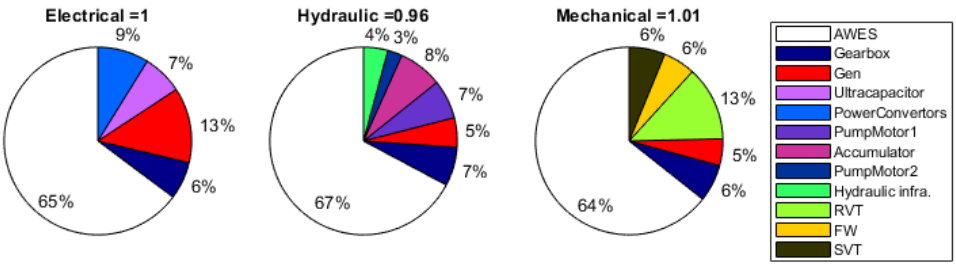

Figure 3.11: Capital cost breakdown

The performance and cost comparison shows that all three drivetrain concepts are essentially comparable to each other. In addition to these performance criteria, a qualitative comparison is also essential to support decision-making. Table 3.3 compares the three storage technologies. For facility weight and volume, the mechanical concept would be the most compact, followed by the electrical and the hydraulic. Though the self-discharge rates of these technologies are quite high, the storage would only be used actively for power smoothing and not for storing energy for longer durations, as in conventional energy storage applications.

During the charge-discharge cycles, the accumulators need to maintain the

Table 3.3: Comparison of attributes of the three storage technologies

	Supercapacitors	**Hydro-pneumatic accumulators**	**Flywheel**
Specific energy (Wh/kg)	3 – 50	~ 0.5	5 – 150
Energy density (kWh/m^3)	10 – 30	~ 1.5	20 – 80
Specific power (W/kg)	500 – 5000	~ 3000	1000 – 30000
Power density (kW/m^3)	1000 – 5000	~ 7500	800 – 5000
Self-discharge rate (%/day)	20 – 40	50 – 95	50 – 100

required pressure levels, the ultracapacitors need to maintain the required voltage levels, and the flywheels need to maintain a certain lower limit on rotational speed to maximize their efficiencies and lifetimes. Therefore, all three solutions might need to be sufficiently oversized to maintain their respective limits on the depth of discharge. Accumulators and flywheels can employ a larger number of duty cycles than ultracapacitors. Mechanical components have relatively higher failure rates than hydraulic and electrical components. Therefore, flywheels might not be suitable for applications in remote areas where operation and maintenance are more expensive.

3.4. KEY-TAKEAWAYS

The share of the drivetrain costs in the total system costs is significant (around 35%). Since most of the AWE companies are now entering the commercialization phase, it is necessary for them to include drivetrains in their design process. To this end, it is essential to capture the effect of the drivetrain on the scaling and system sizing studies of AWE devices. A key aspect is understanding the relationship between the requirements on the drivetrain for power smoothing and system size. This will facilitate evaluating trade-offs between scaling to different system sizes that include optimizing the size in order to reduce the power peaks and, hence, drivetrain costs.

Table 3.4 summarizes the comparative assessment of the three drivetrain concepts proposed in this chapter. Individually, the technologies used in the three concepts have reached a technology readiness level (TRL) of '9', but none of them have been used in the configuration, size and operational requirement such as this. None of the drivetrain concepts could yet be designed with off-the-shelf components. Between the three concepts, the electrical concept is more mature, followed by the hydraulic and then the mechanical. Consequently, the electrical concept would be a safer choice for a first market entry since it is the most widely used and understood configuration in the power generation industry. The hydraulic and mechanical concepts still require some amount of development. These components must be developed in parallel to the AWE system in close collaboration to be commercially ready at the time of market entry. AWE is an innovative technology that has development costs and risks. Using relatively unproven technologies like the hydraulic or the mechanical drivetrain will increase risks and the overall

development costs.

Table 3.4: Qualitative comparison of drivetrain concepts (where, '≃' indicates relatively comparable, '↑' indicates relatively advantageous and '↓' indicates relatively disadvantageous)

Criteria	**Electrical**	**Hydraulic**	**Mechanical**
Performance (eff. & cost)	≃	≃	≃
Lifetime	↓	↑	↑
Facility size & weight	↑	↓	↑
Reliability	↑	↑	↓
Commercial readiness	↑	↓	↓

One of the key findings of this work is that the three concepts are comparable in terms of net efficiency and capital cost. Due to the linearity of the cost models, this should also hold, to first order, for different sizes of the proposed concepts. Nevertheless, this finding cannot be generalized across different AWE concepts and designs. Different concepts will produce different operational dynamics. The sizing and costing of the drivetrain components are highly dependent on the operational characteristics of the AWE system but also on efficiency assumptions and reference cost data. Note also that the performance simulation data of the AWE system used in the present case study is not an optimized dataset. For the analyzed AWE system, the difference between the peaks and the net cycle average increased with increasing wind speeds. This difference will differ based on the type of the AWE concept and its size.

A major drawback of the electrical drivetrain is under-utilization of the generator. If a particular AWE system were to produce lower power peaks, then the electrical drivetrain would further gain attractiveness as a design choice due to its relative maturity. On the one hand, the hydraulic and mechanical systems benefit from the generator being sized for rated power, but on the other, the hydraulic pump/motor machine and the RVT need to be sized for peak power. Kite inertia is a crucial aspect influencing power fluctuations. With the current trend to up-scaling the size and rating of AWE systems, the difference between peak and rated power might further increase and, consequently, exacerbate the under-utilization of components. With further development and adoption, the hydraulic pump/motor and the RVT could scale better in terms of cost than the generator because of their relatively simpler construction. In such cases, the electrical system becomes less economical and a hydraulic or mechanical concept could gain the edge – even considering the higher risks.

4

COST MODELLING AND ECONOMIC METRICS

Chapter 2 described the developed power curve model for fixed-wing ground-generation airborne wind energy (AWE) systems, and Chapter 3 described the drivetrain concepts for power smoothing. This chapter presents the cost modelling of all the AWE components essential to compute the levelised cost of energy (LCoE) of AWE systems. The work described in this chapter was developed as part of the IEA Wind Task 48 activity and is the result of a collaborative effort between industry and academia. Airborne Wind Europe facilitated the setup of this work and acts as an intermediary for data collection, storage, and dissemination. This chapter provides parametric cost models that aim to estimate both capital expenditure (CapEx) and operational expenditure (OpEx) associated with each component of AWE systems. Furthermore, the report identifies relevant design metrics that could be used as objectives for the optimisation and refinement of AWE system designs. These metrics will not only aid in evaluating the performance and efficiency of AWE systems but will also guide future research and development efforts.

The outline of this chapter is as follows. Section 4.2 describes the developed models to estimate kite, tether and ground station costs and Section 4.3 describes the economic metrics.

This chapter has been adapted from the following technical report and the peer-reviewed article:

[91] R. Joshi and F. Trevisi. Reference economic model for airborne wind energy systems. Technical report. IEA Wind TCP Task 48, 2024. DOI: 10.5281/zenodo.10959930.

[62] R. Joshi, M. Kruijff, and R. Schmehl. "Value-Driven System Design of Utility-Scale Airborne Wind Energy". In: Energies 16 (4 Feb. 2023), p. 2075. ISSN: 1996-1073. DOI: 10.3390/en16042075.

4.1. Introduction

The objective of this chapter is cost modelling and the definition of design metrics that could be used as objectives for designing airborne wind energy (AWE) systems. These aspects are necessary to understand the economic potential of AWE and are crucial when designing a system for a given application. A reference economic model is useful both for industry and for academia. Industry can use it to assess the economic viability of their specific implementation while ensuring the economic properties are aligned with the respective information of competitors. Academics can use it to assess the economic aspects of their research while ensuring that this information is derived from up-to-date industry data.

The cost model and the economic metrics described in this chapter are also published as an open-source code repository [109].

4.2. Cost modelling

The cost model used in the present work is described in [91]. This model was developed as a collaborative effort between industry and academia as a part of the IEA Wind TCP Task 48 [110]. This task aims to build a strong collaboration to accelerate the development and commercialisation of AWE technology. This work falls under Work Package 1, which focuses a.o. on identifying economic drivers and the potential of deploying AWE in different markets. Building, refining, and validating this economic model must be a collaborative effort between academia and industry to ensure high quality.

4.2.1. Methodology

The process of developing this reference economic model is shown in fig. 4.1. A workshop was conducted as an IEA Wind Task 48 activity in June 2023 for the introduction and call for collaboration on this work. The workshop was attended by the AWE industry and academic institutions. Around 17 participants expressed interest, and of those, 10 participants were able to provide significant inputs within the planned timeframe. The portfolio of participants who provided input includes AWE companies, tether and ground station manufacturers, suppliers, and university research groups.

The initial formulation of cost functions was based on the dependency on key design parameters such as kite wing area, span, aspect ratio, tether properties, generator characteristics, etc. This was described in the *version 0* of this report. This initial version was then provided to participants along with individual spreadsheets to collect their feedback and inputs. These data have been used to update the cost functions and produce the present (**version 1**) of the report. The cost model is implemented as a modular code in MATLAB. This updated report [91] and the code [109] are published open source, and the individual spreadsheets are archived with Airborne Wind Europe to preserve anonymity. Airborne Wind Europe was an intermediary that hosted the data collection, storage, and dissemination.

In addition to the input of the workshop participants, publicly available reports and articles were also used to collect cost references. Table 4.1 lists the relevant

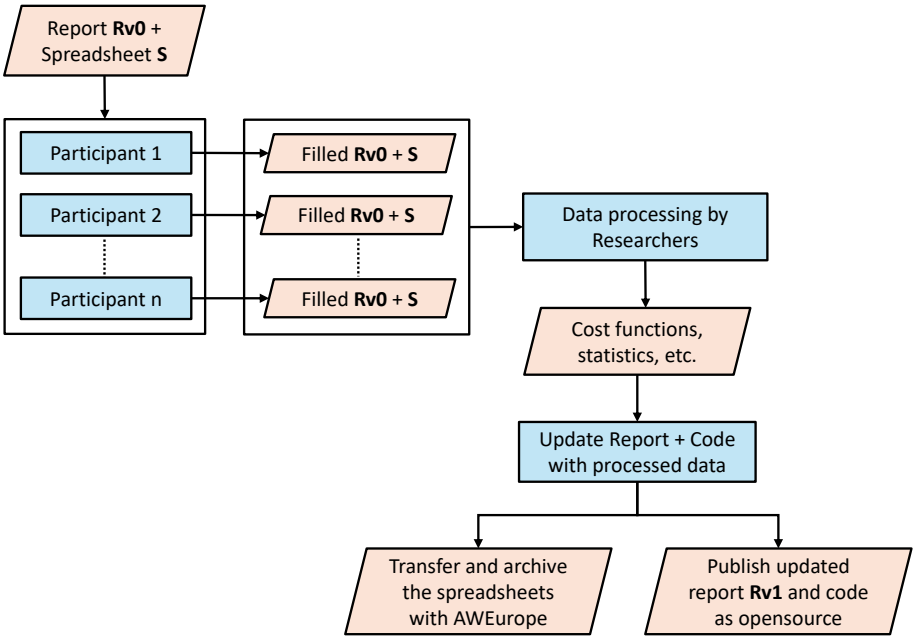

Figure 4.1: Flowchart showing the adopted process to build the reference economic model for AWE systems. Here, 'Rv0' corresponds to the *version 0* of the report and 'S' corresponds to the individual spreadsheets provided to the participants.

literature available on the cost modelling of AWE systems and horizontal axis wind turbines (HAWTs) used in this work.

By their nature, cost models are highly uncertain because they are subject to nonscientific, nontechnical, site-dependent, and sometimes political considerations. Therefore, many assumptions must be considered in the derivation, especially at the current early stage of technology development. The cost references provided in this report are based on the early commercialization of AWESs with the system sizes ranging from 100 kW-2 MW and series production volumes of 50+ units. Moreover, we do not consider any overhead costs in development, manufacturing and profit margins, which might be significant for certain low TRL (technology readiness level) and CRL (commercial readiness level) components.

The following sections detail the modelling of the subsystem cost contributions. For every component and subcomponent of the AWE system, as shown in Figure 4.2, the total costs are divided into capital expenditure (CapEx) and operational expenditure (OpEx). Figure 4.3 shows the used classification of components and subcomponents applied to an existing system from [121].

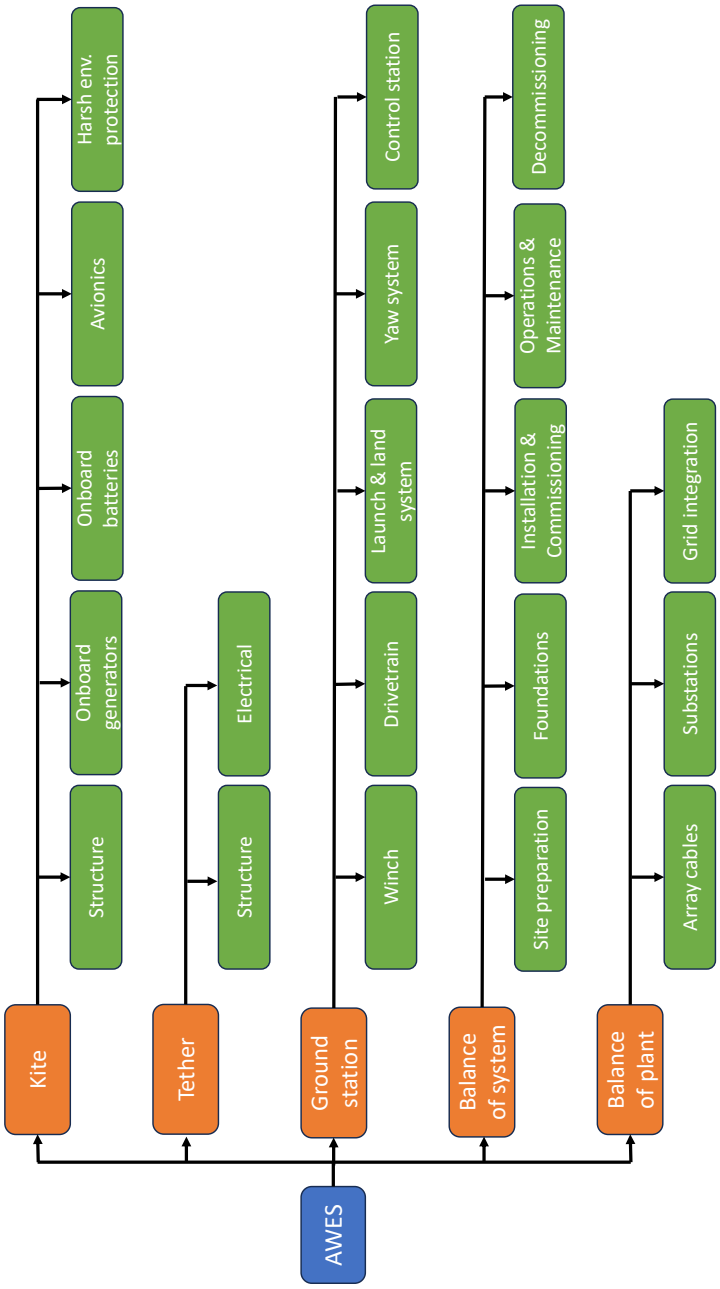

Figure 4.2: Breakdown of cost components of an airborne wind energy system used in this report. The system is represented in 'blue', the components in 'orange', and the subcomponents in 'green'.

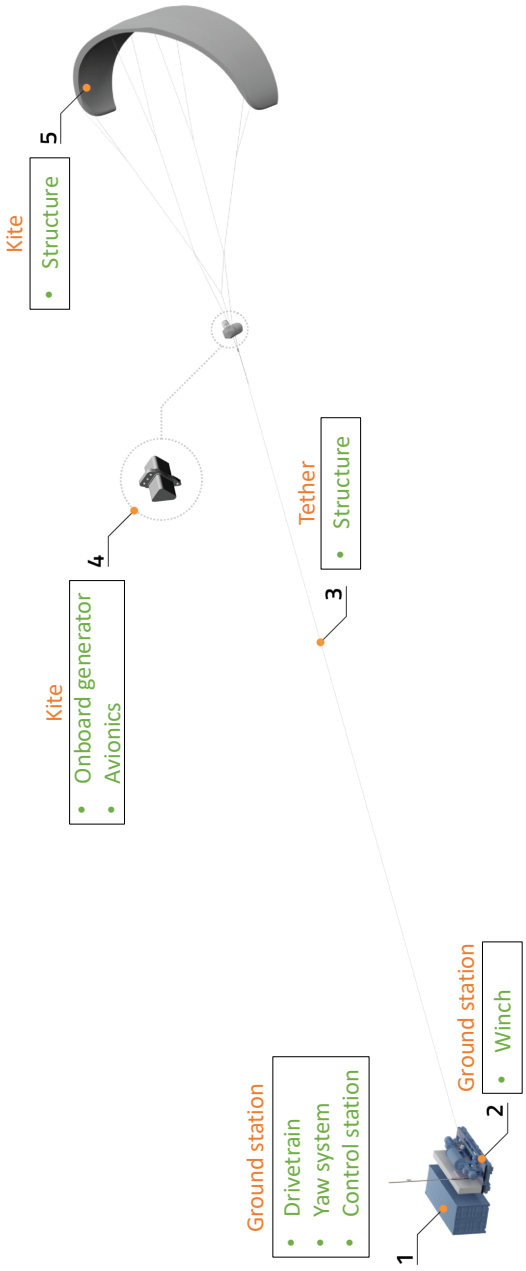

Figure 4.3: Subcomponents classification used in the report as applied to an existing system. Image from [121]. Note that not all subcomponents are necessarily a part of every system.

Table 4.1: Referenced publicly available literature for cost modelling.

Year	Author(s)	Focus	Source
2013	J. Heilmann, C. Houle	GG soft-wing	[52]
2014	C. Grete	GG soft-wing	[48]
2016	M. De Lellis et al.	GG soft-wing	[111]
2018	P. Faggiani, R. Schmehl	GG soft-wing	[112]
2018	F. Bauer et al.	FG fixed-wing	[113]
2019	BVG Associates	HAWTs	[114]
2019	NREL	HAWTs	[115]
2019	M. Garcia-Sanz	HAWTs and AWE systems	[116]
2020	N. Tucker	FG fixed-wing	[117]
2020	F. Trevisi et al.	GG & FG fixed-wing	[118]
2021	NREL	HAWTs	[119]
2022	BVG Associates	GG & FG	[57]
2022	NREL	PV & Storage	[120]

4.2.2. KITE

The flying subcomponents are responsible for converting the wind power into mechanical power, and thus, their cost models play a central role in the system costs. Currently, many different kite concepts are being explored within the domain, which makes the development of a comprehensive cost model challenging. Different kite concepts lead to different technical implementations and, thus, costs. In this chapter, the most researched concepts in AWE, which are GG systems based on soft and fixed wings and FG systems based on fixed wings, are modelled. This first version does not address the cost modelling of the flying components of less common concepts, e.g., Rotational, Magnus effect, etc.

STRUCTURE (FIXED-WING)

The kite costs are divided into structure costs $C_{k,str}$ and avionics costs $C_{k,avio}$. The kite structure costs are dependent on the kite mass and wing area. The dependence on the mass is due to the cost of the composite material, adhesive, and production. The dependence on the wing area is due to the costs of surface treatment, coating, etc. In this case, the material is a carbon-fibre composite and the costs are modelled as

$$C_{k,str} = p_{str} m_k + p_S S, \tag{4.1}$$

where m_k is the kite mass from eq. (2.20) and S is the wing area. For a better estimate, this cost function should include the total surface area of the kite, which includes the wing, fuselage, tail surfaces, and any other parts that are exposed to airflow during flight. p_{str} is 250 €kg^{-1} and p_S is 200 €m^{-2}. Structural costs are expected to drop with the development of technology and with improved structural designs, but such future projections are not considered in the present work.

STRUCTURE (SOFT-WING)

Soft kites, also known as soft wings, have flexible structures made of lightweight materials such as nylon, polyester (Dacron) or polyethylene (Dyneema) fabric. This flexibility allows them to be easily manoeuvred and controlled in the air. The structure costs include the costs of the fabric (including reinforcements) and the bridle lines.

The flat wing area A can be estimated from the projected area S with $A = (25/18)S$. The aspect ratio is assumed to not influence the wing cost and the influence of the wing design and type on the cost is neglected. The total costs are estimated to be a function of the wing area as

$$C_{\text{str}} = (p_{\text{fabric}} + p_{\text{bridle}})A, \tag{4.2}$$

where $p_{\text{fabric}} = 45$ € m^{-2} and $p_{\text{bridle}} = 8$ € m^{-2}. It is important to note that the structure costs will not only be proportional to the area but also to the amount of tether force it has to withstand, such as eq. (2.20), but this dependency is not modelled due to a lack of data.

Compared to fixed-wing kites, the lifetime of the soft-wing kites is necessary information to estimate the replacement costs. If a better-engineered estimate of the kite lifetime is not available, it can be assumed to be of $L_{\text{str,soft}} = 5000$ flying hours at full loading (i.e., maximum tether force), which corresponds to $L_{\text{str,soft}} = 0.57$ flying years.

To estimate how much of the kite lifetime has been used, one can find the equivalent used lifetime knowing the wind distribution $f(v_{\text{w}})$ (e.g. Weibull) and the tether force, which approximates the loading on the kite, as a function of wind speed $F_{\text{t}}(v_{\text{w}})$. To find the equivalent used lifetime, we define the Loading Factor LF as

$$LF = \int_{v_{\text{in}}}^{v_{\text{out}}} f(v_{\text{w}}) \frac{F_{\text{t}}(v_{\text{w}})}{F_{\text{t,max}}} \mathrm{d}v_{\text{w}}, \tag{4.3}$$

where v_{in} and v_{out} are the cut-in and the cut-out wind speed respectively. The frequency of replacements per year is then $f_{\text{repl,str}} = \frac{LF}{L_{\text{str,soft}}}$.

ONBOARD GENERATORS

FG systems use the onboard generators for take-off, power generation, and land, which then represents a significant cost. Instead, GG AWESs typically generate a small amount of power onboard, which is needed to power the onboard avionics. Except for soft-wing systems, the GG systems typically use these generators as motors for take-off and land. They can also be used during the power generation phase to enhance control authority.

The onboard generator cost can be expressed as a function of their rated power as

$$C_{\text{ob,gen}} = p_{\text{ob,gen}} P_{\text{rated,ob,gen}}, \tag{4.4}$$

where $p_{\text{ob,gen}} = 120$ € kW^{-1} and $P_{\text{rated,ob,gen}}$ is in kW.

Onboard batteries

The onboard batteries are used to supply power to the avionics and the onboard generators when needed. The sizing of these batteries depends on the amount of energy required by the onboard systems.

The cost of the batteries is estimated to be proportional to the batteries' capacity. The costs are $p_{\text{ob,batt}} = 150\ €\,\text{kW}^{-1}\,\text{h}^{-1}$.

Avionics

The avionics costs do not scale with the size of the kite and, hence, can be considered fixed. They typically include all the electronic systems used on the kite, such as communication and navigation hardware, sensors, CPUs, and any electronic system needed to perform individual functions. Usually, these have a high share in costs due to the requirements for aviation-grade certification and redundancies.

For prototypes, the avionics cost is estimated to be $C_{\text{k,avio}} = 15$ k€. For early series production, the aviation certification and the redundancy requirements are expected to raise the cost of soft-wing kite systems to $C_{\text{k,avio}} = 30$ k€ and of fixed-wing kite systems to $C_{\text{k,avio}} = 150$ k€. Recent developments indicate that the AWE systems can be regarded as drones instead of aircraft, which would significantly reduce the overall avionics costs due to the relaxation of redundancy requirements for drones.

Other

The kite will have other cost components, such as the tether attachment mechanism and protection equipment necessary in extreme events or to ensure longer life, such as lightning protection, de-icing, erosion protection, etc. It will also have some other maintenance costs over the lifetime, but these are not modelled due to a lack of information.

4.2.3. Tether

The tether is a structural component which has to withstand the pulling force of the kite. The price in $€\text{kg}^{-1}$ depends on the type of material and the suppliers. The tether fibre commonly used in the AWE industry is the Dyneema fibre [71]. Multiple strands are usually braided together to manufacture the tether, and hence, the tethers have a hollow inner core. The nominal diameter is the measured diameter of a newly manufactured tether. After experiencing some loading, this diameter becomes smaller and is called the worked-in diameter. This is supposed to be used in performance evaluations. A hollow core of 15% of the cross-sectional area can be assumed, such that the stress acting on the tether

$$\sigma_{\text{t}} = \frac{F_{\text{t}}}{f_{\text{At}} \pi \frac{d_{\text{t}}^2}{4}}, \tag{4.5}$$

where $F_{\text{t}} = W_{\text{l}} S$ in N, $f_{\text{At}} = 0.85$, which is the ratio between the cross-sectional area taken by the fibres and the tether cross-sectional area, and d_{t} is the worked-in tether diameter. Different wear-resistant coatings are usually applied on the tether, which

increases its total mass. This is usually around 10% of the total mass. The tether CapEx can be computed as

$$C_t = p_t m_t, \tag{4.6}$$

where p_t is 80 €kg^{-1} and m_t is determined from eq. (2.25).

For FG systems, the tether comprises a structural and an electrical part. The electric conductors are assumed to have a negligible material price compared to the structural part, but the dedicated manufacturing largely influences the tether cost. The cost of such a tether can be modelled by applying a manufacturing factor $f_{m,t}$= 2.5 to the tether cost estimated for GG systems.

Bending fatigue and creep were highlighted as the leading causes of tether failure in [71]. The bending fatigue is mainly relevant for GG systems since it arises when the tether is unwound from the drum at high tension. The bending failure is estimated using the method described in [71]. The number of cycles to failure N_b is a function of the ratio between the drum diameter d_{drum} and the tether diameter d_t, and the tether stress. It is given as

$$N_b = 10^{(a_1 - a_2\sigma_t)}, \quad \text{for} \quad 0.2 < \sigma_t < 0.8\,\text{GPa}, \tag{4.7}$$

where σ_t is in GPa and the values of a_1 and a_2 are dependent on d_{drum}/d_t and are given in table 4.2. The number of cycles to failure with respect to the stress levels for the given d_{drum}/d_t ratios is shown in fig. 4.4.

Table 4.2: Parameter a_1 as a function of the drum to tether diameter ratio d_{drum}/d_t and constant parameter a_2.

$\mathbf{d_{drum}/d_t}$	10	20	30	100
$\mathbf{a_1}$	5.4	5.8	6.1	6.5
$\mathbf{a_2}$		2.6		

Miner's rule is commonly used in fatigue life analysis. It is based on the assumption that damage accumulates linearly with each load cycle. This means that the total damage caused by different stress cycles can be summed up to predict when the material will fail. Using the Miner's rule, for a given wind distribution $f(v_{w,ref})$, a tether failure will occur when

$$L_{t,bend} 8760 N_{bends} \int_{v_{w,cut-in}}^{v_{w,cut-out}} \frac{f(v_{w,ref})}{t_{cycle}(v_{w,ref}) N_b(v_{w,ref})} \mathrm{d}v_{w,ref} = 1, \tag{4.8}$$

where $L_{t,bend}$ is the tether lifetime, N_{bends} is the number of times the tether bends per cycle. There is at least one pulley in addition to the drum, which guides the tether during winding, and hence, we assume $N_{bends} = 2$. $v_{w,cut-in}$ and $v_{w,cut-out}$ are the cut-in and cut-out wind speeds respectively and t_{cycle} is in h.

Failure due to creep is more relevant for FG systems than failure due to bending. The creep curve shown in fig. 4.5 represents the tether life $L(\sigma_t(v_w))$ in logarithmic

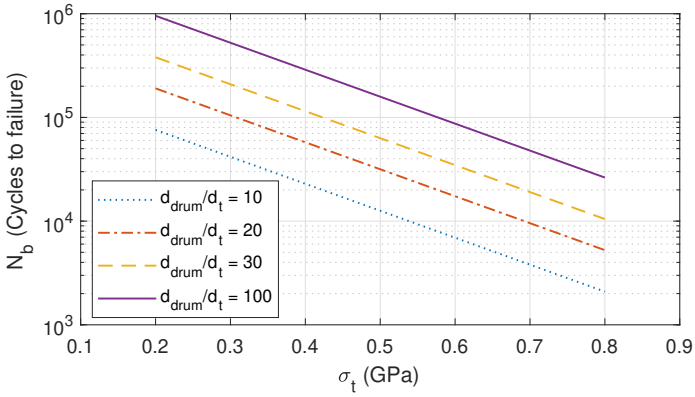

Figure 4.4: Relation between the number of cycles to failure and tether stress for different $d_{\text{drum}}/d_{\text{t}}$ ratios.

scale if only a given stress level $\sigma_{\text{t}}(v_{\text{w}})$ was applied. A polynomial approximation in the linear scale of the tether life curve for the highest-performing rope DM20 is

$$L(\sigma_t) = 10\hat{}\left(-2.4\sigma_{\text{t}}^3 + 8.3\sigma_{\text{t}}^2 - 11.2\sigma_{\text{t}} + 5.2\right), \tag{4.9}$$

where σ_{t} is in GPa.

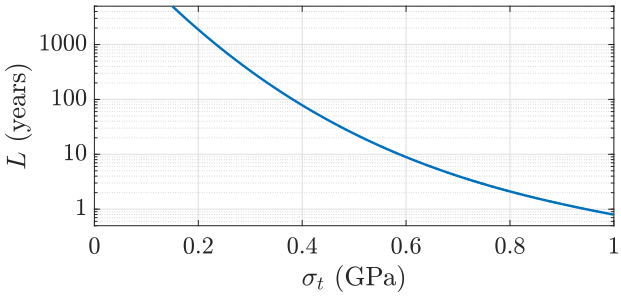

Figure 4.5: Caption

Given a wind distribution $f(v_{\text{w}})$, a tether failure occurs when

$$L_{\text{t,creep}} \int_{v_{\text{in}}}^{v_{\text{out}}} \frac{f(v_{\text{w}})}{L(\sigma_{\text{t}}(v_{\text{w}}))} \mathrm{d}v_{\text{w}} = 1. \tag{4.10}$$

The frequency of tether replacement per year is $f_{\text{repl,t}} = \frac{1}{L_{\text{t,creep}}}$. Note that some correction factors could be applied to account for the low tension during the reel-in phase and for the change in temperature during the day and during the seasons [71].

The frequency of tether replacement per year can, therefore, be calculated as

$$f_{\text{t,repl}} = \frac{1}{L_{\text{t,bend}}}. \tag{4.11}$$

Thus, the tether OpEx per year due to replacements is

$$O_t = f_{t,repl} C_t. \tag{4.12}$$

4.2.4. DRUM

The drum converts the tractive power of the kite into shaft power in the drivetrain. Essentially, the drum is a hollow cylinder with a certain wall thickness. The costs for control and winding mechanisms, including pulleys, guide rails, etc, are not considered due to the unavailability of data. These costs will affect the absolute costs but might not scale significantly with size. Therefore, the cost of the drum is assumed to be proportional to its mass. The drum is typically made of aluminium or steel. Data on these materials are listed in Table 4.3. The drum mass can be computed using the tether diameter as the rolling pitch [52]. When the tether is wound around a drum, it wraps in a helical pattern due to the drum's diameter and the tether's thickness. When the drum rotates once, the tether advances along the drum by one tether diameter, and this distance is known as the rolling pitch. A safety margin of around 10% is generally used on the tether diameter to calculate the pitch. The drum also has some dead windings that are not used. Hence, a safety factor on the tether length must also be applied. The drum mass is computed as

$$m_{drum} = \frac{\pi \left[d_{drum}^2 - (d_{drum} - 2t_{drum})^2 \right]}{4} \frac{l_t f_{s,1}}{\pi d_{drum}} d_t f_{s,2} \rho_{mat}, \tag{4.13}$$

where d_{drum} is the external diameter of the drum, t_{drum} its wall thickness, d_t the tether diameter, $f_{s,1}$ is the safety factor on tether diameter, l_t the tether length, $f_{s,2}$ is the safety factor for tether length, and ρ_{mat} the material density. The first fraction represents the cross-sectional area, the second fraction represents the number of windings of the tether around the drum, and the third term represents how much axial space is needed for each winding multiplied by the tether material density. Considering the tether lifetime due to bending, the ratio d_{drum}/d_t is assumed to be 100, and both safety factors are assumed to be 1.1.

Table 4.3: Drum-related data for aluminium and steel materials.

Parameter	Unit	Aluminium	Steel
p	€kg^{-1}	10	7
ρ	kgm^{-3}	2700	7850
$\hat{\sigma}$	MPa	300	500

We propose a simple first-order engineering approach to design the drum thickness. The maximum tether force $F_{t,max} = \hat{\sigma}_t \pi d_t^2/4$, where $\hat{\sigma}_t = 1.5$ GPa is the tether fibre (Dyneema DM20) strength, assuming no hollow core in this section. We assume that the drum should withstand the same force, distributed over a rectangular area of width d_t and height t_{drum}, i.e. $F_{t,max} = \hat{\sigma}_{mat} d_t t_{drum}$, where $\hat{\sigma}_{mat}$ is the tensile strength of the drum material. Therefore, the drum thickness can be

correlated to the tether diameter as

$$t_{\text{drum}} = \frac{\pi \hat{\sigma}_{\text{t}}}{4\hat{\sigma}_{\text{mat}}} d_{\text{t}}. \tag{4.14}$$

This simplified method neglects the effects such as the force distribution over the entire drum, stress concentrations, and dynamic loading. We used an additional safety factor of 2 on the estimated thickness of the drum to account for the neglected effects. For a steel drum, the CapEx is computed as

$$C_{\text{drum}} = p_{\text{st}} m_{\text{drum}}, \tag{4.15}$$

where m_{drum} is computed using eqs. (4.13) and (4.14).

4.2.5. ELECTRICAL DRIVETRAIN

The drivetrain is fundamentally different for FG and GG systems since, for FG systems, the generator is onboard, and for GG systems, it is on the ground. Based on the commercial readiness and proven track record of comprising components, the more suitable drivetrain for market entry is expected to be the electrical drivetrain, as shown in Figure 4.6.

In this drivetrain, the generator is directly connected to the drum with or without a gearbox. During cycle operation throughout the windspeed range, the rotational speed and torque of the drum vary within a wide range. Hence, a gearbox is generally necessary to convert the rotational speed and torque values to the generator's operational range. A gearbox could be avoided if the generator is custom-designed according to the operation of the AWE system. The generator is connected to an electrical storage and the grid via power converters. The storage solution has to be charged and discharged during the cycle to maintain smooth power output at the grid side. FG systems have the generators onboard, but they would still require intermediate storage on the ground for power smoothing.

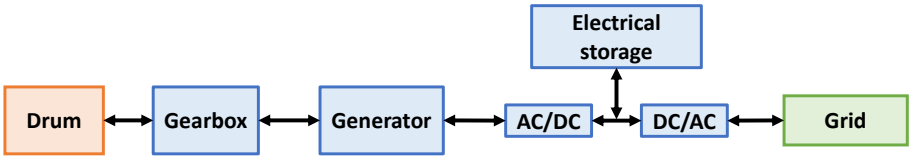

Figure 4.6: Electrical drivetrain architecture (adapted from [87]).

The following sections detail the individual cost models of the electrical drivetrain.

GEARBOX

Since the gearbox connects the drum to the generator, it has to be sized for the peak mechanical loading during the reel-out phase. The cost and size of the gearbox are not only driven by the transferred shaft power but also by the transferred torque.

The benefit of using a gearbox is that it reduces generator costs by controlling the input speed and torque of the generator. Scaling the gearbox costs with transferred power and torque together will give better estimates, but we model the costs only with power due to limited data availability. The costs are modelled as

$$C_{\text{gb}} = p_{\text{gb}} f_{\text{crest}} P_{\text{rated}}, \tag{4.16}$$

where p_{gb}=70 €/kW.

GENERATOR

The cost of the generator depends on the torque as well as on speed. High torque requires more robust components within the generator, whereas high speed requires high precision, wear resistance, etc. Due to the unavailability of detailed data, we represent the costs as a linear function of the rated power, given as

$$C_{\text{gen}} = p_{\text{gen}} f_{\text{crest}} P_{\text{rated}}, \tag{4.17}$$

where p_{gen} = 120 €/kW.

ELECTRICAL ENERGY STORAGE

The objective of energy storage is to act as an intermediate energy exchanger to charge and discharge during cycle operation to maintain the average cycle power at the grid side. The amount of storage required will be driven by the energy exchange required for this purpose [87]. Typical implementations of electrical storage technologies are an ultracapacitor bank or a battery bank. Both have different requirements for sizing as well as different cost and lifetime specifications. While ultracapacitors can withstand high C-rates (charge-discharge rates) of 100C or more, batteries typically have a low C-rate of around 0.5-1C. This drives the sizing of the two options. A 1C rate means the discharge current will discharge the entire battery in 1 hour.

In the present work, we choose ultracapacitors as the electrical energy storage component. An ultracapacitor bank is a high-capacity energy storage system composed of multiple ultracapacitor modules connected in parallel or series. Unlike traditional batteries, ultracapacitors store energy electrostatically, enabling rapid charge and discharge cycles with high efficiency. They are commonly used in applications requiring burst power delivery, energy recuperation, fast charging capabilities, and tolerance to frequent cycling. The costs are modelled as

$$C_{\text{uc}} = p_{\text{uc}} E_{\text{rated,uc}}. \tag{4.18}$$

where p_{uc} = 60 k€/kWh and $E_{\text{rated,uc}}$ is the required storage sizing in kWh. This is driven by the maximum energy the ultracapacitor bank exchanges during the cycle operations for all wind speeds.

As an example, fig. 4.7 shows the simulated instantaneous and average cycle power of a system with an electrical rated power of 150 kW at its rated wind speed. P_{m} and P_{e} are the instantaneous mechanical and electrical power, respectively. $P_{\text{m,avg}}$

and $P_{e,avg}$ are the cycle-average mechanical and electrical power, respectively. $P_{m,avg}$ is a hypothetical cycle average power computed by excluding all the drivetrain efficiencies to estimate the intermediate storage requirement.

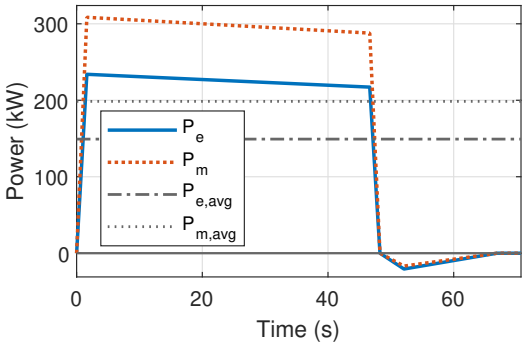

Figure 4.7: Instantaneous mechanical and electrical power over a representative pumping cycle and corresponding average cycle power.

The amount of energy exchanged through the storage during each cycle can be estimated as

$$E_{sto} = (P_m - P_{m,avg})\, t_o = (P_{m,avg} + P_{m,i,avg})\, t_i, \tag{4.19}$$

where t_o and t_i are the reel-out and reel-in times at respective wind speeds in the entire operation range. The capacity of the ultracapacitor bank is the maximum amount of energy stored in the entire operational range and can be computed as

$$E_{rated,uc} = \max(E_{sto}). \tag{4.20}$$

The ultracapacitors' lifetime depends on the number of charge-discharge cycles for the specific AWE system based on its operational behaviour. The number of charge-discharge cycles in a year is computed as

$$N_{cycles,uc} = \frac{8760}{E_{rated,uc}} \int_{v_{w,cut-in}}^{v_{w,cut-out}} f(v_{w,ref}) \frac{E_{sto}(v_{w,ref})}{t_{cycle}(v_{w,ref})} \mathrm{d}v_{w,ref}. \tag{4.21}$$

Therefore, the frequency of replacement per year of the ultracapacitor bank is computed as

$$f_{uc,repl} = \frac{N_{cycles,uc}}{N_{uc}}, \tag{4.22}$$

where N_{uc} is the indicated lifetime by the manufacturer. It is typically around 10^6 cycles. Thus the ultracapacitor OpEx per year due to replacements is

$$O_t = f_{uc,repl} C_{uc}. \tag{4.23}$$

POWER CONVERTERS

Power converters are electronic devices that convert electrical energy from one form to another, commonly alternating current (AC) to direct current (DC) or vice versa. They regulate the voltage, frequency, and waveform to match the requirements of various electrical systems, facilitating efficient energy transfer. The two power converters in this drivetrain will be sized differently. The converter connected to the generator will be sized according to the generator power rating, whereas the converter on the grid side will be sized according to the rated power of the AWE system. The cost of the power converters is modelled as

$$C_{\text{pc}} = p_{\text{pc}} P_{\text{rated}} (f_{\text{crest}} + 1), \tag{4.24}$$

where p_{pc} is 100 €/kW.

4.2.6. HYDRAULIC DRIVETRAIN

This drivetrain concept is more suitable for GG systems. Primary components of this concept are shown in fig. 4.8 and are described in [87, 122, 123]. The winch drives a pump-motor machine, which is connected to a hydropneumatic accumulator bank, and a hydraulic motor, which drives the generator. A hydro-pneumatic accumulator is a vessel capable of storing energy in the form of a compressed gas.

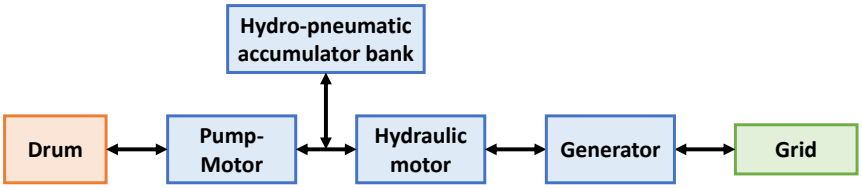

Figure 4.8: Hydraulic drivetrain architecture (adapted from [87]).

PUMP-MOTOR

Pump-motor machines refer to systems where a pump and a motor are combined into a single unit. This unit can either be driven as a pump using a mechanical input, such as the winch rotation or can be driven as a motor using a hydraulic input, such as from a hydropneumatic accumulator bank.

The CapEx of the pump-motor machine is modelled as

$$C_{\text{pm}} = p_{1,\text{pm}} P_{\text{rated,pm}}, \tag{4.25}$$

where $p_{1,\text{pm}} = 100$ € kW^{-1} and $P_{\text{rated,pm}}$ is the rated power of the machine which is driven by the peak mechanical power during reel-out.

Depending on operating conditions (e.g. effective capacity factor, wind speed variations), major maintenance of 2-4 times during the life is expected. This should typically decrease with product maturity.

$$OM_{\text{pm}} = f_{\text{om,pm}} p_{2,\text{pm}} P_{\text{rated,pm}}, \tag{4.26}$$

where $f_{\text{om,pm}} = 1/8$ year^{-1} and $p_{2,\text{pm}} = 75$ € kW^{-1}.

HYDROPNEUMATIC ACCUMULATOR BANK

The hydropneumatic accumulator has two chambers divided by a separator. The first chamber is a fluid chamber, usually filled with hydraulic oil, and the second is a gas chamber, usually containing nitrogen. The fluid chamber is connected to the hydraulic circuit. The winch drives the pump motor machine in the reel-out phase, which pumps the hydraulic fluid into the accumulator bank under high pressure. This accumulator bank is charged and discharged during the cycle to maintain smooth power output at the grid side.

The cost of the hydropneumatic accumulator bank can be modelled as

$$C_{\text{hacc}} = p_{1,\text{hacc}} E_{\text{rated,hacc}}, \tag{4.27}$$

where $p_{1,\text{hacc}} = 30{,}000$ € kW^{-1} h^{-1} and $E_{\text{rated,hacc}}$ is the required storage sizing in kWh. This is driven by maximum energy exchanged by the accumulator bank during the cycle operations for all the wind speeds in the operational range. The calculation of $E_{\text{rated,hacc}}$ is similar to $E_{\text{rated,uc}}$, as mentioned in the Ultracapacitor bank section

The maintenance cost of the hydropneumatic accumulator bank can be modelled as

$$OM_{\text{hacc}} = f_{\text{om,hacc}} p_{2,\text{hacc}} E_{\text{rated,hacc}}, \tag{4.28}$$

where $f_{\text{on,hacc}} = 1/10$ year^{-1} and $p_{2,\text{hacc}} = 1200$ € kW^{-1} h^{-1}.

HYDRAULIC MOTOR

Hydraulic motors are machines that convert hydraulic energy (the pressure and flow of hydraulic fluid) into mechanical energy (rotary motion). They are commonly used in hydraulic systems where the power source is a hydraulic pump. This unit is integrated with a controller and is used to drive the generator.

The CapEx of the hydraulic motor machine is modelled as

$$C_{\text{hm}} = p_{1,\text{hm}} P_{\text{rated,hm}}, \tag{4.29}$$

where $p_{1,\text{hm}} = 200$ € kW^{-1} and $P_{\text{rated,hm}}$ is driven by the rated power of the AWES.

The maintenance of the hydraulic motor machine is modelled as

$$OM_{\text{hm}} = f_{\text{om,hm}} p_{2,\text{hm}} P_{\text{rated,hm}}, \tag{4.30}$$

where $f_{\text{om,hm}} = 1/12$ year^{-1} and $p_{2,\text{hm}} = 80$ € kW^{-1}.

GENERATOR

The generator rating will be driven by the rated power of the AWES. The cost model is the same as described in Section 4.2.5.

The launch and land system (LLS) launches the kite and controls its descent for landing. The LLS will be different for different AWE concepts. There are two commonly used approaches: 1) Horizontal take-off and landing (HTOL), which

either uses a catapult or a rotating arm and 2) Vertical take-off and landing (VTOL), which uses electric propellers. On the one hand, HTOL has much larger spatial requirements than VTOL, which significantly drives up the cost of the supporting infrastructure, but on the other hand, VTOL significantly drives up the kite's structural mass and, consequently, the cost. VTOL is most certainly the preferred design choice for FG systems since they already have ram-air turbines which can be used as propellers. Due to the unavailability of data, the LLS costs, along with the yaw system and control station costs, are not modelled in the present work.

4.2.7. BALANCE OF SYSTEM COSTS

The balance of system (BoS) for a single AWE system is defined as all components except the primary system components, which are the kite, the tether, and the ground station. These costs are more relevant for the evaluations of specific business cases and will be highly dependent on the type and size of the system as well as on site-specific considerations. These considerations can cause order-of-magnitude changes in the results for different scenarios. The costs considered in the present work are under the assumption of an onshore installation. BoS costs consist of site preparation, foundation, installation, operation maintenance and decommissioning.

Costs under site preparation include removing obstacles such as vegetation, debris, and uneven terrain that could interfere with the kite's launch, flight, or landing. Additionally, any necessary groundwork, such as levelling the surface or installing protective barriers, may be undertaken to optimise the site for efficient and uninterrupted system operation. These costs are modelled as

$$C_{\text{sitePrep}} = p_{\text{sitePrep}} P_{\text{rated}}, \tag{4.31}$$

where $p_{\text{sitePrep}} = 40$ €kW^{-1}.

Foundations and support structures are designed to withstand the forces generated by the AWE system during operation and support the ground station weight. These foundations can vary in design depending on soil conditions, site location, and system requirements. The launch and land apparatus is also an important cost driver for this component. Moreover, these costs will be significantly different for onshore, offshore bottom-fixed and offshore floating scenarios. Since these costs would be driven by the peak power, they are modelled as

$$C_{\text{found}} = p_{\text{found}} f_{\text{crest}} P_{\text{rated}}, \tag{4.32}$$

where $p_{\text{found}} = 55$ €kW^{-1}.

Installation and commissioning involve assembling and configuring components to ensure proper functionality and performance. This process includes erecting support structures, connecting power and communication systems, and testing operational parameters. In addition, commissioning involves fine-tuning control algorithms, conducting safety checks, and verifying compliance with regulatory standards. These costs are modelled as

$$C_{\text{install}} = p_{\text{install}} P_{\text{rated}}, \tag{4.33}$$

where $p_{\text{install}} = 40$ €kW^{-1}. The operation and maintenance costs include all the yearly costs, for example, the lease of the land used and the insurance costs against potential risks and liabilities associated with their deployment and operation. These costs are modelled as

$$O_{\text{BoS}} = p_{\text{BoS,O}} P_{\text{rated}} \tag{4.34}$$

where $p_{\text{BoS,O}} = 60$ €kW^{-1}year^{-1}.

Decommissioning entails safely dismantling and removing components at the end of their operational lifespan or in case of system retirement. This process involves disassembling support structures, disconnecting power and communication systems, and responsibly disposing of materials in accordance with environmental regulations. These costs are modelled as

$$C_{\text{decomm}} = 0.5 C_{\text{install}}, \tag{4.35}$$

where C_{install} are the installation and commissioning costs from eq. (4.33).

Another type of cost is related to the balance of plant (BoP), which is defined as all components of an AWE farm (AWE flock), excluding the individual system costs. These costs will be relevant for evaluating specific business cases and layout design. BoP includes the array cables, substations and grid integration costs. These costs are not modelled in the present work due to the lack of information and the focus on system design.

4.3. ECONOMIC METRICS MODELLING

Economic metrics are quantitative measures used to evaluate the performance, efficiency, and effectiveness of a system or product during the design process. These metrics can be used as objectives in design optimisation frameworks.

4.3.1. LEVELISED COST OF ENERGY (LCOE)

The design objective is the goal that the developer wants to achieve with the system. The most common but also conflicting objectives are higher energy production and minimum costs. Levelised cost of energy (LCoE) is a holistic metric that combines both objectives into one metric and is defined as

$$\text{LCoE} = \frac{\sum_{\text{y}=0}^{N_{\text{y}}} \frac{\text{CapEx}_{\text{y}} + \text{OpEx}_{\text{y}}}{(1+r)^y}}{\sum_{\text{y}=0}^{N_{\text{y}}} \frac{\text{AEP}_{\text{y}}}{(1+r)^y}}, \tag{4.36}$$

where CapEx is the capital expenditure, OpEx is the operational expenditure, r is the discount rate, AEP is the annual energy produced, y is the instantaneous year, and N_{y} is the project lifetime.

The annual energy production (AEP) depends on the wind resource at the location and the power curve based on that location's vertical wind shear profile. AEP is calculated as

$$\text{AEP} = 8760 \int_{v_{\text{w,cut-in}}}^{v_{\text{w,cut-out}}} P_{\text{e,avg}}(v_{\text{w,ref}}) f(v_{\text{w,ref}}) \text{d}v_{\text{w,ref}}, \tag{4.37}$$

where $v_{w,ref}$ is the wind speed at the chosen reference height h_{ref}, $v_{w,cut-in}$ and $v_{w,cut-out}$ are the cut-in and cut-out wind speeds, respectively, and $f(v_{w,ref})$ is the probability of occurrence of wind speeds in a year. It is assumed that the wind characteristics remain constant over each year, such that the energy produced over the entire lifetime is calculated as

$$E_{lifetime} = \sum_{y=0}^{N_y} \frac{AEP_y}{(1+r)^y}, \tag{4.38}$$

where r is the discount rate, y is the instantaneous year, and N_y is the project lifetime in number of years.

The final discount rate is usually a result of the different discount rates for equity and debt components weighted according to their proportions in total financing. This is also known as the weighted average cost of capital (WACC). If a project is financed with a debt-to-equity ratio of 'q', then the WACC, or the final discount rate

$$r = \frac{q}{1+q} r_d (1 - T_C) + \frac{1}{1+q} r_e, \tag{4.39}$$

where r_d is the cost of debt, r_e is the cost of equity, T_C is the tax rate for corporations. Typical values for wind energy projects are $q = 70/30$, $r_d = 0.08$, $r_e = 0.12$, and $T_C = 0.25$.

4.3.2. VALUE-BASED METRICS

The revenue of wind farms has long been dependent on government subsidies. As renewable energy technologies are maturing and becoming cheaper, developers now require fewer subsidies to build and operate new wind farms [124]. Since introducing competitive auctions for renewable energy technologies, subsidy-free wind power has rapidly grown in the European market [125]. In a subsidy-free future, the revenue generated by wind farms will depend on the DAM. The functioning of a typical liberalised European electricity market is described in [126–128]. It is observed that the DAM prices drop when the amount of power generation through renewables in the grid increases, which is known as the merit order effect [129, 130]. Accordingly, an increase in the renewable electricity supply reduces the market value of renewable electricity producers, which is known as the self-cannibalisation effect. Along with developers, the market also suffers from increasing price fluctuations. Studies such as [131, 132] show how changing the wind turbine design can help counter this effect. Turbines designed for lower specific powers (ratio of generator size to rotor swept area) can produce more electricity at lower wind speeds leading to higher earnings than turbines designed for higher specific powers. Accordingly, the wind industry is slowly evolving beyond the conventional approach of cost-driven design towards exploring various other design metrics [116, 133, 134].

Some of these metrics were defined by [62, 135–137]. The cost of valued energy (CoVE) informs about the ratio of costs to revenue [136]. CoVE is similar to LCOE, with the difference that CoVE weighs energy based on the day-ahead market price. CoVE takes the same value as LCOE when the electricity prices are constant. The

net present value (NPV) is the discounted value of the cash flow over the lifetime. The internal rate of return (IRR) is used to estimate the profitability of potential investments. [135] proposed modified internal rate of return (MIRR) and [137] incorporated it in the design process for HAWTs. MIRR was defined to overcome the limitation of IRR, which is that the positive cash flow from the project is reinvested at the IRR.

As mentioned in the previous section, the only influencing factor not captured by the LCoE is the value of the generated electricity quantified by the electricity price. Traditionally, the electricity price has depended on various subsidy schemes described in [138, 139]. Two of the most commonly used schemes are the feed-in-tariff (FIT) and the feed-in-premium (FIP). In a FIT scheme, the renewable energy producers are paid a fixed price per unit of electricity fed into the grid. In a FIP scheme, the producers are paid a fixed premium in addition to the day-ahead electricity market (DAM) price received per unit of electricity fed into the grid.

The DAM prices are different for different bidding zones within a country. Most European countries have one or two bidding zones with very few exceptions [140]. All power plant owners throughout the bidding zone receive the same electricity prices. The merit order effect in the DAM shows that electricity prices negatively correlate with wind power production within that zone. Based on the nature of the local wind resource, every wind farm will experience a different correlation between its production and the DAM prices. These local correlations will affect the revenue streams of the wind farm owners.

DAM AND WIND SPEEDS CORRELATION

We developed the data-driven statistical model outlined in Figure 4.9 to verify and model the correlation between the DAM price and wind speeds. We used the wind speed time series data from the ERA5 reanalysis dataset [141] and the DAM price data from the ENTSOE-E transparency platform [142]. ENTSOE-E is responsible for collecting and publishing data related to electricity generation, transmission, and consumption in the European market.

Data preprocessing consisted of data cleaning, detrending, and removing outliers. Detrending is necessary to remove any inherent trend in the datasets to avoid spurious correlations [143]. DAM price data points three standard deviations apart were categorised as outliers. Since the wind speeds are from a modelled dataset, no data points were categorised as outliers. Temporal consistency in the datasets was maintained during these operations. The preprocessed time-series datasets were then used to investigate the correlation between the variables.

The Pearson coefficient was used to evaluate the degree of correlation between wind speeds and DAM prices. The coefficient indicates the direction and strength of the linear relationship between the two statistical variables. With X being the wind speed and Y being the DAM price, the coefficient is calculated as

$$R_{xy} = \frac{\text{cov}(X, Y)}{\sqrt{\text{var}(X)\text{var}(Y)}}, \tag{4.40}$$

where cov is the covariance and var is the variance of the variables.

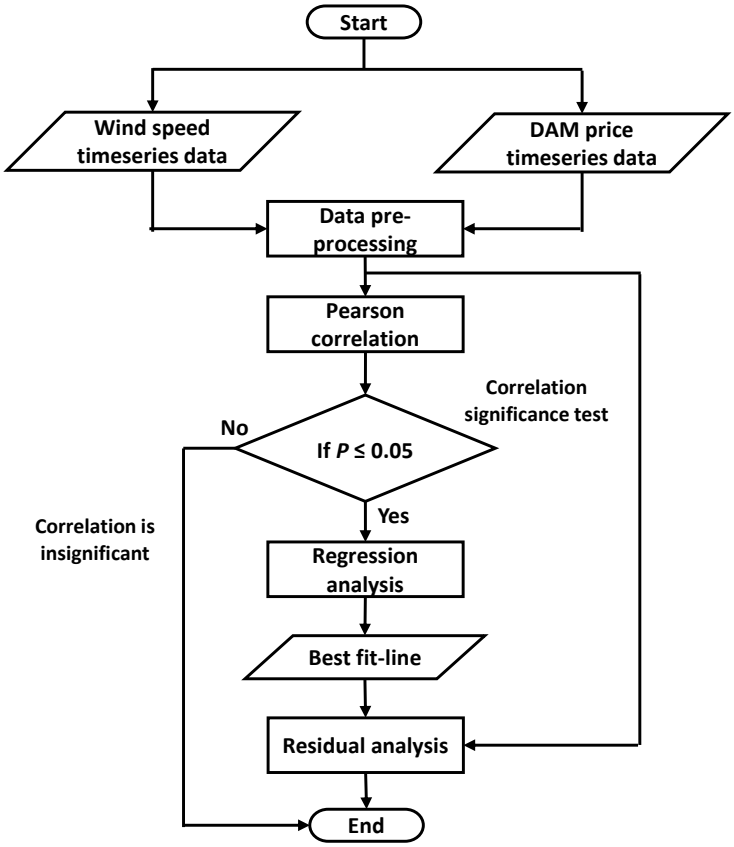

Figure 4.9: Flowchart of the correlation modelling method of DAM price and wind speeds.

A statistical significance test was then performed as a confirmatory test [144]. The P value should be smaller than the chosen significance level to confirm the analysis. The commonly accepted level is 5% and hence was used in this model. As a next step, the ordinary least squares method was used to model the relationship between the two variables, followed by a residual analysis to confirm the linearity of the relationship.

The energy price p can be modelled as a function of wind speed v_w using a a linear model based on historic data:

$$p(v_w) = p_0 + p_1 v_w. \tag{4.41}$$

CASE-STUDIES FROM GERMANY, DENMARK AND THE NETHERLANDS

An offshore location in Germany (54°N 7°E) is an example to investigate and illustrate the dependency of the electricity price on the wind speeds. The analysis is based on

a five-year historical dataset (2015 to 2019) with an hourly resolution. The height at which the wind speed data is evaluated is 350 m. The wind speed data is obtained from [141] and the electricity price data from [142].

Figure 4.10 and fig. 4.11 show the difference between the original and the preprocessed time series of DAM prices and wind speeds, respectively. The negative wind speed values in the preprocessed data are caused by detrending the time series. The price data follows a Gaussian distribution with a mean of 35 €/MWh and a standard deviation of 14 €/MWh. The wind speed data follows a Weibull distribution with a mean of 10 $\mathrm{m\,s^{-1}}$. The preprocessing removed around 1.4% of the total data points.

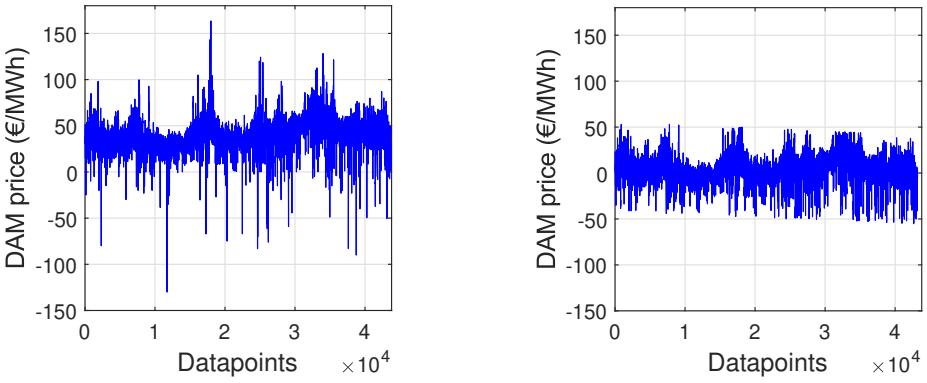

(a) Original time-series dataset.

(b) Preprocessed time-series dataset.

Figure 4.10: Original versus preprocessed DAM price time-series from Germany (2015-2019).

The Pearson correlation coefficient for the dataset is -0.33, and the P value is close to zero ($\ll 0.05$). This confirms the negative correlation between wind speeds and electricity prices. The result of the regression analysis is shown in Figure 4.12 as the best-fit line for the data cloud. On average, an increase in wind speed by 1 $\mathrm{m\,s^{-1}}$ leads to a drop of the DAM price by 0.9 €/MWh. The R^2 statistic of 0.11 indicates that the model does not fit the data perfectly. However, the residuals illustrated in fig. 4.13a and fig. 4.13b are normally distributed with a mean of zero, which validates the linearity of the correlation because the error is spread evenly on both sides of the regression line. Therefore, the model effectively captures the required pattern within the data.

A similar analysis was performed on three locations in the Netherlands, Denmark and Germany to check if this electricity price dependency on wind speeds can be observed in multiple European markets. Table 4.4 shows the statistical analysis results, and all the estimated parameters are significant (i.e. P values $\ll 0.05$).

The analysis confirms the general trend in the European electricity markets with high wind energy penetration that electricity generated at low wind speeds has a higher value than that generated at high wind speeds.

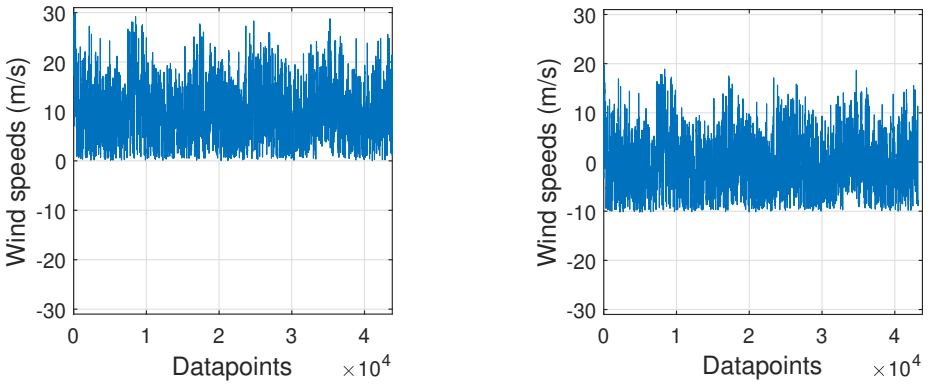

(a) Original time-series dataset.

(b) Preprocessed time-series dataset.

Figure 4.11: Original versus preprocessed wind speeds time-series from the offshore location in Germany (2015-2019).

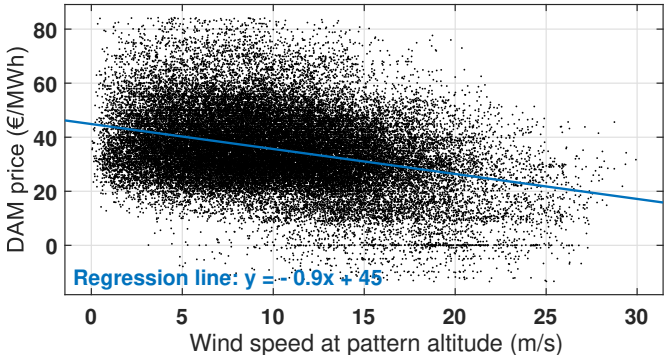

Figure 4.12: Regression analysis results of the DAM prices and wind speeds from Germany (2015-2019).

Table 4.4: Statistical model results: Electricity price dependency on wind speeds for three different European locations.

Location	**Correlation coefficient**	**Slope of regression line**
Netherlands (52.5°N, 4.25°E)	-0.15	-0.4
Denmark (55°N, 8°E)	-0.38	-0.9
Germany (53°N, 12°E)	-0.32	-1.2

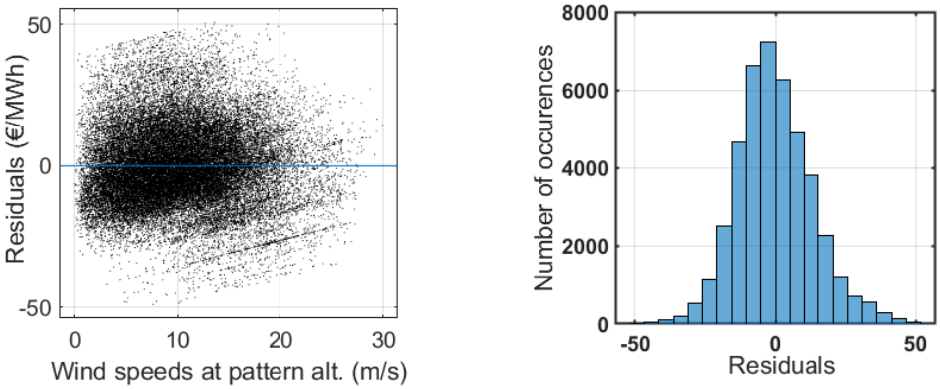

(a) Residuals plot.

(b) Distribution of residuals.

Figure 4.13: Residual analysis plots.

LEVELISED PROFIT OF ENERGY (LPOE)

For a subsidy-based revenue generation scenario, annual revenue can be directly estimated as the product of AEP and electricity price. As shown in the previous section, the DAM price could be modelled as a function of wind speeds. Therefore, for a DAM-based revenue generation scenario, annual revenue is modelled as follows

$$\text{Annual revenue} = N \times 8760 \int_{v_{\text{w,cut-in}}}^{v_{\text{w,cut-out}}} f(v_{\text{w,ref}}) P_{\text{e,avg}}(v_{\text{w,ref}}) p(v_{\text{w,ref}}) dv_{\text{w,ref}}, \tag{4.42}$$

where p is the electricity price in €/MWh and all the other variables retain their definition. The model assumes that the yearly wind statistics and the DAM price distribution are the same each year during the project's lifetime. Therefore, the annual revenue is also assumed to be constant over the entire project lifetime.

Considering the time-varying electricity price scenario, there is a need for a revenue-based metric analogous to the LCoE to compare different systems based on their potential to maximise revenue. The proposed economic metric is the levelised revenue of energy (LRoE) defined as

$$\text{LRoE} = \frac{\sum_{y=0}^{N_y} \frac{[p(y)+subsidy(y)]AEP(y)}{(1+r)^y}}{\sum_{y=0}^{N_y} \frac{AEP(y)}{(1+r)^y}}, \tag{4.43}$$

quantifying the average net present electricity price for a project over its entire economic lifetime in €/MWh. For better comparison, the LRoE is normalised with the average market price and denoted as the value factor (VF)

$$\text{VF} = \frac{\text{LRoE}}{\text{Average DAM price}}. \tag{4.44}$$

The normalised metric quantifies the difference between the average electricity price received by a producer in a time-varying electricity price scenario and the total

market average price. For example, a VF of 0.8 means that the system receives 80% of the average electricity price received by its competitors in the market.

Instead of using the LCoE alone, LCoE and LRoE should be used to compare technologies effectively. The difference between LRoE and LCoE is defined as the levelised profit of energy (LPoE)

$$\text{LPoE} = \text{LRoE} - \text{LCoE}. \tag{4.45}$$

To quantify the profitability of a certain investment in project planning we define the net present value (NPV)

$$\text{NPV} = \sum_{y=0}^{N_y} \frac{CF_y}{(1+r)^y}, \tag{4.46}$$

where CF is the net cash flow, i.e. the difference between the revenue and expenditure.

Since LCoE and LRoE are both discounted to account for the time value of money, they can also be used to calculate the NPV of the project as

$$\text{NPV} = E_{\text{lifetime}} \times \text{LPoE}, \tag{4.47}$$

where E is the discounted value of the total energy produced during its entire economic lifetime.

Since LPoE and NPV capture all four factors influencing the economics of AWE, they are more comprehensive metrics to compare different design choices. In addition to NPV, the internal rate of return (IRR) is another economic metric used to estimate the profitability of a project or an investment. The IRR is the discount rate which makes the NPV (essentially the LPoE) equal to zero. IRR can also be used as an alternative metric to LPoE. From the perspective of a business case, the decision for a project is generally based on the investors' target IRR requirement. In a DAM-based scenario, it is possible that the market price alone cannot achieve this target IRR. Therefore, an additional subsidy in the form of a FIP could be necessary to achieve the required IRR.

In addition to LCoE, these different metrics could be used to evaluate different system designs based on different objectives.

4.4. KEY-TAKEAWAYS

The cost model and the economic metrics defined in this chapter can be used to perform techno-economic analyses, system design optimisation studies, and evaluate business cases for specific market scenarios. It can be used to estimate the economic performance of a given system and site specifications if combined with a performance model. The generated results can assist in developing technology roadmaps and inform policymakers and organisations such as the International Renewable Energy Agency (IRENA) or the International Energy Agency (IEA).

LCoE is chosen as the design metric for further system design and scaling trends analysis in this thesis. This choice of metric is suitable for scenarios in which the

revenue scheme is dependent on subsidies rather than fluctuating electricity market prices. This is more relevant for early commercialising technologies like AWE. The revenue scheme might shift from subsidy-dependent to market-dependent in future scenarios with high technological maturity. In such scenarios, profit-based metrics such as the LPoE would be more relevant than cost-based metrics such as the LCoE.

5

System Design and Scaling Trends

Chapter 2 described the developed power curve model for fixed-wing ground-generation (GG) airborne wind energy (AWE) systems, Chapter 3 described the drivetrain concepts for power smoothing, and Chapter 4 presented the cost modelling of all the AWE components essential to compute the levelised cost of energy (LCoE). This chapter describes the framework which couples all the previous chapters together. It presents the developed multi-disciplinary design, analysis and optimisation (MDAO) framework, which employs models evaluating the wind resource, power curve, energy production, overall component and operation costs, and various economic metrics. This framework is used to design fixed-wing GG AWE systems based on the objective of minimising LCoE. The variables used to define the system are the wing area, aspect ratio, tether diameter and rated power of the generator. This framework is used to find optimal system designs for rated powers ranging from 100 kW *to* 2 MW.

The outline of this chapter is as follows. Section 5.2 presents the methodology and the underlying models used to identify the design drivers and trade-offs, Section 5.3 presents a reference case study exploring the system design for rated powers ranging from 100 kW *to* 2 MW. *This rated-power range is chosen since most AWE companies are targeting their first commercial system within a scale of* 100 kW, *and some of them are aiming for further upscaling up to a multi-megawatt scale. This section is followed by a sensitivity analysis to capture extreme scenarios as compared to the reference case study. Section 5.4 presents the key findings extracted from the case study.*

This chapter has been adapted from the following peer-reviewed article:

[42] R. Joshi, D. von Terzi, and R. Schmehl. "System design and scaling trends in airborne wind energy demonstrated for a ground-generation concept". In: Wind Energy Science (2025). DOI: 10.5194/wes-10-695-2025.

5.1. Introduction

The system design of AWE entails the design of the kite, the tether, and the ground station. The ground station consists of the drum, which supports the loads during operation and stores the tether; the drivetrain, which transfers and converts the mechanical power to electrical power; the yawing mechanism, which enables the kite to align with the wind direction; the launch and land system; and the control station. This work focuses on single systems and does not account for farm-level aspects. Including farm-level aspects will require wake models, cabling models, etc., which will influence the placement of systems and, hence, influence scaling based on area constraints. Therefore, as a first step, we aim to develop an understanding of the scaling of individual systems.

As explained in Chapter 3, the power output of GG AWE systems is oscillating by nature and needs to be smoothened to comply with grid codes before the systems can be connected to the electricity grid. This power smoothing can be achieved with intermediate storage components that act as buffers to charge and discharge during the operation [87]. Another approach is farm-level power smoothing by operating multiple AWE systems in a phase-shifted but synchronised manner. Although this approach is expected to reduce the requirement of the intermediate storage solution [49], it will pose a challenging active control problem. Three different types of drivetrain configurations, electrical, hydraulic and mechanical, depending on different storage solutions, were explored by [87]. Because of the commercial readiness and proven track record of comprising components, the electrical drivetrain is considered a more suitable drivetrain for market entry of AWE systems. Therefore, we limit the scope of the present work to the electrical drivetrain shown in fig. 5.1. It consists of a gearbox, generator, power electronics and an electrical storage unit, which could be a battery pack or a supercapacitor bank.

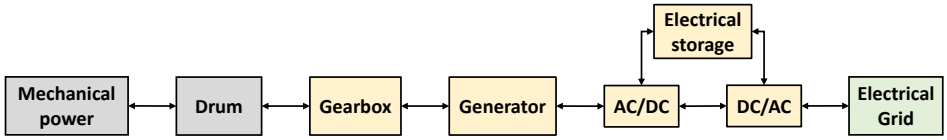

Figure 5.1: Electrical drivetrain architecture (adapted from [87]).

This chapter is structured as follows. Section 5.2 presents the methodology and the underlying models used to identify the design drivers and trade-offs, Section 5.3 presents a reference case study exploring the system design for rated power ranging from 100 kW to 2000 kW. This rated-power range is chosen since most AWE companies are targeting their first commercial system within a scale of 100 kW, and some of them are aiming for further upscaling up to a multi-megawatt scale [43]. This analysis is followed by a sensitivity analysis to capture extreme scenarios compared to the reference case study, and finally, Section 5.4 presents the key takeaways.

5.2. METHODOLOGY: DESIGN SPACE EXPLORATION

Valuable insights can be gained by examining how the design objective changes with variations in system design variables. This approach forms the basis for design space exploration and optimisation. By observing the sensitivity to design variables, we produce an optimal system design as a reference. The developed framework is based on the engineering field of multidisciplinary design, analysis, and optimisation (MDAO). MDAO tools and methodologies consider the interactions between different subsystems and disciplines, enabling a comprehensive assessment of a system's performance based on chosen objectives. This approach is often used in aerospace, automotive, and other industries where system complexity and the interplay between components are significant. Section 5.2.1 discusses the problem formulation and Section 5.2.2 presents the employed system design framework.

5.2.1. PROBLEM FORMULATION

Problem formulation is the description of the design objective, variables and constraints. It depends on the context that defines the settings in which the system will operate. The system's rated power is a requirement set before designing a system. The design objective is usually determined by the requirements set by the market for which the system is designed. This specific market deployment scenario can be defined by the wind conditions, discount rate and price. For a given design objective, certain design variables or constraints can have a high or low influence on the performance of systems. Variables to which the objective is highly sensitive are considered design drivers. Constraints could act as design limiters if they restrict the optimum design. The market and project-specific aspects primarily influence the constraints.

DESIGN OBJECTIVE

The design objective is the goal that the developer wants to achieve with the system. The most common but also conflicting objectives are higher energy production and minimum costs. Levelised cost of energy (LCoE) is a holistic metric that combines both objectives into one metric and is defined as

$$\mathrm{LCoE} = \frac{\sum_{y=0}^{N_y} \frac{\mathrm{CapEx}_y + \mathrm{OpEx}_y}{(1+r)^y}}{\sum_{y=0}^{N_y} \frac{\mathrm{AEP}_y}{(1+r)^y}}, \tag{5.1}$$

where CapEx is the capital expenditure, OpEx is the operational expenditure, r is the discount rate, AEP is the annual energy produced, y is the instantaneous year, and N_y is the project lifetime.

DESIGN VARIABLES

Design variables are the system design parameters which the developer can vary to maximise the performance of systems. In the case of wind turbines, rotor size is the variable that limits the power extraction for a given generator size. In contrast,

for AWE systems, the combination of the kite and the tether dimensions limits the power extraction. Therefore, for AWE systems, the tether is an additional component that must be designed in coherence with the kite and the generator. Table 5.1 lists the chosen system design variables, enabling the evaluation of relevant trade-offs with respect to the chosen design objective.

Table 5.1: Chosen system design variables characterising the kite, the tether and the drivetrain. These are the independent design variables.

Description	Parameter	Unit
Wing area	S	m^2
Aspect ratio	$\mathcal{AR}$	-
Maximum wing loading	$W_{l,max}$	kNm^{-2}
Maximum tether stress	$\sigma_{t,max}$	GPa
Power crest factor	f_{crest}	-

The kite is characterised by the wing area and the aspect ratio. The wing span is a dependent parameter. On one hand, with increasing wing area, the aerodynamic force increases, but on the other, the kite mass also increases. This increases the aerodynamic force component to compensate for the gravitational force, reducing the extractable power [40, 50, 51]. Moreover, larger wing areas and mass also lead to higher costs due to higher material usage. Higher aspect ratios reduce the induced aerodynamic drag, thereby increasing the aerodynamic efficiency and affecting the kite mass. These trade-offs are critical to capture in the system design process.

The tether is characterised by the maximum allowable wing loading and the maximum allowable tether stress. These limit the maximum force the tether can withstand for a given wing area and the maximum stress it can withstand with respect to its own cross-sectional area, respectively. Both of these parameters drive the tether diameter. Higher wing loading translates to higher tether force, enabling higher power extraction. However, to maintain stress levels in the tether while enabling higher tether force, the tether diameter must be increased. An increase in diameter has a penalising effect due to increased drag losses and increased mass. Moreover, the kite has to be structurally capable of withstanding higher loading, which leads to a higher kite mass. Higher maximum allowable tether stress reduces the tether diameter but negatively affects the fatigue lifetime of the tether, significantly increasing the replacement costs. These trade-offs are also critical to capture in the design process.

The power crest factor is the ratio of the generator's rated power to the system's rated power. This is relevant because the instantaneous power during a cycle is higher than the cycle average power of AWE systems. This effect is more pronounced for GG systems with reel-out and reel-in phases. Therefore, the drivetrain must be designed according to the peak power during the cycle. The power crest factor indicates the trade-off between capping the power at lower values, which will reduce the net cycle power but will also reduce the overall drivetrain costs.

Based on a certain set of system design variables, the operation of the AWE

system is optimised to maximise the electrical cycle average power for the input wind speeds. These operational design parameters are listed in Table 2.2. These essentially are the dependent design variables based on the system design variables. This optimisation of operational parameters is described in detail in Chapter 2.

DESIGN CONSTRAINTS

Design constraints are external factors that developers cannot control but must be considered and integrated into the design process. These are primarily derived from project-specific requirements, including safety and regulation requirements [145]. Table 5.2 lists the chosen design constraints.

Table 5.2: Chosen system design constraints to incorporate the project-specific safety and regulation requirements in the design process.

Description	Constraint	Unit
Available land area	$A_{oper} \leq A_{land}$	m^2
Operation height limits	$h_{min} \leq z_k \leq h_{max}$	m

The available land area A_{land} is usually a project-specific constraint, while the operation height limits h_{min} and h_{max} could be driven by safety and regulation requirements. The area of operation A_{oper} is the ground area determined by calculating the circular area using the projected tether length on the ground as the radius. In addition, noise and visual constraints could also be applied, but there is currently insufficient information available to quantify these constraints for AWE systems.

5.2.2. SYSTEM DESIGN FRAMEWORK

An integrated system design framework based on MDAO methodology is developed, incorporating models that cover wind resources, power production, energy production, and costs. [146] described a methodology to present the MDAO frameworks in a formalised manner through an extended design structure matrix (XDSM). Figure 5.2 shows the XDSM of the developed MDAO framework.

In the diagram, various block shapes and colours denote inputs, outputs, computational processes and loops. The MDA block is the controlling block that defines the framework's employed workflow. Thick grey lines denote the flow of data within the framework. Vertical connections from top to bottom denote input to the subsequent blocks, whereas the horizontal connections on either side of the blocks denote the outputs from the particular blocks. The execution order of blocks is denoted by sequential numbering starting from zero. If a block is a start and an endpoint for a loop, it is denoted by two numbers denoting the start and the end, respectively. A loop is denoted by $m \rightarrow n$ where $m \leq n$. The thin black line within the thicker grey lines denotes the process flow. The user inputs are defined in the white blocks at the top, which need to be defined initially; the design variables are

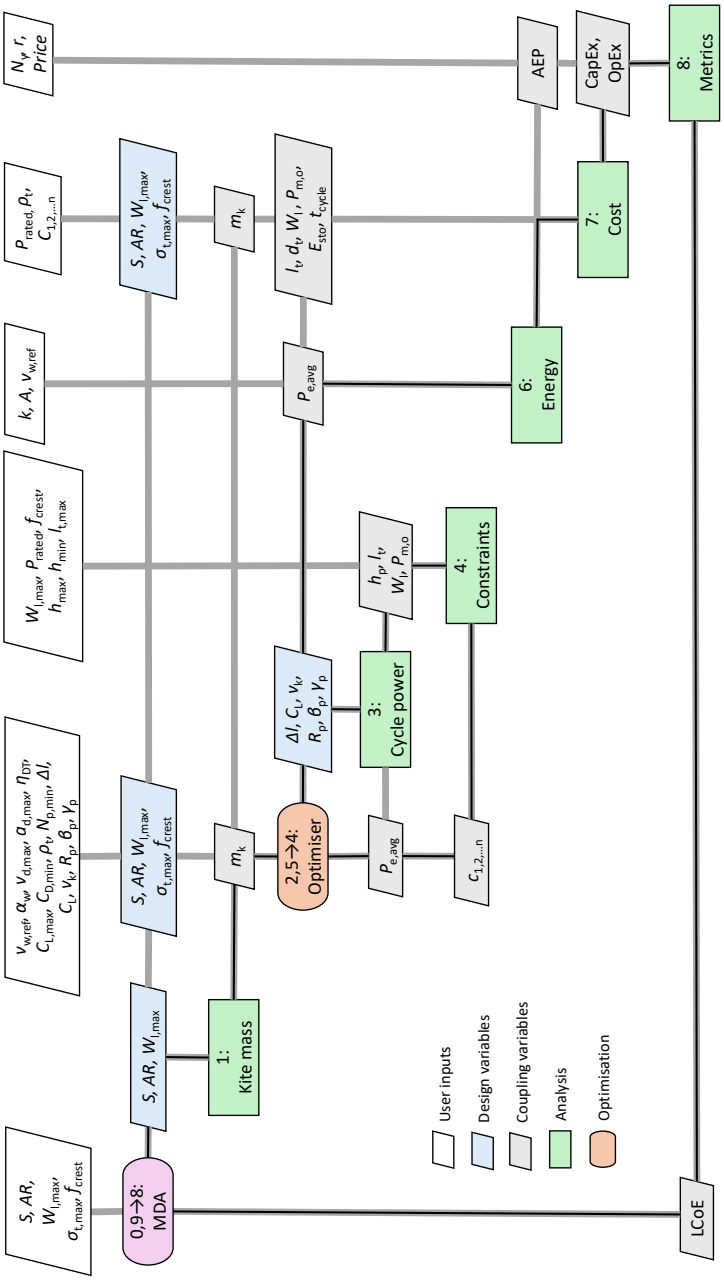

Figure 5.2: Extended design structure matrix (XDSM) of the developed design framework for airborne wind energy systems.

denoted by the blue blocks, and the coupling variables between computation blocks are denoted in grey blocks.

One iteration of the framework starts and ends at the MDA block denoted by '0,9' and includes the evaluation of all process blocks from 1 to 8. This evaluates the LCoE value for the input design based on the initialisation of variables and constraints. For every iteration, i.e., for every set of system design variables described in Table 5.1, the operational design variables described in Table 2.2 are optimised within the nested optimisation loop $2,5 \rightarrow 4$. This workflow can be deployed to evaluate a single design, a design space with many combinations of variables, or as a higher-level optimisation problem in which the system design variables are optimised until a chosen convergence criteria (e.g. minimum LCoE) is satisfied. The following sections describe the models used in the framework.

All the necessary models integrated into this framework have been described in detail in Chapters 2 to 4. The described system design framework, including the individual models, is implemented in MATLAB and is available open source through Zenodo and GitHub [147]. The following section presents a case study showcasing the functionality of the framework.

5.3. CASE STUDY

The case study determines optimal system configurations for rated power of 100, 500, 1000, and 2000 kW. A design space is then explored to identify configurations that minimize the LCoE for each rated power. A reference scenario is defined in the next section, followed by a sensitivity analysis.

5.3.1. REFERENCE SCENARIO

Table 5.3 lists the fixed parameters defining the reference scenario. The input wind resource to the cycle power model is defined by the combination of the wind speed at a fixed reference height h_{ref} and the vertical wind profile shape at that location. The chosen wind conditions of $v_{\text{w,mean}} = 8.5\text{ms}^{-1}$ and $\alpha_{\text{w}} = 0.2$ correspond to Class I wind turbine conditions as described in [148]. The cut-in and rated wind speeds depend on the design variables, but the cut-out wind speed is assumed constant at 25 ms^{-1} at the operational height. In later design stages, the cut-out wind speed will be determined using higher-fidelity engineering analyses. The wind speed limits are always with respect to the reference height h_{ref}. Since the framework does not employ an aerodynamic model, the wing aerodynamic properties are assumed constant for all designs. The underlying assumption is that the same airfoil is used for all the kite sizes. To account for a stall-safety margin and the 3-D wing aerodynamic effects, an airfoil efficiency factor η_{Cl} is applied on the maximum airfoil lift coefficient $C_{\text{l,max}}$ to impose an upper limit for the wing lift coefficient as

$$C_{\text{L,max}} = \eta_{\text{C}_\text{l}} C_{\text{l,max}}. \tag{5.2}$$

A land surface area constraint is not applied since this would be more relevant for farm-level studies. Neglecting this constraint will allow us to understand the

unconstrained potential of single systems. Similarly, the maximum operating height constraint is also not applied, as it is primarily driven by airspace regulations and is highly location-dependent. This is done by setting a relatively high upper limit of 1000m. On the other hand, a minimum operating height of 100 m is applied as a safety constraint. The maximum tether reeling speed $v_{\text{drum,max}}$ and acceleration $a_{\text{drum,max}}$ are a result of the limits driven by the drum dynamics.

Table 5.3: Fixed parameters describing the reference scenario.

Parameter	Description	Value	Unit
α_{w}	Wind shear coefficient	0.2	-
h_{ref}	Reference height	100	m
$v_{\text{w,mean}}$	Mean wind speed at ref. height	8.5	ms^{-1}
k	Weibull shape parameter	2	-
r	Discount rate	0.10	-
N_{y}	Project lifetime	25	years
$C_{\text{l,max}}$	Max. airfoil lift coefficient	2.5	-
η_{Cl}	Airfoil efficiency factor	0.80	-
$C_{\text{l,Cd,min}}$	Lift coefficient at minimum drag coefficient	0.65	-
$C_{\text{d,min}}$	Minimum drag coefficient	0.056	-
ρ_{t}	Tether material density	970	kgm^{-3}
$C_{\text{d,t}}$	Cross-sectional tether drag coefficient	1.2	-
h_{min}	Min. ground clearance	100	m
h_{max}	Max. operating height	1000	m
$v_{\text{drum,max}}$	Max. tether reeling speed	20	ms^{-1}
$a_{\text{drum,max}}$	Max. tether reeling acceleration	5	ms^{-2}
$N_{\text{p,min}}$	Minimum number of patterns per cycle	1	-

The following section shows the design space exploration results for the rated power of 500 kW.

Design space exploration for a 500 kW system

Table 5.4 shows the design space explored using the framework described in Section 5.2.2 for a system rated power of 500 kW. The variables and the optimisation objective are as described in Section 5.2.1. An even wider space was investigated, but only part of this space, around the optimal solution, is discussed in the following.

Table 5.4: Explored design space for 500kW rated power.

Variable	Range [min, max]	Step size	Unit
S	[50, 70]	10	m^2
$\mathcal{AR}$	[10, 14]	2	-
$W_{\text{l,max}}$	[2, 4]	1	kNm^{-2}
$\sigma_{\text{t,max}}$	[0.3, 0.5]	0.1	GPa
f_{crest}	[1.5, 2.5]	0.5	-

Two variables are varied independently, and the results are illustrated as LCoE contour plots and representative power curves. The combinations of variables are chosen based on the degree of the coupling between the two variables. The other variables are kept constant during this process. For example, the wing area is varied with maximum wing loading since they are coupled through the tether force. Maximum wing loading is varied with maximum allowable tether stress since they are coupled through the tether diameter and characterise the tether. The wing aspect ratio is varied with wing area since they characterize the kite. The power crest factor is varied with the wing area since the wing area significantly influences the extractable power and the power crest factor limits this power by limiting the generated rated power. Overall, the wing area is a key parameter characterizing the size and power output of GG AWE systems.

Figure 5.3 and fig. 5.4 show the computed LCoE and associated power curves, respectively, for varying wing area and maximum wing loading. The optimal wing area and maximum wing loading values resulting in the minimum LCoE of 142 €/MWh are 60 m^2 and 3 kNm^{-2}, respectively. Limiting the wing area and the wing loading to lower values limits the power extraction and increases the LCoE. Some configurations cannot reach the specified rated power target of 500 kW as seen in fig. 5.4. These are the combinations with smaller wing areas and smaller maximum wing loading. Increasing the area and loading of the wing increases the kite mass, which in turn increases the losses due to gravitational effects, resulting in an increased LCoE. The system configurations with lower LCoEs are the combinations of smaller wing areas with higher wing loading or larger wing areas with lower wing loading, consequently resulting in the optimum value, as seen in fig. 5.3.

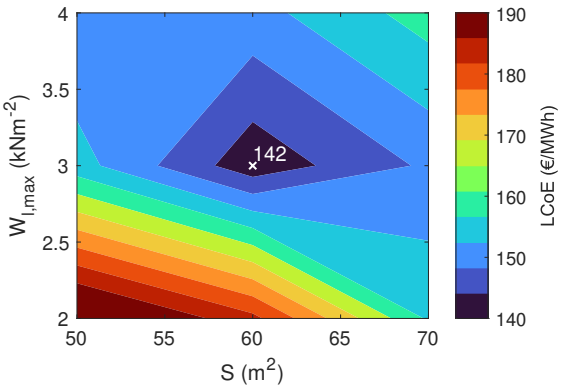

Figure 5.3: LCoE as a function of wing area S and maximum wing loading $W_{l,max}$. The other design variables are held constant with the following values: aspect ratio $\mathcal{AR} = 12$, maximum tether stress $\sigma_{t,max} = 0.4$GPa, and power crest factor $f_{crest} = 2$.

Figure 5.5 and fig. 5.6 show the computed LCoE and associated power curves, respectively, for varying maximum wing loading and tether stress. Maximum wing

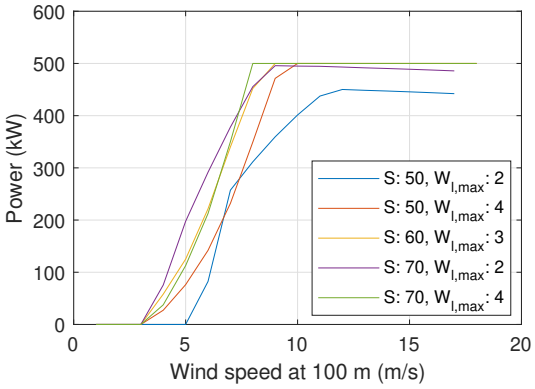

Figure 5.4: Power curves of a few system configurations within the design space illustrated in fig. 5.3. The configurations with smaller wing areas and smaller maximum wing loading cannot reach the rated power of 500kW.

loading primarily affects the maximum power output, while maximum tether stress has a major influence on the tether lifetime. The combined effect of these two variables on the LCoE is highly non-linear. The two parameters also affect the tether diameter, thereby impacting the tether drag losses. The minimum LCoE of 142 €/MWh is reached for the combination of max wing loading of 3kNm^{-2} and a maximum tether stress of 0.4 GPa.

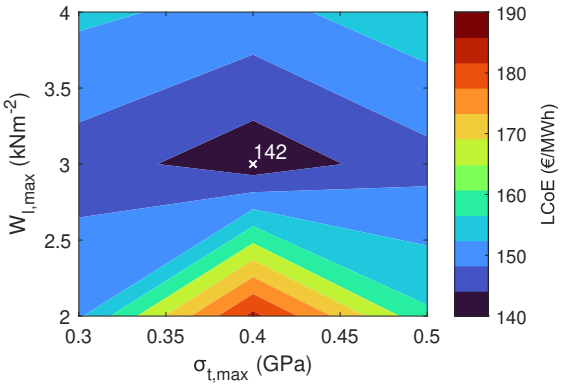

Figure 5.5: LCoE as a function of maximum wing loading $W_{l,max}$ and maximum tether stress $\sigma_{t,max}$. The other design variables are held constant with the following values: wing area $S = 60\text{m}^2$, aspect ratio $\mathcal{AR} = 12$, and power crest factor $f_{crest} = 2$.

Figure 5.7 and fig. 5.8 show the computed LCoE and associated power curves, respectively, for varying wing area and aspect ratio. Compared to other variables,

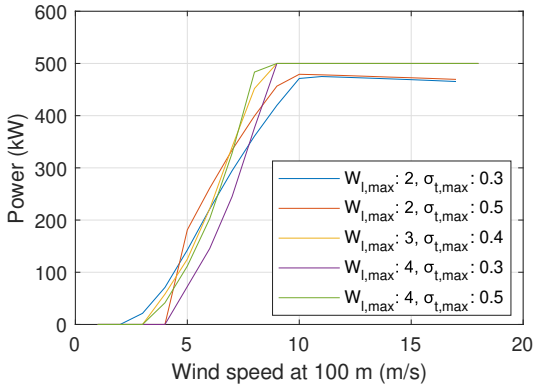

Figure 5.6: Power curves of a few system configurations as illustrated in fig. 5.5. The configurations with lower values of maximum wing loading cannot reach the target rated power of 500 kW.

it is observed that the aspect ratio has a small influence on the LCoE. The figure indicates that the LCoEs computed with aspect ratios of 10 and 12 are very similar. Unlike the configurations from fig. 5.4 and fig. 5.6, all the combinations in this design space reach the target rated power of 500 kW. The variation of wing area has a major effect on the power curve, whereas, for a given wing area, the effect of variation of the aspect ratio is minimal. This is the reason for the clusters of power curves, as seen in fig. 5.8. The rated power is achieved at relatively lower wind speeds with increasing wing area.

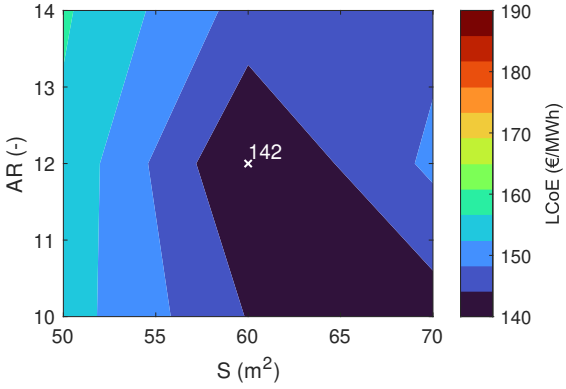

Figure 5.7: LCoE as a function of wing area and aspect ratio. The other design variables are held constant with the following values: maximum wing loading $W_{l,max} = 3 kNm^{-2}$, $\sigma_{t,max} = 0.4 GPa$, and power crest factor $f_{crest} = 2$.

Figure 5.9 and fig. 5.10 show the computed LCoE and associated power curves,

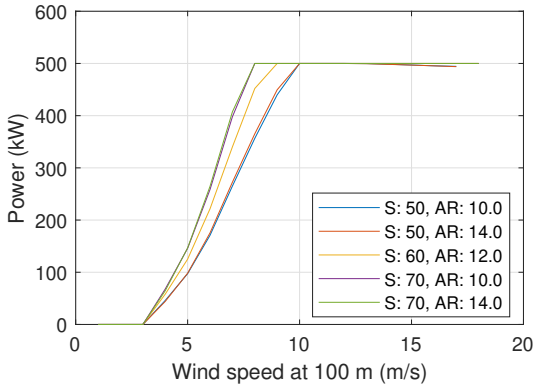

Figure 5.8: Power curves of a few system configurations as illustrated in fig. 5.7. The configurations with the same wing area are clustered together since the influence of the aspect ratio is relatively smaller than the influence of the wing area.

respectively, for varying wing area and the power crest factor. Since the power crest factor limits the rated generator power, consequently limiting the maximum reel-out power, the power curves show that for smaller crest factors, the system cannot reach the rated power of 500 kW. A higher crest factor means larger drivetrains and, hence, higher costs. Since the rated power is capped at 500kW, a crest factor of two gives the minimum LCoE.

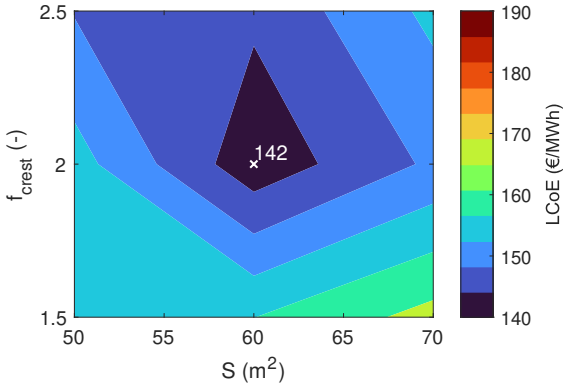

Figure 5.9: LCoE as a function of wing area and power crest factor. The other design variables are held constant with the following values: aspect ratio $\mathit{AR} = 12$, maximum wing loading $W_{\mathrm{l,max}} = 3\mathrm{kNm}^{-2}$, and $\sigma_{\mathrm{t,max}} = 0.4\mathrm{GPa}$.

Based on the above results, the optimal system configuration produces the power curve depicted in fig. 5.11. The values of the design variables are $S = 60\mathrm{m}^2$, $\mathit{AR} = 12$,

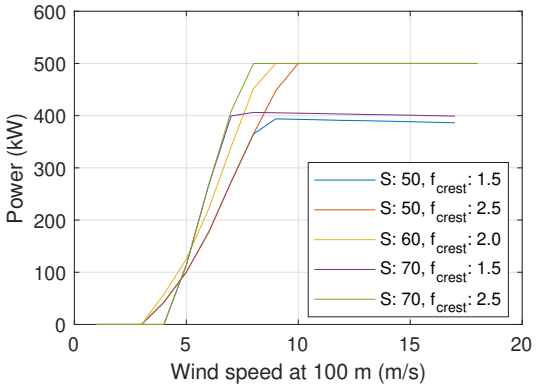

Figure 5.10: Power curves of a few system configurations as illustrated in fig. 5.9. The maximum reel-out power of configurations with a power crest factor $f_{\text{crest}} = 1.5$ is capped at 750 kW and hence they can only attain a rated power of 400 kW.

$W_{\text{l,max}} = 3\text{kNm}^{-2}$, $\sigma_{\text{t,max}} = 0.4\text{GPa}$, $f_{\text{crest}} = 2$. The cut-in, rated, and cut-out wind speeds are 6, 11, and 20ms^{-1} at the reference height of 100 m.

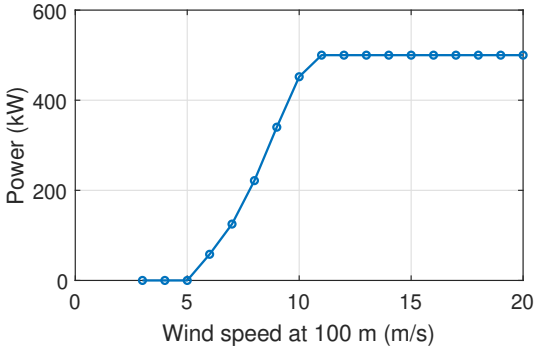

Figure 5.11: Power curve of the 500 kW system based on the optimal system design minimising the LCoE.

Figure 5.12 illustrates the shares of the subsystems in the total capital expenditure (CapEx), operational expenditure (OpEx) and the LCoE. The CapEx is dominated by the kite structure costs resulting directly from the kite mass and the ultracapacitor costs resulting from the power smoothing requirement. The OpEx is composed of the replacements of the ultracapacitors and the tether, along with the balance of system costs. These are again reflected in the LCoE split. Compared to horizontal axis wind turbines (HAWTs), one of the key characteristics is the ratio of total CapEx and the lifetime OpEx. The ratio of CapEx to lifetime OpEx for onshore wind turbines is

around 2 : 1 and is higher for offshore applications [8]. In the case of AWE, the OpEx, considering a lifetime of 25 years, is 2600 k€, and hence this ratio is around 0.7 : 1. This indicates that the GG AWE systems do not have high upfront costs but more spread-out costs, which can be an advantage in financing compared to HAWTs.

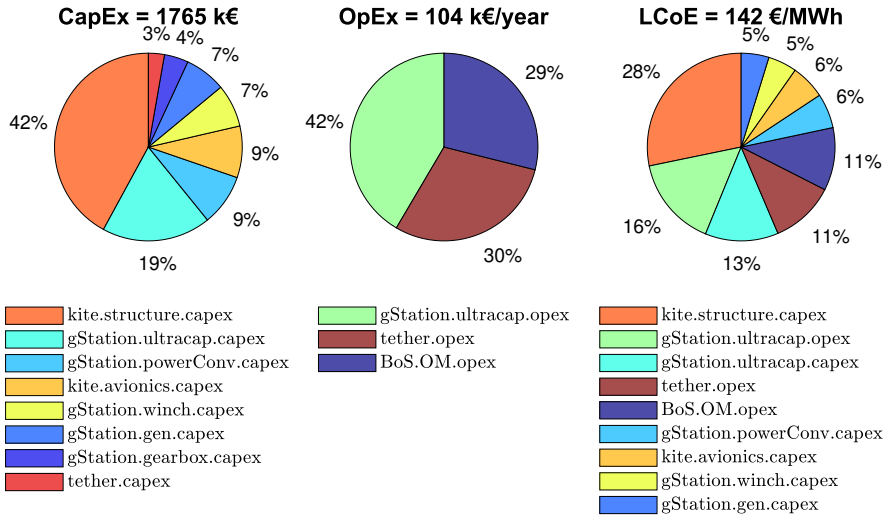

Figure 5.12: Share of subsystem component costs (≥ 2%) within the capital expenditure (CapEx), operational expenditure (OpEx) and the LCoE. The terminology and the nomenclature used in the legend are described in [91].

A similar detailed analysis was performed for the rated power of 100, 1000, and 2000 kW. The following section jointly investigates all power ratings to derive insights into the scaling behaviour of fixed-wing GG AWE systems.

Scaling trends with 100 kW to 2000 kW systems

Table 5.5 lists the explored design space with the system design variables as defined in Section 5.2.1. The lower and upper limits of the design variables are based on the design space explored for the 500 kW system, available prototype data from companies, and engineering guesses. Our analysis showed that the optimum values always lie within the design space considered in this study for chosen system sizes.

Figure 5.13 and fig. 5.14 show the computed LCoE, capacity factor (cf) and the corresponding power curves for the optimal system configurations. The computed LCoE is minimum for the 500 kW size, while the capacity factor monotonously decreases with increasing system size.

Table 5.6 shows the values of the design variables and some key specifications describing the optimal configurations minimising the LCoE for the four rated powers. This results from the exhaustive parametric sweep within the design space defined

Table 5.5: Explored design space for the rated power of 100, 1000, and 2000 kW.

Variable	Range [min, max]	Step size	Unit
S	[10, 170]	10	m^2
AR	[8, 14]	2	-
$W_{l,max}$	[1, 5]	1	kNm^{-2}
$\sigma_{t,max}$	[0.3, 0.5]	0.1	GPa
f_{crest}	[1.5, 2.5]	0.5	-

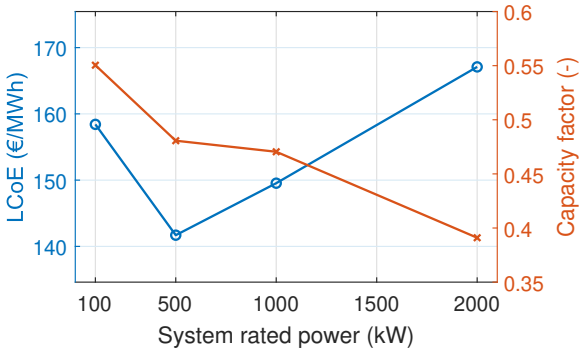

Figure 5.13: LCoE and capacity factor (cf) of the optimal system configurations for the four specified rated powers in the reference scenario.

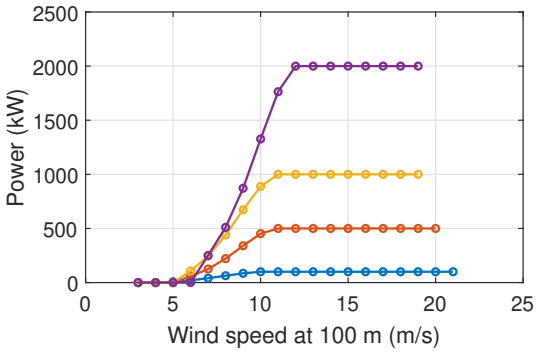

Figure 5.14: Power curves of the optimal system configurations for the four specified rated powers in the reference scenario.

in Table 5.5. It can be seen that a linear relationship between the rated power and the optimal wing area does not exist. The kite area specific power for the 100 kW system is 5 kWm^{-2} and for the 2000 kW system is 12.5 kWm^{-2}. These results indicate that the costs increase faster with size than the energy produced. This effect can be associated with the square-cube law of area and volume scaling,

consequently affecting performance and mass. The maximum wing loading, which essentially translates to tether diameter, increases with increasing power rating. It is intuitive that for larger systems, larger tethers will enable higher power extraction. Other design variables, such as the aspect ratio, maximum allowable tether stress, and power crest factor, remain constant for all power ratings. The power crest factor value of two shows that the most economical configuration is when the generator capacity is at most twice the rated power of the system to incorporate the peak reel-out power. Beyond this, the costs scale faster than the gain in power. The cut-in and the rated wind speeds for the optimal configurations increase with size and mass, reducing the capacity factor, as seen in fig. 5.13.

Table 5.6: Optimum values resulting from an exhaustive parametric sweep within the design space defined in Table 5.5 that minimise the LCoE for the four rated powers, and some key resulting specifications.

P_{rated} (kW)	100	500	1000	2000
S (m^2)	20	60	110	160
$\mathcal{AR}$ (−)	10	12	10	10
$W_{\text{l,max}}$ (kNm^{-2})	2	3	3	4
$\sigma_{\text{t,max}}$ (GPa)	0.4	0.4	0.4	0.4
f_{crest} (−)	2	2	2	2
m_{k} (kg)	700	2792	5857	10663
d_{t} (cm)	1.13	2.39	3.24	4.51
$v_{\text{w,cut-in}}$ (ms^{-1})	5	6	6	7
$v_{\text{w,rated}}$ (ms^{-1})	10	11	11	12
$v_{\text{w,cut-out}}$ (ms^{-1})	21	20	19	19
CapEx (k€)	495	1765	3656	6864
OpEx (k€/yr)	21	104	213	388

Power harvesting factor, specific power, and coefficient of power trends

A commonly used non-dimensional metric in the literature to quantify the performance of AWE systems is the power harvesting factor ζ [149]. It is defined as the ratio of the extracted power to the kinetic energy flux through a cross-sectional area equal to the wing area,

$$\zeta = \frac{P}{\frac{1}{2}\rho S v_{\text{w}}^3}. \tag{5.3}$$

Figure 5.15 depicts the computed values for the optimal system configurations. The trend shows that for LCoE-optimised systems, the extractable power per unit wing area shows diminishing marginal gain with increasing wing area.

The specific power of horizontal axis wind turbines (HAWTs) is defined as the ratio of the rated turbine power to the rotor-swept area. The specific power of HAWTs designed for different markets and wind speed classes are within the range of 200-400 Wm^{-2} [10]. The turbines at the lower end of this range are designed for lower wind speed sites to maximise the energy capture. Since the swept area of AWE

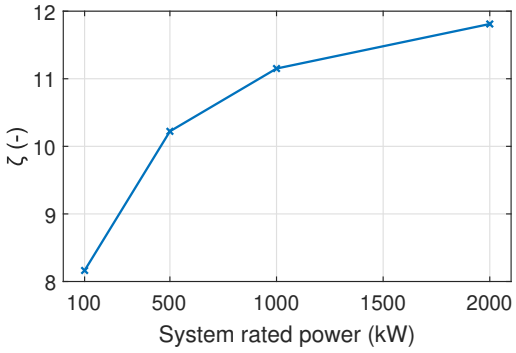

Figure 5.15: Power harvesting factors of the optimal system configurations.

systems generally varies with the operation and control strategies, a definition based on the swept area is not practical. Therefore, we define the specific power for AWE systems using the kite wing area instead of the swept area as

$$SP_S = \frac{P_{\text{rated}}}{S}. \tag{5.4}$$

Figure 5.16 illustrates this specific power and maximum wing loading for the LCoE-optimised system configurations. Both parameters increase with rated power. In contrast to this, the LCoE-optimised HAWTs have a constant specific power in the range of 200-400 $\text{Wm}^{-}2$ [10], irrespective of rated power. This shows the difference in scaling behaviours of GG AWE systems and HAWTs. Together, both of these trends can indicate the choice of wing area and tether combination for any power rating that minimises LCoE. The results listed in Table 5.6 are characterised by a constant optimal power crest factor of two. Hence, in addition to the wing area and tether combination, the drivetrain size that minimises LCoE will be two times that of the targetted rated power.

[69] used a different reference area to define a power coefficient and specific power, given as

$$A_{\text{ref}} = \pi b^2. \tag{5.5}$$

Geometrically, this represents the area of a circle using the wing span of the kite as the radius. This is analogous to calculating the swept area of wind turbines using the blade length as the radius. The resulting coefficient of power is defined as

$$C_{\text{p,Aref}} = \frac{P_{\text{rated}}}{\frac{1}{2}\rho A_{\text{ref}} v_{\text{w,rated}}^3}. \tag{5.6}$$

Figure 5.17 depicts the specific power and power coefficient using the above definition of the reference area. Both parameters are increasing with kite size similar to fig. 5.16. The order of magnitude corresponds to that commonly observed for HAWTs, though the definition of the parameters is different. Though the power output per reference area increases with increasing rated power, it shows that the LCoE-optimised system is not an energy-yield-optimised system.

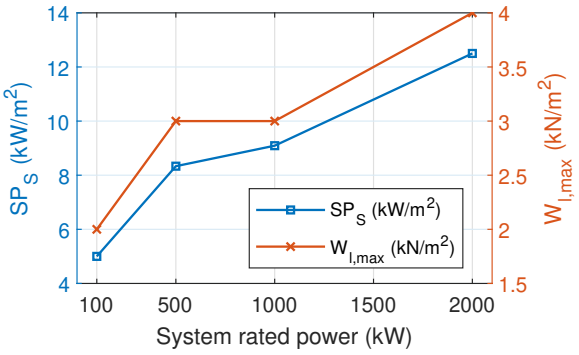

Figure 5.16: Specific power using the kite wing area on the left axis and maximum wing loading on the right axis. The plateau in the maximum wing loading trend is due to the step size used in the design space.

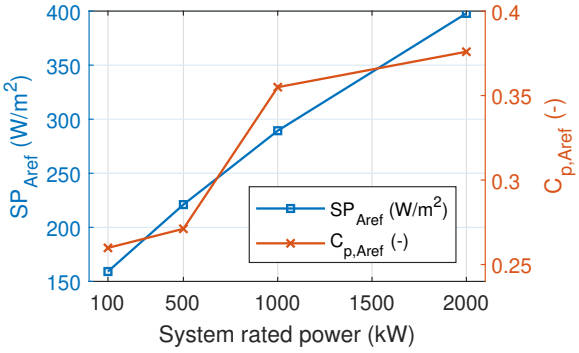

Figure 5.17: Specific power and power coefficient using the reference area definition as proposed by [69].

5.3.2. Scenario sensitivity

To understand the sensitivity of the presented solutions, we investigated the deviations from the reference scenario as described in Table 5.7. These deviations represent more extreme scenarios in technological improvements, environmental conditions, and market characteristics. The sensitivity with respect to kite mass (scenario 1) and ultracapacitor costs (scenario 2) was considered since these components are dominating the LCoE. Moreover, the grid operator may allow for electricity to be taken from the grid during reel-in, which will take away the storage costs required for power smoothing. The sensitivity to the discount rate (scenario 3) is of interest because geopolitical phenomena such as recession or inflation can affect the interest rates. Scenario 4 and 5 capture extreme variations of the wind conditions.

Table 5.7: Scenarios defined for sensitivity analysis in comparison with the reference scenario.

No.	Scenario	Assumptions against the Reference scenario
1	Reduced m_k by 50%	Steep technological advancements reducing the kite mass by 50 %
2	No storage	No power smoothing requirement from grid
3	Increased r to 15%	Higher discount rates due to uncertainties
4	$\alpha_w = 0$	Environmental conditions with no wind shear (α_w is the wind shear coefficient)
5	$\alpha_w = 0, v_{w,mean} = 10 ms^{-1}$	No wind shear but high mean wind speed, representing wind turbine Class I conditions

SCALING TRENDS

Figure 5.18 depicts the LCoE for the optimal system configurations in all scenarios. The reduced kite mass and the removal of storage costs scenarios show a significant reduction in the absolute LCoE values for all power ratings. However, the optimum system size with the minimum LCoE is still 500 kW in all the scenarios. These two curves are flatter than the other scenarios, indicating that the optimum might shift towards larger power ratings with extreme technological improvements, such as mass reduction $\geq 50\%$. The increased discount rate scenario raises the reference scenario curve uniformly, maintaining the same gradient between the points. This is because it does not physically affect scaling but just decreases the present value of future cash flows. The no wind shear scenario also increases the LCoE values since it reduces the magnitude of wind available at higher heights, consequently resulting in lower energy production as compared to the reference. This impact increases with size since heavier systems have higher cut-in wind speeds. The combination of no wind shear but increased mean wind speed balances the loss with the gains, resulting in similar values to the reference. These scenarios only consider single systems, but farm-level aspects such as wake losses, cabling costs, and area constraints will influence these trends and could shift the optimum towards larger power ratings.

Compared to Table 1.2, which lists the LCoE values for AWE systems reported in the public domain, the LCoE values found within this study lie on the upper end of the spectrum. Moreover, [53, 55] had a similar finding to our study about soft-wing systems that the LCoE had a minimum at 200 kW rated power and increased with further upscaling. [150] reported the global averages of LCoEs for different renewable energy technologies in 2023. The onshore wind was around 33 €/MWh, utility-scale solar PV was around 44 €/MWh, and offshore wind was around 75 €/MWh. All these technologies have experienced steep reductions in LCoE over the past half-century due to technological advancements and maturity. A similar trend could likely be predicted for AWE systems, which will further reduce the LCoE values in the next decade.

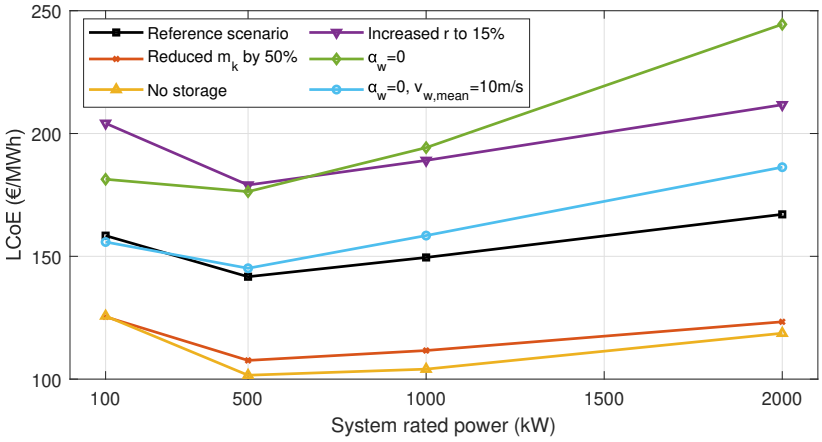

Figure 5.18: LCoE vales for the four rated powers evaluated for the considered scenarios in comparison to the reference.

5

Optimal system configurations

Table 5.8 lists the optimal values for the design parameters and some of the key resulting system specifications that minimise the LCoE of the 500 kW system. The computed values vary slightly across all scenarios based on their effect. For example, the optimum wing area in scenario 1, considering a reduced kite mass, is larger since the penalty due to the gravitational force is lower than in the reference scenario. This also allows for a larger tether diameter by increasing the maximum tether stress value, thereby reducing the tether replacement costs.

5.3.3. Discussion

Unlike HAWTs, fixed-wing GG AWE systems do not show distinct upscaling benefits when scaling up to megawatts. The unfavourable scaling of kite mass drives this outcome, as the kite has to use part of its aerodynamic force to compensate for gravity, which is increasingly penalising with size. Since this study is focused on single systems, farm-level aspects which can influence scaling are not reflected in the results. Having fewer systems in a single farm reduces the installation, operation and maintenance costs and hence would motivate larger individual systems. Also, area constraints will likely drive the solution towards larger systems to reduce the overall farm-LCoE. As a result of these effects not being considered in this study, the optimum system size could potentially increase due to technological improvements in materials and manufacturing methods decreasing the kite mass. The presented framework can be coupled with approaches that evaluate an entire energy system to analyse larger-scale effects. [151] looked at the value of AWE farms to the electricity system based on a metric known as the marginal system value (MSV). This metric quantifies the additional value that one extra unit of electricity generated by the AWE system brings to the overall energy system. In their analysis, they

Table 5.8: Optimum values resulting from an exhaustive parametric sweep within the design space that minimises the LCoE for all power ratings in all scenarios, and some key resulting system specifications.

Scenario		1	2	3	4	5
	Reference	Reduced m_k	No storage	Increased r	$\alpha_w = 0$	Higher wind
S (m^2)	60	70	50	60	60	60
$\mathcal{AR}$ (−)	12	10	10	12	10	8
$W_{l,max}$ (kNm^{-2})	3	3	3	3	3	3
$\sigma_{t,max}$ (GPa)	0.4	0.3	0.4	0.4	0.4	0.4
f_{crest} (−)	2	2	2	2	2	2
m_k (kg)	2729	1634	2164	2792	2700	2682
d_t (cm)	2.39	2.99	2.19	2.39	2.39	2.39
$v_{w,cut-in}$ (ms^{-1})	6	5	6	6	7	7
$v_{w,rated}$ (ms^{-1})	11	10	12	11	13	14
$v_{w,cut-out}$ (ms^{-1})	20	19	19	20	25	25
CapEx (k€)	1765	1490	1249	1765	1673	1639
OpEx (k€/yr)	104	94	51	104	95	111

included vertical wind profiles and optimised the flight trajectories of AWE systems to maximum average power. Their overarching conclusion was that AWE systems and wind turbines are interchangeable technologies since they have similar power production profiles. [151] found that small AWE systems generally have more full-load hours than large systems, which aligns with our finding of decreasing capacity factors with increasing size. A key difference in their approach was that MSV is a cost-independent metric which tries to quantify the added benefit of AWE systems in terms of energy production. [152] conducted a study on the integration of AWE at the European energy system level. In their analysis, they used the versions of the power, CapEx, and OpEx models used in our present work, which were still in the development phase. They also concluded that the AWE systems perform similarly to the wind turbines in offshore scenarios, and the competitiveness is heavily dependent on the total costs. However, [152] found that AWE systems have an advantage onshore due to better wind resource availability at higher altitudes than the average hub heights of wind turbines. The conclusions of these earlier studies align with the findings of the present work, but it will be beneficial to perform such studies again using the models and the presented system designs.

5.4. KEY-TAKEAWAYS

An MDAO framework was developed to understand the scaling behaviour of fixed-wing GG AWE systems using LCoE as the design objective to conduct a holistic system performance assessment. This was applied to the fixed-wing GG AWE concept. System design parameters such as the wing area, aspect ratio, maximum wing loading, maximum tether stress and the power crest factor were chosen as independent variables to systematically explore the design space. These parameters

were optimised for the system sizes of 100, 500, 1000 and 2000 kW.

The minimum LCoE was found for the 500 kW system, and the extractable power per unit wing area shows diminishing marginal gain with increasing wing area. This shows that there is no distinct benefit in upscaling the systems to multiple megawatts in terms of LCoE. This outcome is due to the penalising effect of the kite's weight on energy production and costs. Increasing rated power demands a larger kite, and since the mass increases rapidly with size, this has a negative effect since part of the aerodynamic force is used to counter the gravitational force. As a result, there is an increase in the cut-in wind speed, followed by an increase in the rated wind speed. Therefore, we see a decrease in capacity factor with increasing rated power. The primary cost-driving components for fixed-wing GG AWE systems are the kite mass, storage replacements and tether replacements. Unlike conventional wind turbines, the total lifetime operational costs of AWE systems are equal to or even exceed the initial investment costs. This distribution of expenses over the project's lifetime reduces upfront investments for project financing, which will have significant implications, particularly in markets where securing substantial initial investments is challenging. Sensitivity analyses were performed with scenarios representing extreme environmental conditions, financial assumptions and technological improvements. These results show the same scaling trend indicating sufficient robustness of the conclusions made in this work.

We suggest that academic efforts such as defining reference models and developing higher-fidelity tools, together with industrial efforts to develop commercial products, should target the system sizes in the 500 kW-range. The results show the importance of focusing research efforts on kite design, primarily to reduce mass by investigating innovative materials and manufacturing techniques. Additionally, we recommend research to improve tether design and system operation to increase fatigue life and minimise replacements. We also recommend exploring economic metrics that go beyond LCoE and other value propositions of AWE compared to HAWTs, such as the requirement of a smaller support structure, easier installation and logistics, etc. Factors that can drive the optimum to larger systems could be farm-level effects since having fewer systems generally reduces the overall installation and operation costs. Though the analysis presented in this paper was focused on fixed-wing GG systems, the key conclusions about the scaling behaviour will most likely hold for other concepts as well. This can be investigated using models tailored to specific concepts. Such system-level insights are important to guide the research and development of AWE technology.

6

CONCLUSIONS

This dissertation presents a holistic exploration of the design and scaling trends of fixed-wing ground-generation (GG) airborne wind energy (AWE) systems based on the levelised cost of energy (LCoE). The developed multidisciplinary design, analysis, and optimisation (MDAO) framework has the potential to guide AWE technology development by identifying key trade-offs and scaling trends. This has significant implications for establishing industry roadmaps, research priorities, and commercial strategies. The following are the key findings, limitations and implications of this study.

6.1. KEY FINDINGS

- The strong interdependencies between kite size, tether dimensions, and drivetrain components influencing the system performance highlight the importance of holistic design optimisation frameworks.
- Kite mass significantly impacts the system performance since part of the aerodynamic force is used to compensate for weight. The reel-out phase is negatively affected by kite mass, whereas the reel-in phase is positively affected since a component of weight reduces the energy required to reel in the kite.
- The primary cost drivers for fixed-wing AWE systems are kite mass, tether replacements, and storage costs. Operational costs over the project's lifetime often exceed initial investments, making AWE systems more financially accessible in markets with limited upfront capital availability.
- Power smoothing is one of the key challenges of AWE, which influences the drivetrain sizing. Drivetrain costs constitute about 50% of the LCoE, making their inclusion critical in scaling studies. While electrical drivetrains offer greater commercial readiness and reliability, hydraulic and mechanical drivetrains may become cost-effective for larger systems if developed further.
- Unlike horizontal-axis wind turbines (HAWTs), fixed-wing AWE systems exhibit diminishing returns with upscaling beyond 500 kW rated power. Larger systems

face penalties from increased kite mass, which leads to higher cut-in wind speeds, reduced capacity factors, and increased costs.

6.2. LIMITATIONS

- The quasi-steady power model does not account for inertial effects, which are expected to become significant as system sizes increase. This may lead to overly optimistic performance estimates for larger systems.
- The drivetrain cost and performance models rely on linear scaling assumptions and limited datasets, which may not fully capture the complexity of the operational dynamics of the three investigated concepts.
- While the scaling insights and methodology are robust, conclusions are primarily derived for fixed-wing GG systems. Other AWE concepts may exhibit different scaling behaviours depending on their unique operational and structural characteristics.
- The lack of high-fidelity simulation data and limited operational data from large-scale prototypes restricted the ability to validate findings under real-world conditions.

6.3. OUTLOOK & IMPLICATIONS

- The near-term focus of commercialising products and reference designs should be on the 500 kW system range. This offers an optimal balance between performance, costs, and scalability. The development of reference models and higher-fidelity simulation tools will be essential for refining system-level insights and validating assumptions.
- Efforts should focus on reducing kite mass through innovative materials and manufacturing techniques, improving tether fatigue life, and optimising system operation to minimise replacements.
- Larger system sizes may become viable if farm-level cost reductions (e.g., fewer systems reducing installation and operation costs) and technological advancements can offset diminishing returns. Drivetrain technologies, such as hydraulic and mechanical concepts, should be further investigated for feasibility and scalability.
- Though the methodology was focused on fixed-wing GG systems, it can be adapted to other AWE concepts with tailored models, enabling broader insights into scaling and design. This adaptability positions the framework as a valuable tool for guiding the evolution of AWE technology.

BIBLIOGRAPHY

[1] THE EUROPEAN PARLIAMENT AND THE COUNCIL OF THE EUROPEAN UNION. *DIRECTIVE (EU) 2023/2413 OF THE EUROPEAN PARLIAMENT AND OF THE COUNCIL of 18 October 2023*. Tech. rep. Official Journal of the European Union, 2023. URL: http://data.europa.eu/eli/dir/2023/2413/oj.

[2] European Commission. *The European Green Deal*. (last accessed: 28/11/2024). 2019. URL: https://commission.europa.eu/strategy-and-policy/priorities-2019-2024/european-green-deal_en.

[3] European Commission. *REPowerEU: Affordable, secure and sustainable energy for Europe*. (last accessed: 27/01/2025). 2022. URL: https://commission.europa.eu/strategy-and-policy/priorities-2019-2024/european-green-deal/repowereu-affordable-secure-and-sustainable-energy-europe_en#documents.

[4] ETIP Wind. *Getting fit for 55 and set for 2050: Electrifying Europe with wind energy*. Tech. rep. Wind Europe, 2021.

[5] Wind Europe. *Wind energy in Europe: 2023 Statistics and the outlook for 2024-2030*. Tech. rep. Wind Europe, 2023.

[6] BVG associates. *Our energy, our future: How offshore wind will help Europe go carbon-neutral*. Tech. rep. Wind Europe, 2019.

[7] INTERNATIONAL ENERGY AGENCY. *Net Zero by 2050: A Roadmap for the Global Energy Sector*. Tech. rep. INTERNATIONAL ENERGY AGENCY, 2021.

[8] T. Stehly, P. Duffy, and D. M. Hernando. *Cost of Wind Energy Review: 2024 Edition*. Tech. rep. NREL, 2024.

[9] H. Canet, P. Bortolotti, and C. L. Bottasso. "On the scaling of wind turbine rotors". In: *Wind Energy Science* 6 (3 May 2021), pp. 601–626. ISSN: 2366-7451. DOI: 10.5194/wes-6-601-2021.

[10] M. Mehta, M. Zaaijer, and D. von Terzi. "Drivers for optimum sizing of wind turbines for offshore wind farms". In: *Wind Energy Science* 9 (1 Jan. 2024), pp. 141–163. ISSN: 2366-7451. DOI: 10.5194/wes-9-141-2024.

[11] P. Bechtle, M. Schelbergen, R. Schmehl, U. Zillmann, and S. Watson. "Airborne wind energy resource analysis". In: *Renewable Energy* 141 (Oct. 2019), pp. 1103–1116. ISSN: 18790682. DOI: 10.1016/j.renene.2019.03.118.

[12] L. V. Hagen, K. Petrick, S. Wilhelm, and R. Schmehl. "Life-Cycle Assessment of a Multi-Megawatt Airborne Wind Energy System". In: *Energies* 16 (4 Feb. 2023), p. 1750. ISSN: 1996-1073. DOI: 10.3390/en16041750.

[13] K. Coutinho. “Life cycle assessment of a soft-wing airborne wind energy system and its application within an off-grid hybrid power plant configuration”. MA thesis. Delft University of Technology, 2014. URL: http://resolver.tudelft.nl/uuid:55533d19-21e1-4851-bf7c-7f3af008aaaa.

[14] C. Vermillion, M. Cobb, L. Fagiano, R. Leuthold, M. Diehl, R. S. Smith, T. A. Wood, S. Rapp, R. Schmehl, D. Olinger, and M. Demetriou. “Electricity in the air: Insights from two decades of advanced control research and experimental flight testing of airborne wind energy systems”. In: *Annual Reviews in Control* 52 (2021), pp. 330–357. ISSN: 13675788. DOI: 10.1016/j.arcontrol.2021.03.002.

[15] L. Fagiano, M. Quack, F. Bauer, L. Carnel, and E. Oland. “Autonomous Airborne Wind Energy Systems: Accomplishments and Challenges”. In: *Annual Review of Control, Robotics, and Autonomous Systems* 5 (1 May 2022), pp. 603–631. DOI: 10.1146/annurev-control-042820-124658.

[16] R. Schmehl, H. Schmidt, D. Eijkelhof, J. Poland, O. Cayon, and **R. Joshi**. “Challenges and Opportunities of Airborne Wind Energy: An Interdisciplinary Perspective”. In: *TBD* (2025). Manuscript in preparation.

[17] M. Diehl, R. Leuthold, and R. Schmehl, eds. *The International Airborne Wind Energy Conference 2017: Book of Abstracts*. Freiburg, Germany: University of Freiburg | Delft University of Technology, Oct. 5–6, 2017. 188 pp. DOI: 10.6094/UNIFR/12994.

[18] R. Paelinck and K. Rand. “Progress Along the Long and Windy Road”. In: *The 10th International Airborne Wind Energy Conference (AWEC 2024): Book of Abstracts*. Ed. by G. Sánchez-Arriaga, S. Thoms, and R. Schmehl. Accessed 09-08-2024. Madrid, Spain, Apr. 25–26, 2024, pp. 83–88. URL: http://resolver.tudelft.nl/uuid:5b930d4b-7f26-42c2-a94f-8857f9641d96.

[19] L. Fagiano, A. Croce, R. Schmehl, and S. Thoms, eds. *The International Airborne Wind Energy Conference 2021: Book of Abstracts*. Milan, Italy: Delft University of Technology, June 22–24, 2022. 188 pp. DOI: 10.4233/uuid:696eb599-ab9a-4593-aedc-738eb14a90b3.

[20] T. Mohammed, J. Busk, E. Oland, and L. Fagiano. “Large-Scale Reverse Pumping for Rigid-Wing Airborne Wind Energy Systems”. In: *Journal of Guidance, Control, and Dynamics* 47.8 (2024), pp. 1748–1758. DOI: 10.2514/1.G007859.

[21] C. Houle and R. Luchsinger. *Build wind capacities at windy locations? Assessment of system optimal wind locations*. Final Report SI/501902-01. Bern, Switzerland: Swiss Federal Office of Energy SFOE–Energy Research and Cleantech, July 2021. URL: https://www.aramis.admin.ch/Default?DocumentID=69040.

[22] Windlift Inc. *A Smarter Approach to Offshore Wind*. Accessed on 12-08-2024. 2024. URL: https://windlift.com/.

[23] T. Talton. *Navy lab funds Durham firm's airborne power generator*. Accessed on 12-08-2024. Oct. 19, 2023. URL: https://coastalreview.org/2023/10/navy-lab-funds-durham-firms-airborne-power-generator/.

[24] C. Gentry. *Harvesting Wind Through 'deep tech'*. Accessed on 12-08-2024. May 19, 2023. URL: https://www.bizjournals.com/triangle/news/2023/05/19/windlift-harvesting-wind-power-through-deep-tech.html.

[25] M. Kleineberg and F. Breipohl. "ENERWING – Innovative Airborne Wind Energy Systems". In: *LightCon 2023*. Accessed 09-08-2024. Hannover, Germany, June 13, 2023. URL: https://elib.dlr.de/196236/.

[26] Y. Zhu, X. Deng, R. Gupta, and T. Nam. "Navigation and Flight Control for Airborne Wind Energy Kite". In: *AIAA SCITECH 2024 Forum*. Orlando, FL, Jan. 8, 2024–Jan. 12, 2021, pp. 1–20. DOI: 10.2514/6.2024-2097.

[27] T. Nam, Y. Zhu, X. Deng, C. Zhao, E. Itakura, and T. Tsukada. "Development and Testing of an Airborne Wind Energy System". In: *The 10th International Airborne Wind Energy Conference (AWEC 2024): Book of Abstracts*. Ed. by G. Sánchez-Arriaga, S. Thoms, and R. Schmehl. Accessed 09-08-2024. Madrid, Spain, Apr. 25–26, 2024, p. 33. URL: http://resolver.tudelft.nl/uuid:5a67332a-9840-4a31-8ec7-4cf1701dc1db.

[28] E. Itakura. "Saving the Japan of the Future! Planning and Development of the Mothership Aerial Platform Project". In: *Toyota Technical Review*. Ed. by S. Kato. Vol. 69-2. Accessed on 12-08-2024. Aichi, Japan: Toyota Motor Corporation, July 20, 2024, pp. 69–79. URL: https://global.toyota/pages/global_toyota/mobility/technology/toyota-technical-review/TTR_Vol69-2_E.pdf.

[29] Kitekraft GmbH. *Building Flying Wind Turbines*. Accessed on 12-08-2024. 2024. URL: https://www.kitekraft.de/.

[30] "System Overview." In: *The Energy Kite Part II*. Ed. by P. Echeverri, T. Fricke, G. Homsy, and N. Tucker. 2020, pp. 93–224. URL: https://x.company/projects/makani/#.

[31] B. Luo, L. Zhang, K. Peng, Z. Ren, X. Li, Y. Sun, Y. Cai, and J. Tu. "A Parachute-Based Airborne Wind Energy System and Aerodynamic Characteristics". In: *The 10th International Airborne Wind Energy Conference (AWEC 2024): Book of Abstracts*. Ed. by G. Sánchez-Arriaga, S. Thoms, and R. Schmehl. Accessed 09-08-2024. Madrid, Spain, Apr. 25–26, 2024, pp. 35–37. DOI: http://resolver.tudelft.nl/uuid:f62bca42-2fc8-48c0-b95f-1a6f8e63cdc4.

[32] Y. Cai and X. Li. "High-altitude wind field observation of airborne wind energy system". In: *Southern Energy Construction* 11.1 (2024), pp. 1–9. DOI: 10.16516/j.ceec.2024.1.01.

[33] Skysails Power GmbH. *SKS PN-14 onshore wind power system*. Accessed 09-08-2024. 2024. URL: https://skysails-power.com/onshore-unit-pn-14/.

[34] Kitepower B.V. *Onshore Containerised AWES-100: Kitepower Falcon*. Accessed 09-08-2024. 2024. URL: https://thekitepower.com/the-falcon/.

[35] G. M. Maneia and S. Sanmartino. "A Multidimensional Trade-off". In: *The 9th International Airborne Wind Energy Conference (AWEC 2021): Book of Abstracts*. Ed. by L. Fagiano, A. Croce, R. Schmehl, and S. Thoms. Accessed 09-08-2024. Milan, Italy, June 22–24, 2022, pp. 178–183. URL: http://resolver.tudelft.nl/uuid:2e2232a9-a909-4a86-8209-75f1094a00e6.

[36] Windswept & Interesting Ltd. *Kite Turbines*. Accessed on 31-01-2022. 2024. URL: https://windswept-and-interesting.co.uk/.

[37] Wind Fisher. *WindPower: Reinvented*. Accessed on 10-08-2024. 2024. URL: https://wind-fisher.com/.

[38] C. Beaupoil. "Pumping Mode Rotary Airborne Wind Energy Systems: Exploration and Experimentation". In: *The 10th International Airborne Wind Energy Conference (AWEC 2024): Book of Abstracts*. Ed. by G. Sánchez-Arriaga, S. Thoms, and R. Schmehl. Accessed 09-08-2024. Madrid, Spain: Delft University of Technology, Apr. 25–26, 2024, p. 134. URL: http://resolver.tudelft.nl/uuid:ea05ac85-9f0d-47db-bb59-2257a317a758.

[39] someAWE Labs sl. *someAWE*. Accessed on 12-08-2024. 2024. URL: https://someawe.org/.

[40] **R. Joshi**, R. Schmehl, and M. Kruijff. "Power curve modelling and scaling of fixed-wing ground-generation airborne wind energy systems". In: *Wind Energy Science* 9.11 (2024), pp. 2195–2215. DOI: 10.5194/wes-9-2195-2024. URL: https://wes.copernicus.org/articles/9/2195/2024/.

[41] Mozaero. *Homepage*. https://www.mozaero.com/. (Accessed on 07/08/2024). 2024.

[42] **R. Joshi** and D. von Terziand R. Schmehl. "System design and scaling trends in airborne wind energy demonstrated for a ground-generation concept". In: *Wind Energy Science* 10 (2025), pp. 695–718. DOI: 10.5194/wes-10-695-2025. URL: https://doi.org/10.5194/wes-10-695-2025.

[43] G. Sánchez-Arriaga, S. Thoms, and R. Schmehl, eds. *The International Airborne Wind Energy Conference 2024: Book of Abstracts*. Madrid, Spain: Delft University of Technology, Apr. 25–26, 2024. 200 pp. DOI: 10.4233/uuid:85fd0eb1-83ec-4e34-9ac8-be6b32082a52.

[44] US Department of Energy (DOE). *Challenges and Opportunities for Airborne Wind Energy in the United States*. Report to Congress. Washington, DC, 2021. URL: https://www.energy.gov/sites/default/files/2021-12/report-to-congress-challenges-opportunities-airborne-wind-energy-united-states.pdf.

[45] J. Weber, M. Marquis, A. Cooperman, C. Draxl, R. Hammond, J. Jonkman, A. Lemke, A. Lopez, R. Mudafort, M. Optis, O. Roberts, and M. Shields. *Airborne Wind Energy*. Tech. rep. NREL/TP-5000-79992. Golden, CO: National Renewable Energy Laboratory, 2021. URL: https://www.nrel.gov/docs/fy21osti/79992.pdf.

[46] M. Sommerfeld, M. Dörenkämper, J. D. Schutter, and C. Crawford. "Scaling effects of fixed-wing ground-generation airborne wind energy systems". In: *Wind Energy Science* 7 (5 Sept. 2022), pp. 1847–1868. ISSN: 2366-7451. DOI: 10.5194/wes-7-1847-2022.

[47] F. Trevisi and A. Croce. "Given a wingspan, which windplane design maximizes power?" In: *Journal of Physics: Conference Series* 2767 (7 June 2024), p. 072014. ISSN: 1742-6588. DOI: 10.1088/1742-6596/2767/7/072014.

[48] C. Grete. "Optimization, Scaling and Economics of Pumping Kite Power Systems". MA thesis. Delft University of Technology, 2014. URL: http://resolver.tudelft.nl/uuid:b980aab7-f346-4030-97a3-a3cde13a51d6.

[49] P. Faggiani and R. Schmehl. "Design and Economics of a Pumping Kite Wind Park". In: *Airborne Wind Energy – Advances in Technology Development and Research*. Ed. by R. Schmehl. Green Energy and Technology. Singapore: Springer, 2018. Chap. 16, pp. 391–411. DOI: 10.1007/978-981-10-1947-0_16.

[50] R. Schmehl, M. Noom, and R. Van der Vlugt. "Traction Power Generation with Tethered Wings". In: *Airborne Wind Energy*. Ed. by U. Ahrens, M. Diehl, and R. Schmehl. Green Energy and Technology. Berlin Heidelberg: Springer, 2013. Chap. 2, pp. 23–45. DOI: 10.1007/978-3-642-39965-7_2.

[51] R. Van der Vlugt, A. Bley, M. Noom, and R. Schmehl. "Quasi-steady model of a pumping kite power system". In: *Renewable Energy* 131 (Feb. 2019), pp. 83–99. ISSN: 09601481. DOI: 10.1016/j.renene.2018.07.023.

[52] J. Heilmann and C. Houle. "Economics of Pumping Kite Generators". In: *Airborne Wind Energy*. Ed. by U. Ahrens, M. Diehl, and R. Schmehl. Green Energy and Technology. Berlin Heidelberg: Springer, 2013. Chap. 15, pp. 271–284. DOI: 10.1007/978-3-642-39965-7_15.

[53] A. Gambier, I. Koprek, G. Wolken-Mohlmann, and K. Vincent Redeker. *Projekt OnKites : Untersuchung zu den Potentialen von Flugwindenergieanlagen (FWEA)*. Final Project Report. Bremerhaven, Germany: Fraunhofer Institute for Wind Energy and Energy System Technology IWES, 2014. 155 pp. DOI: 10.2314/GBV:81573428X.

[54] European Commission. *Study on Challenges in the commercialisation of airborne wind energy systems*. Tech. rep. European Commission, 2018. DOI: 10.2777/87591.

[55] A. Gambier, I. Bastigkeit, and E. Nippold. *Projekt OnKites II : Untersuchung zu den Potentialen von Flugwindenergieanlagen (FWEA) Phase II*. Final Project Report. Bremerhaven, Germany: Fraunhofer Institute for Wind Energy and Energy System Technology IWES, June 2017. 105 pp. DOI: 10.2314/GBV:1009915452.

[56] M. Garcia-Sanz. “A Metric Space with LCOE Isolines for Research Guidance in wind and hydrokinetic energy systems”. In: *Wind Energy* 23 (2 Feb. 2020), pp. 291–311. DOI: 10.1002/we.2429.

[57] BVG Associates. *Getting airborne – the need to realise the benefits of airborne wind energy for net zero*. Tech. rep. BVG Associates on behalf of Airborne Wind Europe, Sept. 2022. URL: https://airbornewindeurope.org/wp-content/uploads/2023/03/BVGA-Getting-Airborne-White-Paper-220929.pdf.

[58] G. Licitra, J. Koenemann, A. Bürger, P. Williams, R. Ruiterkamp, and M. Diehl. “Performance assessment of a rigid wing Airborne Wind Energy pumping system”. In: *Energy* 173 (Apr. 2019), pp. 569–585. ISSN: 03605442. DOI: 10.1016/j.energy.2019.02.064.

[59] E. Malz, J. Koenemann, S. Sieberling, and S. Gros. “A reference model for airborne wind energy systems for optimization and control”. In: *Renewable Energy* 140 (Sept. 2019), pp. 1004–1011. ISSN: 09601481. DOI: 10.1016/j.renene.2019.03.111.

[60] D. Eijkelhof and R. Schmehl. “Six-degrees-of-freedom simulation model for future multi-megawatt airborne wind energy systems”. In: *Renewable Energy* 196 (Aug. 2022), pp. 137–150. ISSN: 09601481. DOI: 10.1016/j.renene.2022.06.094.

[61] J. D. Schutter, R. Leuthold, T. Bronnenmeyer, E. Malz, S. Gros, and M. Diehl. “AWEbox: An Optimal Control Framework for Single- and Multi-Aircraft Airborne Wind Energy Systems”. In: *Energies* 16 (4 Feb. 2023), p. 1900. ISSN: 1996-1073. DOI: 10.3390/en16041900.

[62] **R. Joshi**, M. Kruijff, and R. Schmehl. “Value-Driven System Design of Utility-Scale Airborne Wind Energy”. In: *Energies* 16 (4 Feb. 2023), p. 2075. ISSN: 1996-1073. DOI: 10.3390/en16042075.

[63] M. L. Loyd. “Crosswind kite power”. In: *Journal of Energy* 4.3 (1980), pp. 106–111. DOI: 10.2514/3.48021.

[64] I. Argatov, P. Rautakorpi, and R. Silvennoinen. “Estimation of the mechanical energy output of the kite wind generator”. In: *Renewable Energy* 34.6 (2009), pp. 1525–1532. DOI: 10.1016/j.renene.2008.11.001.

[65] R. H. Luchsinger. “Pumping Cycle Kite Power”. In: *Airborne Wind Energy*. Ed. by U. Ahrens, M. Diehl, and R. Schmehl. Green Energy and Technology. Berlin Heidelberg: Springer, 2013. Chap. 3, pp. 47–64. DOI: 10.1007/978-3-642-39965-7_3.

[66] U. Fechner and R. Schmehl. “Model-Based Efficiency Analysis of Wind Power Conversion by a Pumping Kite Power System”. In: *Airborne Wind Energy*. Ed. by U. Ahrens, M. Diehl, and R. Schmehl. Green Energy and Technology. Berlin Heidelberg: Springer, 2013. Chap. 14, pp. 249–269. DOI: 10.1007/978-3-642-39965-7_14.

[67] M. Ranneberg, D. Wölfle, A. Bormann, P. Rohde, F. Breipohl, and I. Bastigkeit. "Fast Power Curve and Yield Estimation of Pumping Airborne Wind Energy Systems". In: *Airborne Wind Energy – Advances in Technology Development and Research*. Ed. by R. Schmehl. Green Energy and Technology. Singapore: Springer, 2018. Chap. 25, pp. 623–641. DOI: 10.1007/978-981-10-1947-0_25.

[68] F. Trevisi, M. Gaunaa, and M. McWilliam. "Unified engineering models for the performance and cost of ground-gen and fly-gen crosswind airborne wind energy systems". In: *Renewable Energy* 162 (2020), pp. 893–907. DOI: 10.1016/j.renene.2020.07.129.

[69] F. Trevisi, C. E. D. Riboldi, and A. Croce. "Refining the airborne wind energy system power equations with a vortex wake model". In: *Wind Energy Science* 8 (11 Nov. 2023), pp. 1639–1650. ISSN: 2366-7451. DOI: 10.5194/wes-8-1639-2023.

[70] M. Schelbergen and R. Schmehl. "Validation of the quasi-steady performance model for pumping airborne wind energy systems". In: *Journal of Physics: Conference Series* 1618 (3 Sept. 2020), p. 032003. ISSN: 1742-6588. DOI: 10.1088/1742-6596/1618/3/032003.

[71] R. Bosman, V. Reid, M. Vlasblom, and P. Smeets. "Airborne Wind Energy Tethers with High-Modulus Polyethylene Fibers". In: *Airborne Wind Energy*. Ed. by U. Ahrens, M. Diehl, and R. Schmehl. Green Energy and Technology. Berlin Heidelberg: Springer, 2013. Chap. 33, pp. 563–585. DOI: 10.1007/978-3-642-39965-7_33.

[72] K. Vimalakanthan, M. Caboni, J. Schepers, E. Pechenik, and P. Williams. "Aerodynamic analysis of ampyx's airborne wind energy system". In: *Journal of Physics: Conference Series* 1037.062008 (2018). DOI: 10.1088/1742-6596/1037/6/062008.

[73] B. Houska and M. Diehl. "Optimal Control of Towing Kites". In: *Proceedings of the 45th IEEE Conference on Decision and Control*. IEEE, 2006, pp. 2693–2697. ISBN: 1-4244-0171-2. DOI: 10.1109/CDC.2006.377210.

[74] J. D. Anderson. *Fundamentals of Aerodynamics*. 6th ed. ISBN10: 1259129918. McGraw-Hill, 2016.

[75] M. Kruijff and R. Ruiterkamp. "A Roadmap Towards Airborne Wind Energy in the Utility Sector". In: *Airborne Wind Energy – Advances in Technology Development and Research*. Ed. by R. Schmehl. Green Energy and Technology. Singapore: Springer, 2018. Chap. 26, pp. 643–662. DOI: 10.1007/978-981-10-1947-0_26.

[76] V. Bonnin. "An Analytical Performance Model for AP-4 Conceptual Design Phase". In: *The 8th International Airborne Wind Energy Conference (AWEC 2019): Book of Abstracts*. Ed. by R. Schmehl and O. Tulloch. Glasgow, United Kingdom: University of Strathclyde | Delft University of Technology, Oct. 15–16, 2019. URL: https://repository.tudelft.nl/record/uuid:e0a4471b-c11b-4c47-b409-45d62974ce94.

[77] J. Roskam. *Airplane Design: Part V, Component Weight Estimation*. ISBN: 978-1-884885-50-1. Roskam Aviation and Engineering Corporation, 1989.

[78] R. Ruiterkamp and S. Sieberling. "Description and Preliminary Test Results of a Six Degrees of Freedom Rigid Wing Pumping System". In: *Airborne Wind Energy*. Ed. by U. Ahrens, M. Diehl, and R. Schmehl. Green Energy and Technology. Berlin Heidelberg: Springer, 2013. Chap. 26, pp. 443–458. DOI: 10.1007/978-3-642-39965-7_26.

[79] P. Echeverri, T. Fricke, G. Homsy, and N. Tucker. *The Energy Kite: Selected Results From the Design, Development and Testing of Makani's Airborne Wind Turbines*. Technical report. https://storage.googleapis.com/x-prod.appspot.com/files/Makani_TheEnergyKiteReport_Part1.pdf, (Accessed on 19/01/2024). Makani, 2020.

[80] T. Haas, J. D. Schutter, M. Diehl, and J. Meyers. "Wake characteristics of pumping mode airborne wind energy systems". In: *Journal of Physics: Conference Series* 1256 (1 July 2019), p. 012016. ISSN: 1742-6588. DOI: 10.1088/1742-6596/1256/1/012016.

[81] C. Hardham. *Response to the Federal Aviation Authority. Docket No.: FAA-2011-1279; Notice No. 11-07; Notification for Airborne Wind Energy Systems (AWES)*. Tech. rep. Makani Power, Feb. 7, 2012. URL: https://www.regulations.gov/comment/FAA-2011-1279-0014.

[82] D. Eijkelhof and R. Schmehl. "Performance vs. Mass of Box Wing Designs Using Parametrised Finite Element Modelling". In: *The 10th International Airborne Wind Energy Conference (AWEC 2024): Book of Abstracts*. Ed. by G. Sánchez-Arriaga, S. Thoms, and R. Schmehl. Madrid, Spain: Delft University of Technology, Apr. 25–26, 2024. URL: https://repository.tudelft.nl/record/uuid:1738907f-d750-4854-bbcc-535dbd11ba63.

[83] P. Williams, S. Sieberling, and R. Ruiterkamp. "Flight Test Verification of a Rigid Wing Airborne Wind Energy System". In: *2019 American Control Conference (ACC)*. 2019, pp. 2183–2190. DOI: 10.23919/ACC.2019.8814338.

[84] J. Oehler and R. Schmehl. "Aerodynamic characterization of a soft kite by in situ flow measurement". In: *Wind Energy Science* 4 (1 Jan. 2019), pp. 1–21. ISSN: 2366-7451. DOI: 10.5194/wes-4-1-2019.

[85] M. Schelbergen, P. C. Kalverla, R. Schmehl, and S. J. Watson. "Clustering wind profile shapes to estimate airborne wind energy production". In: *Wind Energy Science* 5 (3 Aug. 2020), pp. 1097–1120. ISSN: 23667451. DOI: 10.5194/wes-5-1097-2020.

[86] E. W. Peterson and J. P. J. Hennessey. "On the use of power laws for estimates of wind power potential". In: *Journal of Applied Meteorology and Climatology Search* (1978). DOI: https://doi.org/10.1175/1520-0450(1978)017<0390:OTUOPL>2.0.CO;2.

[87] **R. Joshi**, D. von Terzi, M. Kruijff, and R. Schmehl. "Techno-economic analysis of power smoothing solutions for pumping airborne wind energy systems". In: *Journal of Physics: Conference Series* 2265 (4 May 2022), p. 042069. ISSN: 1742-6588. DOI: 10.1088/1742-6596/2265/4/042069.

[88] N. Rossi. "Performance comparison and flight controller of circular and figure-of-eight paths for fixed-wing airborne wind energy systems". MA thesis. University of Trento, 2023. URL: https://doi.org/10.5281/zenodo.10160420.

[89] **R. Joshi**. *AWE-Power: A fast cycle-power computation model for fixed-wing ground-generation airborne wind energy systems*. Zenodo repository. 2024. DOI: https://doi.org/10.5281/zenodo.13842297.

[90] R. Paelink and K. Rand. "Progress Along the Long and Windy Road". In: *The 10th International Airborne Wind Energy Conference (AWEC 2024): Book of Abstracts*. Ed. by G. Sánchez-Arriaga, S. Thoms, and R. Schmehl. Madrid, Spain: Delft University of Technology, Apr. 25–26, 2024. URL: http://resolver.tudelft.nl/uuid:5b930d4b-7f26-42c2-a94f-8857f9641d96.

[91] **R. Joshi** and F. Trevisi. *Reference economic model for airborne wind energy systems*. Technical report. IEA Wind TCP Task 48, 2024. DOI: 10.5281/zenodo.10959930.

[92] V. Van Deursen. "Dynamic simulation techniques for airborne wind energy systems - Evaluating the role of kite inertia in a soft-wing system operated in pumping cycles". MA thesis. Delft University of Technology, 2024. URL: https://resolver.tudelft.nl/uuid:bb32fc5b-300a-4789-9b48-90927f035378.

[93] T. Bartsch, P. Knipper, S. Grazianski, R. Noga, and X. Paulig. "SkySails PN-14 Power Curve Measurement". In: *The 10th International Airborne Wind Energy Conference (AWEC 2024): Book of Abstracts*. Ed. by G. Sánchez-Arriaga, S. Thoms, and R. Schmehl. Accessed 09-08-2024. Madrid, Spain, Apr. 25–26, 2024, pp. 63–65. DOI: 10.4233/uuid:85fd0eb1-83ec-4e34-9ac8-be6b32082a52.

[94] European network of transmission system operators. *European network of transmission system operators*. https://www.entsoe.eu/. (accessed on 01/11/2024).

[95] Dutch Overheid. *Netherlands electricity grid code*. https://wetten.overheid.nl/BWBR0037940/2021-07-03. (accessed on 01/11/2024).

[96] T. K. Vrana, A. Attya, and L. Trilla. "Future-oriented generic grid code regarding wind power plants in Europe". In: *International Journal of Electrical Power & Energy Systems* 125 (Feb. 2021), p. 106490. ISSN: 01420615. DOI: 10.1016/j.ijepes.2020.106490.

[97] European Union. *European commission regulation*. https://eur-lex.europa.eu/legal-content/EN/TXT/?uri=CELEX%3A32016R0631. (accessed on 01/11/2024).

[98] F. Bourgault, D. Todd, J. Beatch, M. Kheiri, L. Damron, and V. S. Nasrabad. "Efficient and Power Smoothing Drive-Train Concept for Pumping Kite Generators using Hydraulics". In: *The International Airborne Wind Energy Conference 2017: Book of Abstracts*. Ed. by M. Diehl, R. Leuthold, and R. Schmehl. Freiburg, Germany: University of Freiburg | Delft University of Technology, Oct. 5–6, 2017, p. 81. DOI: 10.6094/UNIFR/12994.

[99] Mazaro. *Mazaro Transmissions for energy, emission and cost savings*. https://www.mazaro.eu/en/pioneering-transmission-technology. (accessed on 01/11/2024).

[100] C. Rueb and M. Tueteberg. *Personal communication–technical support*. DC-IH/STS1 Bosch Rexroth, 2021.

[101] NOV. *National oilwell varco Powerblade kinetic energy recovery system*. https://www.nov.com/-/media/nov/files/products/rig/rig-equipment/power-systems/powerblade-kinetic-energy-recovery-system-spec-sheet.pdf. (accessed on 25/11/2021).

[102] Beacon Power. *Beacon power Flywheel energy storage systems*. https://beaconpower.com/. (accessed on 01/11/2024).

[103] BVG Associates. *Wind farm costs – Guide to an offshore wind farm*. (Accessed on 03/20/2023). Jan. 2019. URL: https://guidetoanoffshorewindfarm.com/wind-farm-costs.

[104] S. Sabihuddin, A. Kiprakis, and M. Mueller. "A Numerical and Graphical Review of Energy Storage Technologies". In: *Energies* 8 (1 Dec. 2014), pp. 172–216. ISSN: 1996-1073. DOI: 10.3390/en8010172.

[105] H. Zhao, Q. Wu, S. Hu, H. Xu, and C. N. Rasmussen. "Review of energy storage system for wind power integration support". In: *Applied Energy* 137 (Jan. 2015), pp. 545–553. ISSN: 03062619. DOI: 10.1016/j.apenergy.2014.04.103.

[106] K. Mongird, V. Fotedar, V. Viswanathan, V. Koritarov, P. Balducci, B. Hadjerioua, and J. Alam. *Energy storage technology and cost characterization report*. 2019.

[107] J. Leon-Quiroga, B. Newell, M. Krishnamurthy, A. Gonzalez-Mancera, and J. Garcia-Bravo. "Energy Efficiency Comparison of Hydraulic Accumulators and Ultracapacitors". In: *Energies* 13 (7 Apr. 2020), p. 1632. ISSN: 1996-1073. DOI: 10.3390/en13071632.

[108] R. Georgious, R. Refaat, J. Garcia, and A. A. Daoud. "Review on Energy Storage Systems in Microgrids". In: *Electronics* 10 (17 Sept. 2021), p. 2134. ISSN: 2079-9292. DOI: 10.3390/electronics10172134.

[109] **R. Joshi** and F. Trevisi. *AWE-Eco: A reference economic model for airborne wind energy systems*. Zenodo repository. 2024. DOI: https://doi.org/10.5281/zenodo.12166697.

[110] IEA Wind TCP. *IEA Wind Task 48 on Airborne Wind Energy*. (accessed on October 24, 2024). 2021. URL: https://iea-wind.org/task48/.

[111] M. De Lellis, A. K. Mendonça, R. Saraiva, A. Trofino, and Lezana. "Electric power generation in wind farms with pumping kites: An economical analysis". In: *Renewable Energy* 86 (2016), pp. 163–172. DOI: 10.1016/j.renene.2015.08.002.

[112] P. Faggiani and R. Schmehl. "Design and Economics of a Pumping Kite Wind Park". In: *Airborne Wind Energy. Green Energy and Technology. Springer, Singapore*. Ed. by R. Schmehl. 2018, pp. 391–411. DOI: 10.1007/978-981-10-1947-0_16.

[113] F. Bauer, R. M. Kennel, C. M. Hackl, F. Campagnolo, M. Patt, and R. Schmehl. "Drag power kite with very high lift coefficient". In: *Renewable Energy* 118 (2018), pp. 290–305. ISSN: 18790682. DOI: 10.1016/j.renene.2017.10.073.

[114] BVG Associates. *Wind farm costs – Guide to an offshore wind farm*. (Accessed on 03/20/2023). Jan. 2019. URL: https://guidetoanoffshorewindfarm.com/wind-farm-costs.

[115] NREL. *Theory — WISDEM 2.0 documentation on cost scaling*. (Accessed on 03/20/2023). URL: https://wisdem.readthedocs.io/en/master/wisdem/nrelcsm/theory.html.

[116] M. Garcia-Sanz. "A Metric Space with LCOE Isolines for Research Guidance in wind and hydrokinetic energy systems". In: *Wind Energy* 23.2 (2020), pp. 291–311. DOI: https://doi.org/10.1002/we.2429. eprint: https://onlinelibrary.wiley.com/doi/pdf/10.1002/we.2429. URL: https://onlinelibrary.wiley.com/doi/abs/10.1002/we.2429.

[117] N. Tucker. "Airborne Wind Turbine Performance: Key Lessons From More Than a Decade of Flying Kites." In: *The Energy Kite Part I*. Ed. by P. Echeverri, T. Fricke, G. Homsy, and N. Tucker. 2020, pp. 93–224. URL: https://x.company/projects/makani/#.

[118] F. Trevisi, M. Gaunaa, and M. McWilliam. "Unified engineering models for the performance and cost of Ground-Gen and Fly-Gen crosswind Airborne Wind Energy Systems". In: *Renewable Energy* 162 (2020), pp. 893–907. DOI: 10.1016/j.renene.2020.07.129.

[119] T. Stehly, P. Beiter, and P. Duffy. *2019 Cost of Wind Energy Review*. Tech. rep. NREL/TP-5000-78471. National Renewable Energy Laboratory, 2020. URL: https://www.nrel.gov/docs/fy21osti/78471.pdf.

[120] V. Ramasamy, J. Zuboy, E. O'Shaughnessy, D. Feldman, J. Desai, M. Woodhouse, P. Basore, and R. Margolis1. *U.S. Solar Photovoltaic System and Energy Storage Cost Benchmarks, With Minimum Sustainable Price Analysis: Q1 2022*. Tech. rep. National Renewable Energy Laboratory, 2022. URL: https://www.nrel.gov/docs/fy22osti/83586.pdf.

[121] Kitepower B.V. *The Hawk - Kitepower*. https://thekitepower.com/the-hawk/. (Accessed on 04/11/2024).

[122] F. Bourgault, D. Todd, J. Beatch, M. Kheiri, L. Damron, and V. S. Nasrabad. "Efficient and Power Smoothing Drive-Train Concept for Pumping Kite Generators using Hydraulics". In: *7th international Airborne Wind Energy Conference (AWEC 2017): Book of Abstracts*. https://repository.tudelft.nl/islandora/object/uuid:fba9c248-da91-4252-b89a-d5b6bef124b2/datastream/OBJ/download. Freiburg, Germany, Oct. 5, 2017–Oct. 6, 2022.

[123] Diinef. *Ground stations for Airborne Wind Energy*. https://www.diinef.com/kopi-av-airborne-wind. (Accessed on 04/04/2024).

[124] International Renewable Energy Agency (IRENA). *Renewable Power Generation Costs in 2019*. URL: https://www.irena.org/publications/2020/Jun/Renewable-Power-Costs-in-2019.

[125] International Renewable Energy Agency (IRENA). *Renewable Power Remains Cost-Competitive amid Fossil Fuel Crisis*. URL: https://www.irena.org/News/pressreleases/2022/Jul/Renewable-Power-Remains-Cost-Competitive-amid-Fossil-Fuel-Crisis.

[126] F. Tanrisever, K. Derinkuyu, and G. Jongen. "Organization and functioning of liberalized electricity markets: An overview of the Dutch market". In: *Renewable and Sustainable Energy Reviews* 51 (Nov. 2015), pp. 1363–1374. DOI: 10.1016/j.rser.2015.07.019.

[127] KU Leuven Energy Institute. *The current electricity market design in Europe*. EI Fact Sheet. https://set.kuleuven.be/ei/images/EI_factsheet8_eng.pdf. 2015.

[128] G. Erbach. *Understanding electricity markets in the EU*. Briefing. https://www.europarl.europa.eu/RegData/etudes/BRIE/2016/593519/EPRS_BRI(2016)593519_EN.pdf. European Parliamentary Research Service, Nov. 2016.

[129] C. K. Woo, I. Horowitz, J. Moore, and A. Pacheco. "The impact of wind generation on the electricity spot-market price level and variance: The Texas experience". In: *Energy Policy* 39.7 (2011), pp. 3939–3944. DOI: 10.1016/j.enpol.2011.03.084.

[130] L. Hirth. "The market value of variable renewables. The effect of solar wind power variability on their relative price". In: *Energy Economics* 38 (July 2013), pp. 218–236. DOI: 10.1016/j.eneco.2013.02.004.

[131] L. Hirth and S. Müller. "System-friendly wind power. How advanced wind turbine design can increase the economic value of electricity generated through wind power". In: *Energy Economics* 56 (2016), pp. 51–63. ISSN: 01409883. DOI: 10.1016/j.eneco.2016.02.016.

[132] P. Swisher, J. P. M. Leon, J. Gea-Bermúdez, M. Koivisto, H. A. Madsen, and M. Münster. "Competitiveness of a low specific power, low cut-out wind speed wind turbine in North and Central Europe towards 2050". In: *Applied Energy* 306 (Jan. 2022), p. 118043. DOI: 10.1016/j.apenergy.2021.118043.

[133] J. Simpson, E. Loth, and K. Dykes. “Cost of Valued Energy for design of renewable energy systems”. In: *Renewable Energy* 153 (June 2020), pp. 290–300. DOI: 10.1016/j.renene.2020.01.131.

[134] H. Canet, A. Guilloré, and C. L. Bottasso. “The eco-conscious wind turbine: design beyond purely economic metrics”. In: *Wind Energy Science* 8.6 (2023), pp. 1029–1047. DOI: 10.5194/wes-8-1029-2023.

[135] A. de Souza Range, J. C. de Souza Santos, and J. R. F. Savoia. “Modified Profitability Index and Internal Rate of Return”. In: *Journal of International Business and Economics* 4 (2 2016). ISSN: 23742208. DOI: 10.15640/jibe.v4n2a2.

[136] J. Simpson, E. Loth, and K. Dykes. “Cost of Valued Energy for design of renewable energy systems”. In: *Renewable Energy* 153 (June 2020), pp. 290–300. ISSN: 18790682. DOI: 10.1016/j.renene.2020.01.131.

[137] M. Mehta, M. Zaaijer, and D. von Terzi. “Designing wind turbines for profitability in the day-ahead markets”. In: *Wind Energy Science Discussions* (2024). [preprint]. URL: https://doi.org/10.5194/wes-2024-43.

[138] European Commission. *Renewable energy policy database*. URL: http://www.res-legal.eu/home/.

[139] I. Komusanac, D. Fraile, and G. Brindley. *Wind energy in Europe in 2018 - Trends and statistics*. Tech. rep. https://windeurope.org/wp-content/uploads/files/about-wind/statistics/WindEurope-Annual-Statistics-2018.pdf. Wind Europe, Feb. 2019.

[140] ENTSO-E. *Bidding Zone Configuration Technical Report 2021*. Technical report. https://eepublicdownloads.azureedge.net/clean-documents/mc-documents/entso-e_bzr_technical_report_2021_211109_med.pdf. 2021.

[141] European Centre for Medium-Range Weather Forecasts (ECMWF). *ERA5 dataset*. URL: https://www.ecmwf.int/en/forecasts/datasets/reanalysis-datasets/era5.

[142] European Network of Transmission System Operators for Electricity (ENTSOE-E). *ENTSO-E Transparency Platform*. URL: https://transparency.entsoe.eu.

[143] L. E. Raffalovich. “Detrending Time Series”. In: *Sociological Methods & Research* 22 (4 May 1994), pp. 492–519. ISSN: 0049-1241. DOI: 10.1177/0049124194022004003.

[144] L. Wasserman. *All of Statistics - A Concise Course in Statistical Inference*. 2004. URL: https://link.springer.com/book/10.1007/978-0-387-21736-9.

[145] V. Salma and R. Schmehl. “Operation Approval for Commercial Airborne Wind Energy Systems”. In: *Energies* 16 (7 Apr. 2023), p. 3264. ISSN: 1996-1073. DOI: 10.3390/en16073264.

[146] A. B. Lambe and J. R. R. A. Martins. “Extensions to the design structure matrix for the description of multidisciplinary design, analysis, and optimization processes”. In: *Structural and Multidisciplinary Optimization* 46 (2 Aug. 2012), pp. 273–284. ISSN: 1615-147X. DOI: 10.1007/s00158-012-0763-y.

[147] **R. Joshi**. *AWE-SE: A systems engineering framework for system design of airborne wind energy*. Zenodo repository. 2025. DOI: https://doi.org/10.5281/zenodo.15187607.

[148] International Electrotechnical Commission (IEC). *Wind energy generation systems - Part 1: Design requirements (IEC 61400-1:2019,IDT)*. Tech. rep. IEC 61400-1. Geneva, Switzerland. International Electrotechnical Commission (IEC), 2019.

[149] M. Diehl. “Airborne Wind Energy: Basic Concepts and Physical Foundations”. In: *Airborne Wind Energy*. Ed. by U. Ahrens, M. Diehl, and R. Schmehl. Green Energy and Technology. Berlin Heidelberg: Springer, 2013. Chap. 1, pp. 3–22. DOI: 10.1007/978-3-642-39965-7_1.

[150] IRENA. *Renewable power generation costs in 2023*. Tech. rep. International Renewable Energy Agency, 2023. URL: https://www.irena.org/-/media/Files/IRENA/Agency/Publication/2024/Sep/IRENA_Renewable_power_generation_costs_in_2023.pdf.

[151] E. C. Malz, V. Walter, L. Göransson, and S. Gros. “The value of airborne wind energy to the electricity system”. In: *Wind Energy* 25 (2 Feb. 2022), pp. 281–299. ISSN: 1095-4244. DOI: 10.1002/we.2671.

[152] H. Vos, F. Lombardi, **R. Joshi**, R. Schmehl, and S. Pfenninger. “The potential role of airborne and floating wind in the North Sea region”. In: *Environmental Research: Energy* 1 (2 June 2024), p. 025002. ISSN: 2753-3751. DOI: 10.1088/2753-3751/ad3fbc.

[153] K. Coutinho, P. Maharjan, L. Reitz, **R. Joshi**, and R. Schmehl. “Life cycle assessment of a soft-wing airborne wind energy system”. In: *TBD* (2025). Manuscript in preparation.

[154] S. Reuchlin, **R. Joshi**, and R. Schmehl. “Sizing of Hybrid Power Systems for Off-Grid Applications Using Airborne Wind Energy”. In: *Energies* 16.10 (May 2023), p. 4036. ISSN: 1996-1073. DOI: 10.3390/en16104036. URL: https://www.mdpi.com/1996-1073/16/10/4036.

ACKNOWLEDGEMENTS

I take this opportunity to express my gratitude towards every aspect of my life that has shaped and enabled me to reach this milestone! India — the country and its culture which nurtured my core values; My school teachers — who taught me the most fundamental things; The Netherlands — which has warmly hosted me for the past six years, and a country I admire for its simplicity, openness and discipline; The ever-evolving circle of people around me — who, knowingly or unknowingly, have contributed to shaping who I am today.

Since this is a section in my PhD dissertation, I will focus on my recent four-year journey. First and foremost, I am grateful to TU Delft for fostering an excellent academic environment supported by remarkably knowledgeable and efficient staff. Roland Schmehl, thank you for giving me this opportunity and for your invaluable feedback and guidance throughout the four years. I am amazed by your passion for airborne wind energy, and I wish all people could find their own passion as you found yours. Dominic von Terzi, thank you for teaching me how to see the bigger picture and identifying the relevance of my work. Your invaluable insights and encouragement were instrumental in shaping my PhD into what it has ultimately become. Michiel Zaaijer, thank you for inspiring me to choose wind energy systems as my specialisation during my master's and continuing it in my PhD. I really admire your ability and willingness to coach and mentor your students.

Many of my peers have been instrumental in shaping my PhD. Mihir, my understanding of various concepts of wind energy and energy markets improved due to many of our discussions. Oriol, you were my sparring partner when I was stuck on the performance model, trying to understand the inertial effects. Our discussions were crucial in developing my understanding. Jelle, I have admired and learnt from many of your qualities, such as your calmness, your hunger to keep learning new things, and efficiently managing professional as well as personal time. Moreover, I have enjoyed our philosophical conversations with both of you. Dylan, we were the only fixed-wing community at Delft, and I have learnt a lot from many of our technical discussions. Filippo, I am glad you came for the secondment at Delft, and we were able to work together on the first-ever cost model for airborne wind energy systems. You significantly contributed to my understanding of flight dynamics through our discussions. Helena, thank you for introducing me to the domain of social sciences and their significance in technology development.

David, you have become one of my closest friends from my PhD time. I admire and have learnt a lot from your positive and playful nature. This cannot be our final arc. Deepali, you were one of my first friends after starting my PhD when we came back to the office after the COVID pandemic. We instantly shared the same energy and became really good friends. Erik, the board game master, I relate and

learnt from the competitive spirit you hold, which is a motivator to give our best in any activity we perform. Matteo, you were a fellow systems engineer, and I am grateful for your advice on my PhD and my next career steps. Likhita, I appreciate your thoughtfulness in making personalised, beautiful drawings on cards for us on our special occasions. Adhyanth, the anime master, thank you for motivating me to start watching One Piece and for all the spoilers along the way. Ali, I have enjoyed and learnt a lot from our discussions on geopolitics and financial markets. Ricardo, thank you for motivating me to keep training and watching my diet for a pipe dream of getting six-pack abs. Mehtab, sirjee, you were the only person with whom I could enjoy sharing Urdu/Hindi poetry. Shyam and Simone, thank you for introducing me to whatever you guys do by spotting and capturing aeroplanes. Abhyuday, ABD, thank you for being cheerful all the time. Kiran, the only person other than me who understands how amazing Bombay Corner food is. Guanqun, Jingna, Livia, Anand, George, Shantanu, Haoyan, Augustin, Clem, Cristina, Ivan and Seba – my time at the office wouldn't have been nearly as enjoyable without each of you. Thank you for making it such a memorable experience!

Along with my academic circle, it's very important that I thank my other social circles, which kept me alive as a person. Lolya, Palande, and Parikshit, I am grateful for your friendship since I could be a 'Maharashtrian' in the Netherlands. I would like to thank the Netherlands Marathi Mandal and all its members for organising and celebrating different Indian festivals, keeping the spirit of India alive within me. Agney, Nikhil, Ashish, and Tworit paaji, I am grateful for our intriguing discussions, game nights and hang-outs throughout the last 4 years. Our discussions have inspired and taught me many new things, especially our 'Shastrarth', Tworit. Aditya, thank you so much for designing such a beautiful cover page for my dissertation. Amdya, Jadya, Pandya, Kaushya, Sabnya, Tamhya — It's impossible not to mention you guys. We have seen each other grow, we have learnt innumerable things from each other, and I am sure we will continue to do the same until the end.

Lastly, I would like to express my deepest gratitude to my three pillars — Vaishnavi, Aai, and Baba. This journey would have been impossible without you on my side.

Curriculum Vitæ

Rishikesh Joshi

17-02-1996	Born in Pune, India.

Education

2002 – 2012	Primary and secondary education Sinhgad Spring Dale School, Pune, India
2012 – 2014	Higher secondary education Sinhgad College of Arts, Commerce and Science, Pune, India
2014 – 2018	B.Tech Mechanical Engineering Vellore Institute of Technology, Vellore, India
2018 – 2020	M.Sc Sustainable Energy Technology Delft University of Technology, The Netherlands
2021 – 2025	Ph.D Aerospace Engineering Delft University of Technology, The Netherlands

Experience

2025 – present	Energy Market Analyst EP Commodities B.V., The Netherlands

List of Publications

First-Author

5. **R. Joshi** and D. von Terziand R. Schmehl. "System design and scaling trends in airborne wind energy demonstrated for a ground-generation concept". In: *Wind Energy Science* 10 (2025), pp. 695–718. DOI: 10.5194/wes-10-695-2025. URL: https://doi.org/10.5194/wes-10-695-2025

4. **R. Joshi**, R. Schmehl, and M. Kruijff. "Power curve modelling and scaling of fixed-wing ground-generation airborne wind energy systems". In: *Wind Energy Science* 9.11 (2024), pp. 2195–2215. DOI: 10.5194/wes-9-2195-2024. URL: https://wes.copernicus.org/articles/9/2195/2024/

3. **R. Joshi** and F. Trevisi. *Reference economic model for airborne wind energy systems*. Technical report. IEA Wind TCP Task 48, 2024. DOI: 10.5281/zenodo.10959930

2. **R. Joshi**, M. Kruijff, and R. Schmehl. "Value-Driven System Design of Utility-Scale Airborne Wind Energy". In: *Energies* 16 (4 Feb. 2023), p. 2075. ISSN: 1996-1073. DOI: 10.3390/en16042075

1. **R. Joshi**, D. von Terzi, M. Kruijff, and R. Schmehl. "Techno-economic analysis of power smoothing solutions for pumping airborne wind energy systems". In: *Journal of Physics: Conference Series* 2265 (4 May 2022), p. 042069. ISSN: 1742-6588. DOI: 10.1088/1742-6596/2265/4/042069

Co-authored

4. R. Schmehl, H. Schmidt, D. Eijkelhof, J. Poland, O. Cayon, and **R. Joshi**. "Challenges and Opportunities of Airborne Wind Energy: An Interdisciplinary Perspective". In: *TBD* (2025). Manuscript in preparation

3. K. Coutinho, P. Maharjan, L. Reitz, **R. Joshi**, and R. Schmehl. "Life cycle assessment of a soft-wing airborne wind energy system". In: *TBD* (2025). Manuscript in preparation

2. H. Vos, F. Lombardi, **R. Joshi**, R. Schmehl, and S. Pfenninger. "The potential role of airborne and floating wind in the North Sea region". In: *Environmental Research: Energy* 1 (2 June 2024), p. 025002. ISSN: 2753-3751. DOI: 10.1088/2753-3751/ad3fbc

1. S. Reuchlin, **R. Joshi**, and R. Schmehl. "Sizing of Hybrid Power Systems for Off-Grid Applications Using Airborne Wind Energy". In: *Energies* 16.10 (May 2023), p. 4036. ISSN: 1996-1073. DOI: 10.3390/en16104036. URL: https://www.mdpi.com/1996-1073/16/10/4036

LIST OF OPEN-SOURCE SOFTWARE

3. **R. Joshi**. *AWE-SE: A systems engineering framework for system design of airborne wind energy.* Zenodo repository. 2025. DOI: https://doi.org/10.5281/zenodo.15187607

2. **R. Joshi**. *AWE-Power: A fast cycle-power computation model for fixed-wing ground-generation airborne wind energy systems.* Zenodo repository. 2024. DOI: https://doi.org/10.5281/zenodo.13842297

1. **R. Joshi** and F. Trevisi. *AWE-Eco: A reference economic model for airborne wind energy systems.* Zenodo repository. 2024. DOI: https://doi.org/10.5281/zenodo.12166697

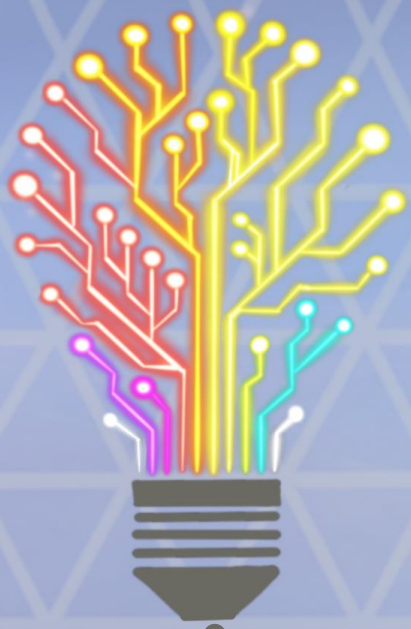

TU Delft